

ABSTRACT

Title of Dissertation: THE PHYSICS OF THE STRONGLY DRIVEN
MAGNETOSPHERE: GLOBAL MHD MODELING

Viatcheslav G. Merkine, Doctor of Philosophy, 2004

Dissertation directed by: Prof. Konstantinos (Dennis) Papadopoulos
Department of Physics

This study examines the behavior of the earth's magnetosphere under extreme solar wind conditions using global magnetohydrodynamic (MHD) simulations. Particular emphasis is placed on the phenomenon of the cross polar cap potential (CPCP) saturation. The effect refers to the tendency of the potential to level off instead of growing linearly as the interplanetary electric field (IEF) increases. The CPCP is an important indicator of the coupling in the solar wind-magnetosphere-ionosphere (SW-M-I) system since it is mapped along the equipotential magnetic field lines from the dayside reconnection line. Due to the CPCP saturation a large amount of the solar wind energy is prevented from directly accessing the ionosphere which limits the ionospheric response to the solar wind driver.

Global MHD simulations are a natural tool to study the phenomenon of the CPCP saturation. Despite the lack of proper microscopic shock and reconnection physics, such models reproduce many global phenomena in the SW-M-I system and its geometry. As discussed in this dissertation the problem of the CPCP saturation is in many respects a matter of geometry: The reconnection potential is formed in the magnetosheath flow which properties are affected greatly by the geometry of the magnetosphere.

A series of simulations with idealized solar wind and ionosphere was conducted to study the dependence of the CPCP on the IEF and ionospheric conductance in a wide range of values. The simulations confirmed the CPCP saturation, but the level of saturation was shown to be strongly dependent on the ionospheric conductance. A mechanism of the ionospheric conductance feedback on the global characteristics of the SW-M-I system leading to the CPCP saturation was proposed.

As a result of these studies a phenomenological model of the CPCP saturation was formulated. The main building blocks of this model are the direct amplifying effect of the solar wind electric field and the adverse feedback of the ionospheric conductance on the reconnection potential. Finally, test simulations were conducted with improved ionospheric model which incorporated a parametrized dependence of the ionospheric conductance on the IEF.

THE PHYSICS OF THE STRONGLY DRIVEN MAGNETOSPHERE:

GLOBAL MHD MODELING

by

Viatcheslav G. Merkine

Dissertation submitted to the Faculty of the Graduate School of the
University of Maryland, College Park in partial fulfillment
of the requirements for the degree of
Doctor of Philosophy
2004

Advisory Committee:

Prof. Konstantinos (Dennis) Papadopoulos, Chairman/Advisor
Prof. Charles C. Goodrich,
Prof. Roald Sagdeev,
Dr. A. Surjalal Sharma,
Prof. Theodore Rosenberg

© Copyright by

Viatcheslav G. Merkin

2004

DEDICATION

To my dearest wife Tanya for her devoted love, endless patience, and
understanding,

To my parents for their unconditional support and encouragement,
and

To my late grandmother who had always set a great example of human kindness
and wisdom.

ACKNOWLEDGMENTS

I would like to express my gratitude to my advisors: Dennis Papadopoulos, Surja Sharma, and Gennady Milikh. Dennis for his strong guidance and intuition, encouragement to develop as an independent scientist, and uncompromising approach to physics. Surja for his judicious counsel and support. Gennady for his invaluable commitment and perpetual willingness to help.

I am grateful to my friend and colleague Sasha Ukhorskiy for countless hours spent in debates and discussions during all these years. He has always set a great example and I have learned many things from him.

Finally, I would like to thank people whose help throughout the work on this dissertation I appreciate greatly: Xi Shao, Misha Sitnov, Charles Goodrich, John Lyon, and Michael Wiltberger.

Scientific computations were accomplished on Origin 2000 and IBM p690 supercomputer systems of the National Center for Supercomputing Applications at the University of Illinois, Urbana-Champaign.

TABLE OF CONTENTS

List of Tables	vii
List of Figures	viii
1 Introduction	1
2 Global MHD Modeling of the Earth's Magnetosphere	10
2.1 Ideal Magnetohydrodynamics and its Validity for the Magnetospheric Plasmas	11
2.2 Numerical Solution of the Ideal MHD Equations	14
2.2.1 Finite-Volume Methods	14
2.2.2 Flux-Limiter Methods	15
2.2.3 Flux-Corrected Transport	18
2.2.4 Treatment of the Magnetic Field	20
2.2.5 Treatment of Magnetic Reconnection	21
2.3 The Lyon-Fedder-Mobarry Global MHD Model	22
2.3.1 The LFM Grid and MHD Boundary Conditions	23
2.3.2 The Ionospheric Simulation	25

3	Effects of the Solar Wind Activity on the Ionospheric Conductance	30
3.1	Conductivity Tensor of Partially Ionized Plasma	30
3.2	Ionization due to Particle Precipitation	34
3.3	Turbulent Electron Heating	36
4	The Cross Polar Cap Potential: Observational Evidence and Theoretical Models of Saturation	47
4.1	Observations of the Cross Polar Cap Potential	49
4.1.1	Boyle Empirical Potentials	50
4.1.2	Weimer potentials	53
4.1.3	AMIE Polar Cap Potentials	56
4.1.4	SuperDARN Polar Cap Potentials	58
4.2	Seasonal Dependence of the Cross Polar Cap Potential	61
4.3	The Hill/Siscoe model of the cross polar cap potential saturation . .	66
4.3.1	Formulation	66
4.3.2	Comparison with observations	71
4.4	Discussion	73
5	Global MHD Simulations of the Earth's Magnetosphere Under Strong Southward IMF	86
5.1	Code Run Specifications	87
5.2	Cross Polar Cap Potential and Reconnection Potential	89

5.3	Magnetosheath Flow Stagnation and Saturation of the Reconnection Potential	93
5.4	Effect of the Ionospheric Conductance	97
5.5	Effect of the Solar Wind Dynamic Pressure	101
5.6	Discussion and Conclusions	102
6	Ionospheric Conductance Control of the Magnetopause Size and Magnetosheath Flow	111
6.1	Introduction	112
6.2	Effect of the Ionospheric Conductance on the Transpolar Potential and the Size of the Magnetopause	113
6.3	Pressure Balance and the Magnetopause Size	114
6.4	Field Aligned Current System and the Size of the Magnetopause	117
6.4.1	Figure-Eight Field Aligned Current	118
6.4.2	Field Aligned Current Inferred from the Simulations	120
6.5	The Magnetopause Size and the Flow in the Magnetosheath	123
6.6	Ram Pressure Effect Revisited	127
6.7	Conclusions	127
7	Summary and Future Work	136
7.1	Summary and Conclusions	136
7.2	Implications for Future Work	139

LIST OF TABLES

4.1	Correlation fit to (4.5). R stands for the correlation coefficient. (from [<i>Burke et al.</i> , 1999])	77
5.1	The solar wind plasma parameters used in the simulation of the Φ_{PC} dependence on the IEF	105
5.2	The solar wind plasma parameters used in the simulation of the Φ_{PC} dependence on the solar wind dynamic pressure	105

LIST OF FIGURES

1.1	Schematic illustration of trajectories of positive ions (+) and electrons (-) incident on the planetary magnetic field.	8
1.2	Schematic representation of the magnetosphere showing the solar wind flow, the general structure of the magnetosphere, and the magnetospheric current system.	8
1.3	Reconnection model of the magnetosphere with southward IMF [after <i>Dungey, 1961</i>]	9
1.4	Typical convection pattern in the polar ionosphere. The distribution of the electrostatic potential is shown along with the equipotential lines. GSM coordinate system is used. The figure is obtained from global MHD simulations.	9
2.1	Results from the numerical solution of 1-d advection equation with constant speed: exact solution (solid), upstream (dashed), Lax-Wendroff (dotted), flux-limiter combination of upstream and Lax-Wendroff methods (dash-dotted).	28

2.2	Centering of the magnetic fluxes and electric fields in a grid cell ensuring the divergence free magnetic field. The center of the cell has coordinates (i,j,k). The arrows along the edges show the direction of the path integral in the Faraday's law.	28
2.3	A 2D cut of the LFM simulation grid. The full 3D grid is recovered by rotating the depicted grid about the long axis by uniformly spaced azimuthal angles.	29
3.1	(a) Idealized representation of a three-zone auroral-particle precipitation pattern. The auroral-oval (medium-energy) precipitation is represented by the triangles, the auroral-zone (high-energy) by the dots, and the polar-cusp (low-energy) precipitation on the dayside by the stars. The average flux is indicated approximately by the density of the symbols. (b) Integrated energy flux into the auroral ionosphere across the dawn-dusk plane as a function of geomagnetic latitude for electrons and protons. (from [<i>Kivelson and Russell</i> , 1995])	43
3.2	Altitudinal profiles of the ionization rate. a) due to a flux of 10^8 electrons/cm ² s at several initial values of energy, E_p (keV), precipitating along magnetic field lines into the earth's atmosphere. b) due to proton fluxes with initial energy, E_p , identified on each curve. An isotropic flux over the upper hemisphere is assumed and the energy flux is 0.1 erg/cm ² s at every initial proton energy. (from [<i>Rees</i> , 1989])	44

3.3	Electron density profiles from [<i>Barr and Stubbe, 1984</i>]	45
3.4	Isotherms of the electron temperature. The dotted trace shows the threshold of the Farley-Buneman instability, while the dashed trace shows the ion magnetization height. Numbers from 1 to 7 correspond to $T_e = 300, 500, 1000, 1500, 2000, 2500,$ and 3000 K, respectively. (from [<i>Milikh and Dimant, 2003</i>])	45
3.5	A typical distribution of the electric field in the polar ionosphere corresponding to storm-like conditions. The plot is based on global MHD simulations.	46
4.1	Relationship between the observed potential and the predictions of equation (4.2). This fit and the plot use 127 cleanest passes with 4 hours of steady IMF which occurred near the terminator. (from [<i>Boyle et al., 1997</i>])	77
4.2	Observed cross polar cap potentials normalized by the unsaturated value predicted by the model (4.2) versus a single hour average IMF with requirement of 2 hours steady IMF. (from [<i>Boyle et al., 1997</i>])	78
4.3	Potential drop plotted versus the corresponding value of the IEF for due southward IMF from the measurements by <i>Burke et al.</i> [1999] (after [<i>Russell et al., 2001</i>])	78

4.4	One hour averages of the cross polar cap potential and the Joule heating versus the IEF with arctan fit during a) September 24-25, 1998 storm; b) May 2-4, 1998 storm; c) January 9-11, 1997 storm; d) October 18-20, 1995 storm; e) October 18-20, 1998 storm (from [Russell et al., 2001])	79
4.5	Solutions of the electrostatic potential using APL FIT for the shown 10-min periods. The small dots indicate the positions of the SuperDARN measurements. Contours are the equipotentials as determined by the APL FIT procedure spaced at 6-kV increments. (from [Shepherd et al., 2002])	80
4.6	Φ_{PC} as a function of E_{KL} as determined using APL FIT for a) all 10-min periods satisfying the quasi-stability condition and b) those periods where the SuperDARN data sufficiently determine Φ_{PC} . Each 10-min period is represented by a dot. A sliding, linear least squares fit to data within a 10 kV/R _E window, and corresponding 2- σ deviations, are shown for each unit of E_{KL} up to 40 kV/R _E . Due to the sparsity of data in the range $E_{KL} > 40$ kV/R _E , a single fit was performed on these data. (from [Shepherd et al., 2002])	81
4.7	Average cross polar cap potentials by seasons for the northern hemisphere inferred from DMSP satellite polar passes. (from [Boyle et al., 1997])	82

4.8	The dependence of the average cross polar cap potential on the IMF strength range for due southward IMF. The solid line corresponds to winter, the dotted line is for summer, and the dashed line is for equinox. The figure is based on the data from DMSP satellites during the period September 1987 to December 1990 as presented by <i>Rich and Hairston</i> [1994].	82
4.9	The transpolar potential given by the four shown models of polar convection for each season. The IMF conditions correspond to $B_T = 5$ nT and due southward magnetic field. Triangles correspond to equinox, diamond signs correspond to summer, and squares are for winter.	83
4.10	Comparison of cross polar cap potential as given by Hill/Siscoe model and data from a magnetic storm of 24, 25 September 1998 (from [<i>Siscoe et al.</i> , 2002b])	84
4.11	Comparison of saturation as given by Hill/Siscoe model and data from six DMSP F13 passes during a magnetic storm of 31 March 2001. The Φ_{PC} curves are the potentials from the Hill/Siscoe model with $\Sigma_P = 5$ and 10 mhos and $p_{sw} = 6.08$ nPa. The Φ_A line is the Boyle potentials [<i>Boyle et al.</i> , 1997]. The Φ_M line is the calculated potential as given by (4.17) (from [<i>Hairston et al.</i> , 2003])	84

4.12	a) Cross polar cap potentials observed by SuperDARN and the best fit Hill/Siscoe model ($\Sigma = 23$ mhos and the constant potential $\Phi_0 = 17$ kV) plotted against the reconnection electric field. Also the potentials from Boyle model and Siscoe/Hill model with $\Sigma = 2$ and $\Sigma = 44$ mhos are shown. b) Distribution of events in reconnection electric field. (from [<i>Shepherd et al.</i> , 2002])	85
5.1	Temporal evolution of the cross polar cap potential over the last five hours of simulation. a) $\Sigma_P = 5$ mhos, b) $\Sigma_P = 10$ mhos. On the two plots the curves from the lowest to the highest represent runs from #1 to #7 , respectively (see Table 5.1).	105
5.2	A 3D illustration of the magnetic field lines attached to the locations of the extrema of the electrostatic potential in the ionosphere. The background represents the z-component of the plasma velocity in the GSM $z=1$ plane so that the reconnection line is easily identified. The magnitude of the parallel electric field is color coded and plotted over the field lines. Also, the electrostatic potential pattern on the inner boundary of the code is shown in color.	106

5.3	Potential drop between the field lines, $\Delta\Phi$, as a function of the distance from the inner boundary along the field line, d . The leftmost point on every curve lies on the inner boundary and represents the corresponding cross polar cap potential; the rightmost point corresponds to the potential between the field lines in the solar wind. a) $\Sigma_P = 5$ mhos, b) $\Sigma_P = 10$ mhos. On both plots the curves with the corresponding cross polar cap potential from the lowest to the highest represent runs from #1 to #7, respectively.	106
5.4	The dependence of the cross polar cap potential and reconnection potential, $\Delta\Phi$, on the solar wind convective electric field, E_y . The lines are a fit to the simulation data.	107
5.5	Contours of the constant term Φ_0 in α, β space. The parameters shown here result in the least squares error function which is less or equal than 20% of the minimum transpolar potential simulated for a given value of the ionospheric conductance. The dashed lines represent $\Sigma_P = 10$ mhos, while the solid lines are for $\Sigma_P = 5$ mhos.	108
5.6	The magnetopause and the bow shock for the run #7. The background is color coded plasma density on a logarithmic scale for $\Sigma_P = 5$ mhos. The curves are of the form $r = \kappa/(1 + \varepsilon \cos \theta)$ where κ and ε are found from subsolar and terminator distances determined by the density jump.	109

5.7	Profiles of E_y along the GSM x-axis in the magnetosheath for the run #7. The vertical dotted line represents the location of the point moved about $1 R_E$ toward the Sun from the magnetopause subsolar point as determined from the density jump (see Fig. 5.6). This is to make sure that numerical errors arising from the solution inside of the reconnection region are not included in the calculation. . . .	109
5.8	The dependence of the steady state transpolar potential on the solar wind dynamic pressure for the shown values of the ionospheric conductance and $E_y = 12$ mV/m for the solar wind electric field. The lines represent the best linear fit to the simulation data. . . .	110
6.1	The dependence on the ionospheric Pedersen conductance: a) of the cross polar cap potential (solid line) and the ionospheric field aligned current (dashed line); b) of the magnetopause size in the terminator plane, κ	130
6.2	Profile of B_x along the GSM y-axis in the terminator plane. The vertical dashed line denotes the location of the magnetopause as defined by the jump of the density.	131
6.3	a) A sketch of the current loop in the terminator plane. b) z-component of the current in the terminator plane on a logarithmic scale for $\Sigma_P = 10$ mhos.	132

6.4	The dependence of the cosine squared of the flaring angle on the squared magnitude of the ionospheric integrated field aligned current. The error bars show the error estimations assuming the accuracy of a distance measurement equal to $\sim 0.3 R_E$ based on the local code resolution.	133
6.5	The magnetosphere in the $z=1$ plane. The background is the plasma mass density on a logarithmic scale. The lines are the projections of 3D flow streamlines. a) $\Sigma_P = 1$ mho, b) $\Sigma_P = 10$ mhos.	134
6.6	The maximum v_z component of the plasma velocity measured along a streamline originated in the solar wind upstream of the bow shock in the $z = 1$ plane at a distance y_0 from the symmetry axis.	135
7.1	A block diagram of the phenomenological model of Φ_{PC} saturation.	141
7.2	Time evolution of the transpolar potential simulated without (the upper curve) and with (the lower curve) turbulent electron heating in the ionosphere.	141
7.3	Distributions of the electric field (a) and electrostatic potential (b) in the polar ionosphere for the simulations with anomalous heating switched off (on the left) and switched on (on the right). Parameters of simulations are: solar wind electric field $E_y = 16$ mV/m and background ionospheric Pedersen conductance $\Sigma_P^0 = 10$ mhos.	142

Chapter 1

Introduction

The earth's magnetosphere is a unique physical system providing a natural laboratory of plasmas existing in the near-Earth space. It is formed by the interaction of the flow of a hot plasma from the sun (solar wind) with the terrestrial dipole magnetic field. The interaction is highly complex: it is driven by a variety of physical processes starting from the formation of the solar flares and coronal mass ejections (CMEs) in the solar corona and its consequences are manifested in the near-Earth environment, i.e. in the ionosphere and on the surface of the earth.

In this dissertation we are primarily concerned with a "small" part of this immense system, namely, the interaction of the solar wind with the earth's magnetosphere and its effects on the ionosphere. The earth's magnetosphere is a cavity formed in the solar wind flow. The solar wind particles can not penetrate the earth's magnetic field because their motion is deflected due to the gyration (in the simplistic representation). The width of the boundary between the solar wind and the magnetosphere, the magnetopause, as well as the distance between the points of entrance and exit of the particle from the dipole field region are of

the order of the ion gyroradius. With typical values of the solar wind velocity (500 km/s) and the dipole magnetic field at the dayside magnetopause (about 30 nT) the ion gyroradius is ~ 150 km which is orders of magnitude smaller than the earth's radius. Thus, the reflection of the solar wind particles can be considered as ideal specular reflection. This picture is schematically depicted in Fig. 1.1. This description of the magnetosphere formation is, of course, only a zero order approximation: in fact, solar wind energetic particles can get through the boundary of the magnetosphere and initiate a number of processes that constitute the main body of the magnetospheric physics.

The magnetosphere has a complex multilayered structure. It is schematically represented in Fig. 1.2. A consequence of the supersonic solar wind flow (its speed typically ranges from 300 to 1400 km/s with 500 km/s being the most probable value) is the formation of the standing shock wave, the bow shock. When the decelerated subsonic solar wind flow encounters the earth's dipole magnetic field a boundary, the magnetopause, is formed. The region between the bow shock and the magnetopause is the magnetosheath. On the dayside, the dipole field is compressed to about twice its original value while on the nightside it stretches far out forming the regions of almost horizontally and oppositely directed magnetic fields, the tail lobes, where the plasma is dilute. The layer between the lobes with more dense plasma and weaker magnetic field is the plasma sheet. Such reconfiguration of the terrestrial magnetic field requires a system of currents which distorts the original magnetic field. The current flowing

along the surface of the magnetopause is known as the Chapman-Ferraro current. It participates in balancing the dynamic pressure of the solar wind by means of the $\vec{j} \times \vec{B}$ force. In the tail the current flows along the thin current sheet between the lobes producing the lobe magnetic field. The ionospheric current is also a part of a global magnetospheric current system. The field aligned currents flowing in and out of the ionosphere close partly across the magnetopause and partly through the cross-tail current. During highly disturbed storm-time conditions the ring current develops closer to the earth (typically, within $4 R_E$). Ionospheric field aligned currents also partly close through the ring current.

The fact that the solar wind particles can penetrate the magnetopause boundary makes magnetospheric physics rich in phenomena and complexity. Under some conditions the magnetosphere can become partially open to the solar wind due to magnetic reconnection. The solar wind plasma is infinitely conducting, and therefore the frozen-in theorem [*Landau and Lifshitz, 1985*] holds, meaning that if a field line passes through two given particles at some moment of time, it will do so at all times. When the interplanetary magnetic field (IMF) has a strong southward component, it is anti-parallel to the earth's dipole magnetic field on the dayside and, therefore, conditions for magnetic reconnection are created. Once the magnetic field is reconnected, a population of field lines arises that have one end connected to the ionosphere and the other end in the solar wind. This provides direct access of the solar wind energetic particles to the ionosphere. A concept of an "open" magnetosphere was first put forward

by *Dungey* [1961]. In Fig. 1.3 the sketch first made by *Dungey* [1961] is reproduced. Magnetic field lines reconnected at the dayside magnetopause are convected to the tail where the tail neutral line is formed and the field lines reconnect again and then convect back to the dayside. This is a picture of a global plasma convection pattern in the magnetosphere.

Within the ideal MHD description the electric field $\vec{E} = -\frac{1}{c}\vec{v} \times \vec{B}$ is perpendicular to a magnetic field line at any point and, therefore, in steady state, the magnetic field lines are equipotential. On the other hand, the electric field is also perpendicular to the velocity vector at any point so that the streamlines are also equipotential. This means that any fluid element frozen in the magnetic field retains its electrostatic potential. Thus, once there is a field line having one of the ends tied to the ionosphere and the other frozen in the solar wind, the trajectory of its ionospheric footprint is an equipotential with the value of the electrostatic potential mapped from the solar wind. The typical convection pattern formed in the polar ionosphere is depicted in Fig. 1.4. The points of minimum and maximum electrostatic potential lie on the boundary between the closed and open magnetic field lines and the potential difference between them is mapped directly from the dayside reconnection line. Hence, the difference between the extrema of electrostatic potential in the polar ionosphere is a very important indicator of the SW-M-I coupling. It is called the cross polar cap potential (CPCP) or the transpolar potential (TPP).

The main topic of this dissertation is to investigate the behavior of the CPCP

under varying solar wind and ionospheric conditions. We focus our interest on the observational evidence that the CPCP depends nonlinearly on the convective electric field in the solar wind, saturating at a level of about 150-200 kV when the upstream electric field exceeds a threshold of ~ 5 mV/m. This is a very fortunate property of the magnetosphere-ionosphere system. A large amount of the solar wind energy is prevented from directly accessing the ionosphere which limits the ionospheric response to the solar wind driver. Among the practical consequences of the effect are the reduced Joule ionospheric heating and saturation of the ionospheric currents that produce significantly weakened magnetic disturbances on the ground. Besides its practical importance, exploration of the saturation of the transpolar potential poses challenging problems for modern space plasma research. First, the effect is global in the sense that processes taking place in different parts of the SW-M-I system on different space scales (magnetosheath flow, magnetopause reconnection, ionospheric convection, etc.) should be taken into account. Further, as discussed in subsequent chapters, the ionospheric conductance plays a critical role in regulating the level of the CPCP saturation and therefore it provides a feedback on other parts of the SW-M-I system. Mechanisms for such a feedback are not well understood at present.

Global magnetohydrodynamic (MHD) simulations are a natural tool to study the effect of the CPCP saturation. The plasma in most regions of the SW-M-I system satisfies in the global sense the ideal one-fluid MHD equations on which the global MHD simulations are based. Despite the lack of proper microscopic

shock and reconnection physics, such models reproduce many global phenomena in the SW-M-I system and its geometry. As discussed in this dissertation the problem of CPCP saturation is in many respects a matter of geometry: The magnetopause is an obstacle in the way of the solar wind and a change in the geometry of the obstacle can affect greatly the properties of the flow past it.

This dissertation is organized as follows:

In Chapter 2 a brief introduction to global MHD simulation techniques is given. We discuss the initial set of one-fluid MHD equations and methods of their numerical solution. The description of the Lyon-Fedder-Mobarry (LFM) global MHD code [e.g. *Fedder and Lyon, 1995*] that was used throughout this dissertation is given, with particular emphasis on techniques employed for incorporation of magnetic reconnection processes in the simulation. The idealized Ohm's law does not contain terms responsible for the magnetic reconnection and therefore, special methods need to be applied in the global MHD simulations to provide a plausible representation of the phenomena in the SW-I-M system.

Chapter 3 addresses effects of the solar wind activity on the ionospheric conductance. As discussed in subsequent chapters, the latter is the crucial quantity in determining the magnitude of the cross polar cap potential in the saturation domain. Specific emphasis is placed on the influence of the solar wind electric field (the basic indicator of the coupling in the SW-M-I system) on the ionospheric conductance, since the tendency of the conductance to grow with the increasing IEF facilitates the CPCP saturation.

In Chapter 4 we give an overview of the observational evidence for the CPCP saturation. The CPCP is measured using a number of techniques including satellite and ground observations as well as assimilative ionospheric models. Additionally, Chapter 4 includes a description of the Hill/Siscoe model that provides theoretical arguments for the saturation of the transpolar potential.

Chapters 5 and 6 comprise the main body of the research. Chapter 5 presents results of the global MHD modeling of the magnetosphere under strong solar wind conditions corresponding to a strong geomagnetic storm. The simulations confirm the CPCP saturation, but the level of saturation is shown to be strongly dependent on the ionospheric conductance. In this chapter we show that the saturation of the CPCP follows from the saturation of the dayside reconnection potential, which is formed by the magnetosheath flow past the magnetopause.

Chapter 6 is devoted to a thorough study of the ionospheric conductance influence on the reconnection and transpolar potentials. The feedback of the conductance on the magnetosheath flow, its deflection by the magnetopause, and the formation of the reconnection potential are considered. Finally, in the last chapter we summarize our results and formulate a phenomenological model of the CPCP saturation

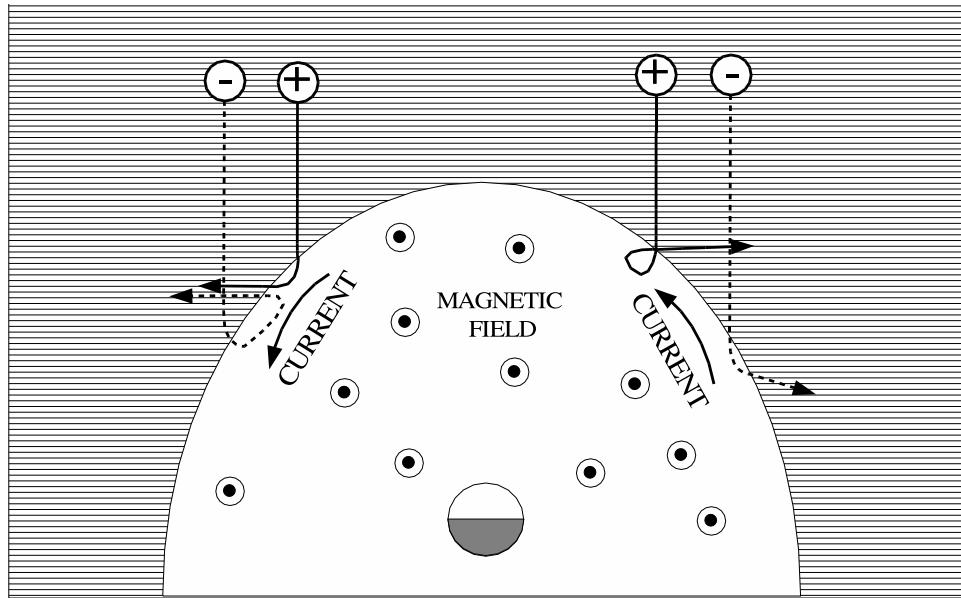


Figure 1.1: Schematic illustration of trajectories of positive ions (+) and electrons (-) incident on the planetary magnetic field.

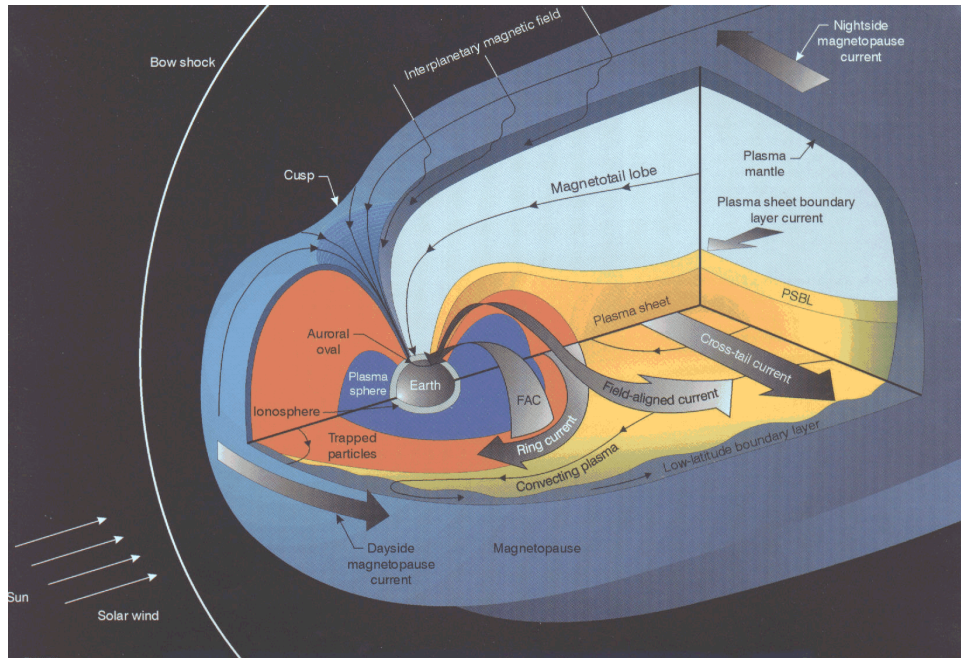


Figure 1.2: Schematic representation of the magnetosphere showing the solar wind flow, the general structure of the magnetosphere, and the magnetospheric current system.

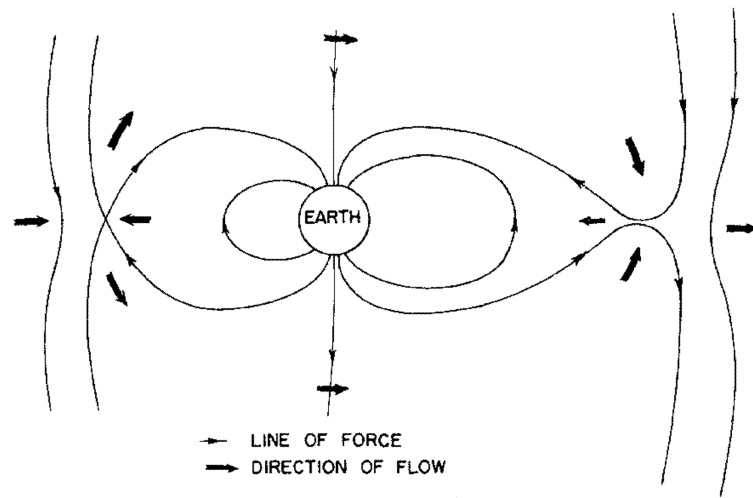


Figure 1.3: Reconnection model of the magnetosphere with southward IMF [after *Dungey*, 1961]

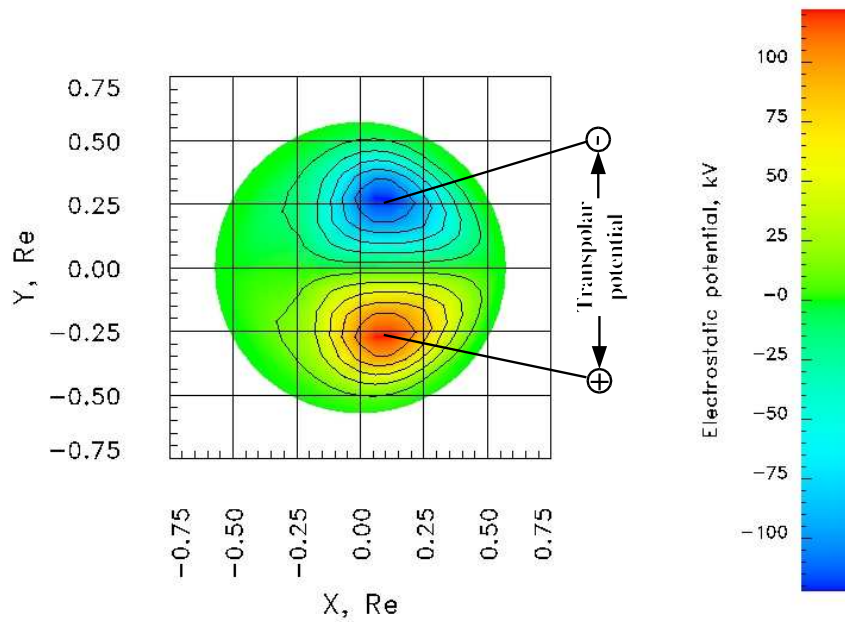


Figure 1.4: Typical convection pattern in the polar ionosphere. The distribution of the electrostatic potential is shown along with the equipotential lines. GSM coordinate system is used. The figure is obtained from global MHD simulations.

Chapter 2

Global MHD Modeling of the Earth's Magnetosphere

Global MHD models provide a powerful tool for investigation of the magnetospheric dynamics. They are so far the only numerical means by which the global interactions in the SW-M-I system can be studied, although they lack accurate description of important physical processes such as magnetic reconnection and MHD discontinuities and shocks. Global MHD codes solve numerically the system of the ideal MHD equations for the magnetosphere, with the solar wind and the ionosphere providing the inflow-outflow and the inner boundary conditions, respectively. In this chapter we consider the system of the ideal MHD equations and their applicability to the magnetosphere, discuss the general methods for their numerical solution, and describe the Lyon-Fedder-Mobarry (LFM) model used for the calculations in this dissertation.

2.1 Ideal Magnetohydrodynamics and its Validity for the Magnetospheric Plasmas

The system of the ideal MHD equations [e.g. *Freidberg, 1987; Landau and Lifshitz, 1985*] put in the fully conservative form is

$$\frac{\partial \rho}{\partial t} + \nabla \cdot (\rho \vec{v}) = 0 \quad (2.1)$$

$$\frac{\partial \rho \vec{v}}{\partial t} + \nabla \cdot \left[\rho \vec{v} \otimes \vec{v} + \left(p + \frac{B^2}{8\pi} \right) \bar{\mathbf{I}} - \frac{\vec{B} \otimes \vec{B}}{4\pi} \right] = 0 \quad (2.2)$$

$$\frac{\partial U}{\partial t} + \nabla \cdot \left[\vec{v} \left(U + p + \frac{B^2}{8\pi} \right) - \frac{\vec{B} (\vec{v} \cdot \vec{B})}{4\pi} \right] = 0 \quad (2.3)$$

$$\frac{\partial \vec{B}}{\partial t} + \nabla \cdot (\vec{v} \otimes \vec{B} - \vec{B} \otimes \vec{v}) = 0. \quad (2.4)$$

Here $\bar{\mathbf{I}}$ is the unity matrix, \otimes denotes dyadic multiplication of vectors and U is the total energy:

$$U = \frac{\rho v^2}{2} + \frac{p}{\gamma - 1} + \frac{B^2}{8\pi}. \quad (2.5)$$

This system of equations should be closed with the equation of the solenoidal magnetic field:

$$\nabla \cdot \vec{B} = 0. \quad (2.6)$$

The system of equations implies the ideal Ohm's law:

$$\vec{E} = -\frac{1}{c} \vec{v} \times \vec{B} \quad \text{and} \quad (2.7)$$

$$\vec{j} = \frac{c}{4\pi} \nabla \times \vec{B}, \quad (2.8)$$

i.e. the displacement current is neglected.

The validity of ideal magnetohydrodynamics is determined from the condition that no distinction is made between the different plasma species. This means that the time-scale of variations of fluid and fields should be larger than the characteristic time scale of the heaviest plasma component. This restricts consideration to small frequencies and large spacial scales, i.e. the characteristic frequency of any change should be smaller than the ion gyrofrequency:

$$\omega < \omega_{gi} \quad (2.9)$$

and the characteristic length scale, L , should be greater than the ion gyroradius:

$$L > r_{gi}. \quad (2.10)$$

At such low frequencies one can usually neglect the displacement current.

In addition to the above restrictions, the conditions arising from neglecting different terms in the generalized Ohm's law apply. Before proceeding to the assessment of different terms in the generalized Ohm's law it is helpful to briefly outline its derivation. One starts by writing the equations of motion for electrons and ions:

$$n_e m_e \frac{d\vec{v}_e}{dt} = -\nabla \bar{P}_e - n_e e \left(\vec{E} + \frac{1}{c} \vec{v}_e \times \vec{B} \right) + \vec{R}_e \quad (2.11)$$

$$n_i m_i \frac{d\vec{v}_i}{dt} = -\nabla \bar{P}_i + n_i e \left(\vec{E} + \frac{1}{c} \vec{v}_i \times \vec{B} \right) - \vec{R}_e, \quad (2.12)$$

where \vec{R}_e is the resistive force due to the ion-electron collisions and \bar{P}_e and \bar{P}_i stand for the electron and ion pressure tensors, respectively. Making use of the

definition of one-fluid quantities,

$$n \simeq n_i,$$

$$\vec{v} \simeq \vec{v}_i, \quad \text{and}$$

$$\vec{j} = ne(\vec{v}_i - \vec{v}_e),$$

from (2.11) one easily obtains

$$\vec{E} + \frac{1}{c}\vec{v}_e \times \vec{B} = -\frac{\nabla \bar{P}_e}{ne} - \frac{m_e}{e} \frac{d\vec{v}_e}{dt} + \frac{\vec{R}_e}{ne}. \quad (2.13)$$

The conventional form of the generalized Ohm's law is found if one adds $\frac{1}{c}\vec{v}_i \times \vec{B}$ to each side of (2.13) and makes a substitution $\vec{R}_e = \eta ne\vec{j}$:

$$\vec{E} + \frac{1}{c}\vec{v} \times \vec{B} = \eta\vec{j} - \frac{m_e}{e} \frac{d\vec{v}_e}{dt} - \frac{1}{ne} \nabla \cdot \bar{P}_e + \frac{1}{nec} \vec{j} \times \vec{B}, \quad (2.14)$$

where η is the plasma resistivity. Equation (2.14) assumes quasi-neutral plasma and $m_e \ll m_i$. Besides, the effect of ion-electron collisions is represented by the simple resistivity term $\eta\vec{j}$ instead of the appropriate collision integral.

Otherwise, (2.14) is a rigorous consequence of the Boltzmann equation.

The ratio of each term on the right-hand side of (2.14) to the terms on the left can be expressed as an appropriate characteristic length divided by the length scale for gradients in the system. The characteristic lengths associated with the four terms on the right-hand side of (2.14) are the following:

- First term: $\lambda_\eta v_a/v$, where λ_η is the resistive (or diffusion) length and v_a is the Alfvén speed.

- Second term (electron inertia): λ_e , the electron inertial length or collisionless skin depth.
- Third term (electron pressure gradient): $\lambda_i \beta^{1/2}$.
- Fourth term (Hall effect): λ_i , the ion inertial length.

The definitions of the above quantities are: $\lambda_\eta = \eta c^2 / 4\pi v_a$, $\lambda_e = c / \omega_{pe}$, and $\lambda_i = c / \omega_{pi}$. When the gradient length scale is much larger than any of these characteristic lengths, (2.14) reduces to (2.8). An informative discussion on this subject can be found in [Vasyliunas, 1975; Drake, 1995].

A posteriori comparison of MHD simulations to the observations show that the ideal MHD equations describe SW-M-I plasma interactions considerably well in regions that include solar wind, magnetosheath, tail lobes, and plasma sheet. The magnetopause and neutral sheet require a kinetic description of the plasma.

2.2 Numerical Solution of the Ideal MHD Equations

2.2.1 Finite-Volume Methods

It is a well known problem that the quality of a numerical solution of the hydrodynamic (and magnetohydrodynamic) equations depends on the form in which these equations are written [e.g. Durrant, 1999]. In fact, it was shown by Lax [1954] that only the finite-differencing of the equations written in the conservative form gives adequate results with shocks placed in the right locations. The numerical methods based on the solution of the equations in conservation (or

”flux”) form are called *finite-volume methods*. They automatically conserve mass, momentum and energy throughout the simulation.

Let’s consider a general 1-d conservation equation:

$$\frac{\partial \psi}{\partial t} + \frac{\partial f(\psi)}{\partial x} = 0. \quad (2.15)$$

Its finite-difference approximation in the finite-volume approach is given by

$$\psi_i^{n+1} = \psi_i^n - \frac{\Delta t}{\Delta x} [F_{i+1/2} - F_{i-1/2}]. \quad (2.16)$$

Here ψ and f are determined in the center of the i th spatial grid cell and n th temporal grid cell. The $F_{i\pm 1/2}$ are called transportive fluxes, and are functions of f at one or more of the time levels t^n . The functional dependence of F on f is defined by a particular integration scheme.

2.2.2 Flux-Limiter Methods

The choice of the integration scheme depends on the physical system under the consideration. However, a general statement that can be made about the finite-volume schemes is that neither low-order schemes nor high-order ones are perfect for modeling systems with sharp gradients of quantities. Low-order schemes possess an unacceptably high level of diffusion, i.e. the shocks can be smeared over a large number of spacial cells. On the other hand, high-order schemes while capturing the width of discontinuities better, suffer from dispersive oscillations non-existent in the original solution. To avoid the above problems *Boris and Book* [1973] suggested the Flux-Corrected Transport (FCT)

method which takes advantage of both approaches. The idea is to mix a low-order and a high-order scheme in such a way that the numerical diffusion is minimized while no new extrema are created in the solution. Before describing the FCT algorithm let's illustrate how it works using a similar but simpler approach, a so called flux-limiter method.

We start by considering a simple 1-d advection equation (i.e. (2.15) with $F(\psi) = c\psi$):

$$\frac{\partial \psi}{\partial t} + \frac{\partial (c\psi)}{\partial x} = 0, \quad (2.17)$$

where c is the constant representing the propagation speed. Suppose, the initial condition is a step-function:

$$\psi(x, 0) = \begin{cases} 0, & x < 0 \\ 1, & x \geq 0. \end{cases} \quad (2.18)$$

We want to see how the shock is propagated in time by three schemes: a low-order, a high-order and a hybrid (flux-limiter). The idea of the flux-limiter method is to calculate the fluxes at the cell interfaces using a low-order and a high-order scheme and construct the total flux that will be used in (2.16) by the following formula:

$$F_{j+1/2} = F_{j+1/2}^l + C_{j+1/2} (F_{j+1/2}^h - F_{j+1/2}^l), \quad (2.19)$$

where $F_{j+1/2}^l$ and $F_{j+1/2}^h$ are the fluxes calculated by the low-order and high-order schemes, respectively. $C_{j+1/2}$ is the multiplicative limiter. It is a number between

0 and 1 describing the amount of mixing between the low-order and high-order fluxes. The limiter is calculated as a nonlinear function of the local solution $C(r_{j+1/2})$, where

$$r_{j+1/2} = \frac{\psi_j - \psi_{j-1}}{\psi_{j+1} - \psi_j} \quad (2.20)$$

is the ratio of the slope of the solution across the cell interface upstream of $j + 1/2$ to the slope of the solution across the interface at $j + 1/2$. The parameter $r_{j+1/2}$ is approximately unity where the numerical solution is smooth and is negative when there is a local maximum or minimum immediately upstream of the cell interface at $j + 1/2$. There are a number of choices for the specific functional form of $C(r)$. Here we use the "minmod" limiter:

$$C(r) = \max[0, \min(1, r)]. \quad (2.21)$$

The comparison of the low-order, high-order and hybrid scheme is shown in Fig. 2.1. In this example, a low-order flux is computed using the upstream-differencing (or donor cell) scheme:

$$F_{j+1/2}^l = \frac{c}{2} (\psi_j + \psi_{j+1}) - \frac{|c|}{2} (\psi_{j+1} - \psi_j) \quad (2.22)$$

and the high-order flux is computed using the Lax-Wendroff method:

$$F_{j+1/2}^h = \frac{c}{2} (\psi_j + \psi_{j+1}) - \frac{c^2 \Delta t}{2\Delta x} (\psi_{j+1} - \psi_j). \quad (2.23)$$

The calculations were conducted with the Courant number $c\Delta t/\Delta x$ equal to 0.5. The shock was propagated for 50 time steps and its initial position was

$x=10$. Fig. 2.1 shows advantages of the flux-limiter method: it removes the dispersive oscillations produced by the high-order (Lax-Wendroff) scheme upstream of the shock while limiting the diffusion of the low-order scheme (upstream differencing).

2.2.3 Flux-Corrected Transport

A more involved analogue of the flux-limiter method is the flux-corrected transport algorithm mentioned above. A detailed description of the method can be found in [Zalesak, 1979]. The outline of the algorithm is as follows:

1. Compute $F_{j+1/2}^l$, the transportive flux given by some low order scheme guaranteed to give monotonic (no dispersive oscillations) results for the problem at hand
2. Compute $F_{j+1/2}^h$, the transportive flux given by some high order scheme
3. Define the "antidiffusive flux":

$$A_{j+1/2} \equiv F_{j+1/2}^h - F_{j+1/2}^l$$

4. Compute the updated low order ("transported and diffused") solution:

$$\psi_j^{td} = \psi_j^n - \frac{\Delta t}{\Delta x} [F_{j+1/2}^l - F_{j-1/2}^l]$$

5. Limit the $A_{j+1/2}$ so that ψ^{n+1} as calculated in step 6 below is free of extrema not found in ψ^{td} or ψ^n :

$$A_{j+1/2}^C = C_{j+1/2} A_{j+1/2}, \quad 0 \leq C_{j+1/2} \leq 1$$

6. Apply the limited antidiffusive fluxes:

$$\psi_j^{n+1} = \psi_j^{td} - \frac{\Delta t}{\Delta x} [A_{j+1/2}^C - A_{j-1/2}^C]$$

A choice of the flux limiter $C_{j+1/2}$ is, of course, the crucial step in the above procedure. The requirements to the limiter are described in step 5: it should be chosen in such a manner that it minimize the diffusion and do not generate new extrema in the solution. The algorithm for the choice of the limiter is presented in [Zalesak, 1979].

The generalization of the above algorithm for the case of multidimensional problems is more algebraically involved and, therefore, will not be reproduced here. The Lyon-Fedder-Mobarry model uses the eight-order flux formulas as described in [Zalesak, 1979]. As a finite-volume technique the FCT method when applied to the ideal MHD equations guarantees that the shocks will be placed at the right locations and will be resolved to about 2 grid points without producing unphysical oscillations. The properties of the plasmas on both sides of the shocks will satisfy Rankine-Hugoniot relations but the microphysics of the shocks and discontinuities will, of course, not be captured. A similar approach is taken to the magnetic reconnection. We will conclude this chapter with several remarks on how the problem of magnetic reconnection is tackled in global MHD simulations (see 2.2.5).

2.2.4 Treatment of the Magnetic Field

As pointed out in [Stone and Norman, 1992] one of the most serious difficulties in MHD numerical simulations is the necessity to maintain the solenoidal nature of the magnetic field. The incapability of a code to ensure the condition $\nabla \cdot \vec{B} = 0$ leads to unphysical solutions with field-aligned forces and non-conservation of magnetic flux, momentum and energy [Brackbill and Barnes, 1980]. The LFM model uses the staggered-mesh technique which was first proposed by Yee [1966] for electromagnetic problems and later applied to the numerical solution of the MHD equations by Evans and Hawley [1988] and Stone and Norman [1992]. The above references provide an informative discussion on this subject. Here, we will briefly outline the algorithm.

The main idea of the staggered mesh technique is to develop a numerical scheme which ensures a divergence-free magnetic field "by construction". This is achieved by the proper centering of the variables. The divergence free field flux through any closed surface is equal to 0. On the other hand, the integral form of the Faraday's law (2.4) reads

$$\frac{\partial \Phi_S}{\partial t} = - \oint_{\ell} \vec{E} \cdot d\vec{l} = \oint_{\ell} (\vec{v} \times \vec{B}) \cdot d\vec{l}, \quad (2.24)$$

where Φ_S is the magnetic flux through the surface S bounded by the closed curve ℓ . This equation shows that it is natural to define magnetic fields, fluxes, and velocities at the center of the cell faces and to place electric fields along the cell edges as it is shown in Fig. 2.2. The value e_i is given by $v_j B_k - v_k B_j$ where

$\{ijk\} = \{xyz\}$, $\{yzx\}$, or $\{zxy\}$. Then the line integral is easily identified in (2.24) as the sum of electric fields multiplied by the length of the cell edges and can be easily shown to be identically equal to 0:

$$\begin{aligned}
\frac{\partial \Phi_S}{\partial t} &= \frac{\partial B_x(i-1/2, j, k)}{\partial t} \Delta y \Delta z + \frac{\partial B_x(i+1/2, j, k)}{\partial t} \Delta y \Delta z + \\
&\quad \frac{\partial B_y(i, j-1/2, k)}{\partial t} \Delta x \Delta z + \frac{\partial B_y(i, j+1/2, k)}{\partial t} \Delta x \Delta z + \\
&\quad \frac{\partial B_z(i, j, k-1/2)}{\partial t} \Delta x \Delta y + \frac{\partial B_z(i, j, k+1/2)}{\partial t} \Delta x \Delta y = \\
&\quad [-e_y(i-1/2, j, k+1/2) + e_y(i-1/2, j, k-1/2)] \Delta y + \\
&\quad [-e_y(i+1/2, j, k+1/2) + e_y(i+1/2, j, k-1/2)] \Delta y + \\
&\quad \dots \equiv 0,
\end{aligned} \tag{2.25}$$

since each electric field component contributes to the total path integral twice: one time in one direction and the other time in the opposite direction (as depicted in Fig. 2.2 by arrows). Therefore, the magnetic flux through the surface bounding each grid cell is maintained constant throughout the simulation. So, if the magnetic flux in a cell is 0 initially, it will continue to do so and, thus, the solenoidal nature of the magnetic field will be ensured at all times.

2.2.5 Treatment of Magnetic Reconnection

As mentioned above, the ideal MHD equations do not allow for magnetic reconnection to occur. However, magnetic reconnection and energy release can result from convection. Numerical merging of magnetic field occurs when oppositely directed magnetic fields are convected into a computation cell causing their numerical averaging and annihilation due to the finite cell size [e.g.

Goodrich et al., 2001]. The LFM model is designed in such a manner that the numerical magnetic field and plasma diffusion is very small. However, there are usually steep gradients of the magnetic field in regions where magnetic reconnection takes place. This results in increase of numerical diffusion as it is described in sections 2.2.1, 2.2.2 and 2.2.3. Due to the existence of the numerical diffusion the RHS of (2.4) is no longer zero:

$$\frac{\partial \vec{B}}{\partial t} + \nabla \cdot (\vec{v} \otimes \vec{B} - \vec{B} \otimes \vec{v}) = \vec{R}', \quad (2.26)$$

which is equivalent to the appearance of an effective "non-ideal" term in the Ohm's law so that

$$\vec{E} = -\frac{1}{c} \vec{v} \times \vec{B} + \vec{R}, \quad (2.27)$$

where \vec{R} comprises different non-ideal effects that can govern magnetic reconnection in realistic plasmas. As previously mentioned the LFM model uses a hybrid scheme which applies diffusion in a non-linear manner depending on local conditions and, thus, it is not possible to define the global value of the numerical resistivity. This means that quantities like the reconnection rate will be controlled by the global character of the solution and the boundary conditions.

2.3 The Lyon-Fedder-Mobarry Global MHD Model

The LFM code consists of two interlinked simulations for modeling the magnetosphere and ionosphere [*Fedder et al.*, 1995a; *Fedder and Lyon*, 1995; *Mobarry et al.*, 1996]. The solar wind and magnetospheric plasmas are modeled

via solution of the ideal MHD equations using the methods described above. In the subsection 2.3.1 the actual grid of the code as well as the boundary conditions used are discussed. The ionosphere is modeled by solving a height integrated electrostatic model that is coupled to the magnetospheric solution. This is discussed in subsection 2.3.2.

2.3.1 The LFM Grid and MHD Boundary Conditions

The ideal MHD equations are solved in an approximately cylindrical volume containing the magnetosphere and the solar wind. A typical spatial grid configuration for the LFM is shown in Fig. 2.3. The full 3D grid can be obtained by rotating the plane depicted in Fig. 2.3 around its longest axis. The dimensions of the grid used in the calculations for this dissertation are as follows: the radius of the cylinder is approximately $60 R_E$; the x-axis extends to $30 R_E$ on the dayside and to $300 R_E$ on the nightside. The grid places the maximal resolution in critical locations: the bow shock, magnetopause, magnetotail, and ionosphere.

Time series of solar wind plasma and field parameters are applied at the upstream and side boundaries of the calculation while supersonic outflow is assumed at the downstream boundary. This boundary is located far enough in the tail that the plasma is once again super-Alfvenic, and thus the boundary is electromagnetically disconnected from the ionosphere and upstream plasma. A geocentric sphere of $3.5 R_E$ in radius is removed to form the inner boundary condition at which the magnetospheric solution is matched to an ionospheric

simulation.

Since the 3D structure of the solar wind usually cannot be resolved with existing number of upstream satellites, the front of the solar wind is taken to be a plane front with constant plasma quantities along it. This imposes a strict condition on the solar wind magnetic field: its solenoidal nature requires that

$$\vec{n} \cdot \vec{B} = d = \text{const.} \quad (2.28)$$

The above condition means nothing more than that, since the magnetic field components lying in the plane of the front are constant, the component normal to the front should obey

$$\frac{\partial B_n}{\partial n} = 0. \quad (2.29)$$

Thus, if the plane of the front is taken to be yz-plane of the simulation the above condition requires B_x to be constant in time, which poses a serious problem when simulating real events. On the other hand, if the plane of the front is tilted so that

$$\vec{n} = \alpha \hat{i} + \beta \hat{j} + \gamma \hat{k} \quad (2.30)$$

Equation (2.29) results in

$$\alpha B_x + \beta B_y + \gamma B_z = d \quad (2.31)$$

and redefining B_x as

$$B_x(t) = \frac{1}{\alpha} (d - \beta B_y(t) - \gamma B_z(t)) \quad (2.32)$$

we eliminate the problem. In practice, we use a linear regression technique to construct a new $B_x(t)$ time series satisfying (2.32) and as close to the original $B_x(t)$ as possible.

2.3.2 The Ionospheric Simulation

The ionospheric simulation supplies the inner boundary condition for the MHD solution in the magnetosphere. It provides the electric field in the ionosphere by solving a two-dimensional height-integrated electrostatic potential equation driven by the field aligned currents within the magnetosphere,

$$\nabla_{\perp} (\Sigma \cdot \nabla_{\perp} \Phi) = j_{\parallel} \sin \theta, \quad (2.33)$$

where Φ is the ionospheric potential, Σ is the anisotropic ionospheric conductance (i.e. height-integrated conductivity) tensor, and θ is the dipole tilt angle [e.g. *Baumjohann and Treumann, 1996*]. The j_{\parallel} term stands for the absolute value of the parallel current density and describes the coupling between the magnetosphere and ionosphere. The field-aligned currents are determined at the inner magnetospheric boundary and are then mapped instantaneously along dipole field lines to the ionosphere. The ionospheric solution for the electric field \vec{E} is then mapped back to this boundary and used to define the boundary condition for the plasma velocity via

$$\vec{v} = \frac{(-\nabla\Phi) \times \vec{B}}{B^2}. \quad (2.34)$$

The numerical solution for the ionospheric parameters strongly depends on the conductance tensor. The detailed empirical model for calculating the anisotropic

conductivity tensor in the LFM is presented by *Fedder et al.* [1995b]. Briefly, the model consists of two parts. The first part comes from the steady solar EUV flux and the second from particle precipitation in the auroral region.

Using DMSP and radar data *Robinson et al.* [1987] have developed an empirical method for determining the auroral contributions to the Pedersen and Hall conductivities,

$$\delta\Sigma_P = \frac{5E^{3/2}\phi^{1/2}}{1 + 0.0625E^2} \quad (2.35)$$

$$\delta\Sigma_H = 0.45E^{0.85}\delta\Sigma_P, \quad (2.36)$$

where E and ϕ are the energy and flux of the precipitating electrons.

Using the work of *Chiu and Cornwall* [1980]; *Chiu et al.* [1981]; *Orens and Fedder* [1978], the energy and flux of precipitating electrons in the LFM are determined from the MHD quantities within the inner most grid cells. First a provisional set of energy, E_0 and flux, ϕ_0 , values are determined from thermal speed, c_s , and density, ρ using

$$E_0 = \alpha c_s^2 \quad (2.37)$$

$$\phi_0 = \beta \rho E_0^{1/2}. \quad (2.38)$$

The parameters α and β are numbers of order one determined empirically to set the Pedersen and Hall conductivities to reasonable values. The flux of precipitating electrons is modified to include the effects of field aligned potential

drops,

$$E_{\parallel} = \frac{Rj_{\parallel}E_0^{1/2}}{\rho} \quad (2.39)$$

and geomagnetic mirroring to be

$$\phi = \begin{cases} \phi_0 \left(8 - 7e^{-\frac{E_{\parallel}}{7E_0}} \right), & E_{\parallel} \geq 0 \\ \phi_0 = e^{\frac{E_{\parallel}}{E_0}}, & E_{\parallel} < 0. \end{cases} \quad (2.40)$$

While the energy of precipitating electrons is simply

$$E = E_0 + E_{\parallel}. \quad (2.41)$$

In fact, for the results of this dissertation the LFM model was run with the ionospheric module "switched off", that is the ionospheric conductance was set robustly at the values specified. In this way, a parametric dependence of the system on the ionospheric conductance can be studied, which was one of the goals of the dissertation.

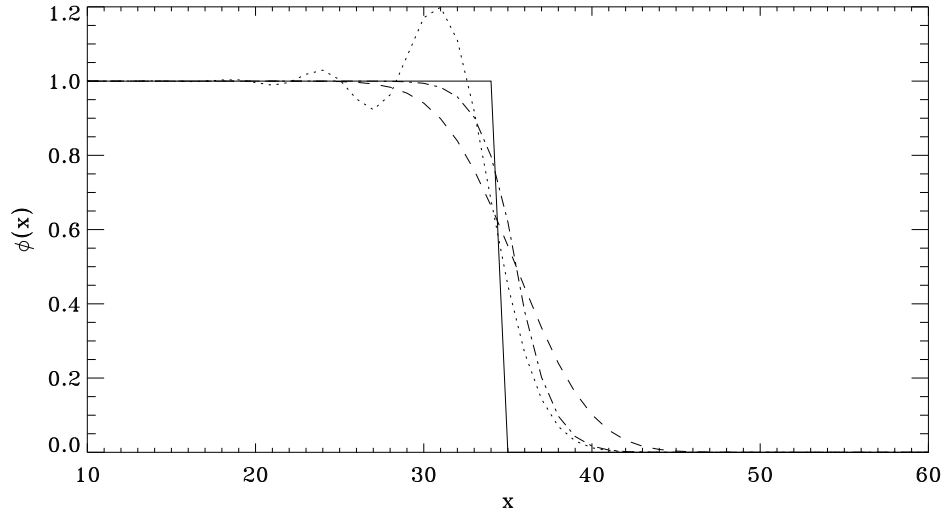


Figure 2.1: Results from the numerical solution of 1-d advection equation with constant speed: exact solution (solid), upstream (dashed), Lax-Wendroff (dotted), flux-limiter combination of upstream and Lax-Wendroff methods (dash-dotted).

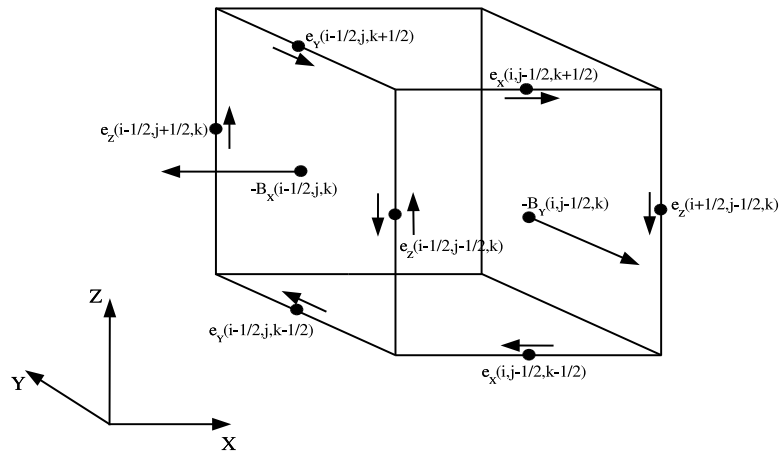


Figure 2.2: Centering of the magnetic fluxes and electric fields in a grid cell ensuring the divergence free magnetic field. The center of the cell has coordinates (i, j, k) . The arrows along the edges show the direction of the path integral in the Faraday's law.

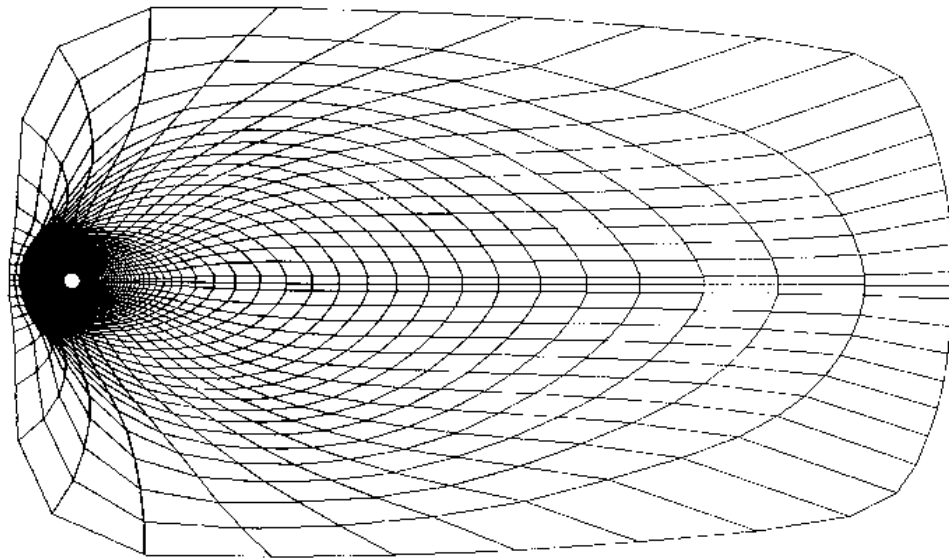


Figure 2.3: A 2D cut of the LFM simulation grid. The full 3D grid is recovered by rotating the depicted grid about the long axis by uniformly spaced azimuthal angles.

Chapter 3

Effects of the Solar Wind Activity on the Ionospheric Conductance

An important aspect of the strongly driven SW-M-I system is the changes in the ionospheric conductance induced by the solar wind activity. There are generally two causes for such changes. The conventional cause is the energetic charged particle precipitation which enhances the electron density in the E and F layers of the ionosphere. More recently [*Ossakow et al.*, 1975; *Dimant and Milikh*, 2003] it was noted that, for large ionospheric electric fields, anomalous electron heating due to the development of the Farley-Buneman instability at the electrojet altitudes results in enhanced conductance. The two effects are, in fact, strongly related, since the Farley-Buneman instability only develops in a plasma with high enough convective electric field, which is usually the case for storm-like conditions, that result in auroral precipitation as well. In this chapter the two effects are discussed, preceded by a brief derivation of the ionospheric conductivity tensor.

3.1 Conductivity Tensor of Partially Ionized Plasma

In this chapter we are primarily concerned with a partially ionized plasma that populates the E -layer of the ionosphere (90-120 km altitude). These are the altitudes of nominal maximum ionization of the disturbed ionosphere, where the

ion-electron collisions can be neglected ($\nu_{ei} \ll \nu_{in}, \nu_{en}$), and the ions become at least partially unmagnetized due to frequent ion-neutral collisions. The effects of turbulent electron heating are mostly seen at these altitudes [*Ossakow et al.*, 1975; *Schlegel and St.-Maurice*, 1981; *Stauning and Olesen*, 1989; *St.-Maurice*, 1987; *St.-Maurice and Laher*, 1985].

Let us briefly outline the derivation of the conductivity tensor for a partially ionized plasma in a magnetic field, which will be extensively used in the subsequent sections. We start by writing the equations of motion for ions and electrons neglecting pressure gradient, gravitational force, inertia, and electron-ion collisions:

$$e \left(\vec{E} + \frac{1}{c} \vec{v}_i \times \vec{B} \right) - m_i \nu_{in} (\vec{v}_i - \vec{v}) = 0 \quad (\text{for ions}) \quad (3.1)$$

$$-e \left(\vec{E} + \frac{1}{c} \vec{v}_e \times \vec{B} \right) - m_e \nu_{en} (\vec{v}_e - \vec{v}) = 0 \quad (\text{for electrons}), \quad (3.2)$$

where ν_{in} and ν_{en} are the frequencies of ion-neutral and electron-neutral collisions, \vec{v} is the bulk velocity of neutrals, and all other terms have their usual meaning. Our goal is to find \vec{v}_e and \vec{v}_i from (3.1) and (3.2) and, substituting to $\vec{j} = n_e e (\vec{v}_i - \vec{v}_e)$, obtain the relation between the current density and the electric field.

For the sake of simplicity, we choose the system of coordinates in such a way, that the magnetic field points in the z-direction. In this case, the cross-product of

the velocity and the magnetic field can be easily written in the matrix form:

$$\vec{v}_{i,e} \times \vec{B} = B \begin{bmatrix} 0 & 1 & 0 \\ -1 & 0 & 0 \\ 0 & 0 & 0 \end{bmatrix} \vec{v}_{i,e}, \quad (3.3)$$

where B is the magnetic field magnitude. Carrying out simple algebraic

calculations using (3.3), from (3.1) and (3.2) we obtain:

$$\vec{v}_i = \begin{bmatrix} \frac{\nu_{in}}{\Delta_i} & \frac{\Omega_i}{\Delta_i} & 0 \\ -\frac{\Omega_i}{\Delta_i} & \frac{\nu_{in}}{\Delta_i} & 0 \\ 0 & 0 & \frac{1}{\nu_{in}} \end{bmatrix} \left(\frac{e}{m_i} \vec{E} + \nu_{in} \vec{v} \right) \quad (3.4)$$

$$\vec{v}_e = \begin{bmatrix} \frac{\nu_{en}}{\Delta_e} & -\frac{\Omega_e}{\Delta_e} & 0 \\ \frac{\Omega_e}{\Delta_e} & \frac{\nu_{en}}{\Delta_e} & 0 \\ 0 & 0 & \frac{1}{\nu_{en}} \end{bmatrix} \left(-\frac{e}{m_e} \vec{E} + \nu_{en} \vec{v} \right), \quad (3.5)$$

where we have introduced $\Delta_i = \nu_{in}^2 + \Omega_i^2$ and $\Delta_e = \nu_{en}^2 + \Omega_e^2$, and $\Omega_{i,e} = eB/m_{i,e}c$ are ion and electron gyro-frequencies, respectively.

Let us now substitute the obtained expressions for the electron and ion velocities into the equation for the current density:

$$\vec{j} = \bar{\sigma} \vec{E} + \bar{\rho} \vec{v}, \quad (3.6)$$

where $\bar{\sigma}$ and $\bar{\rho}$ are tensors given by

$$\bar{\sigma} = n_e e^2 \begin{bmatrix} \frac{\nu_{in}}{m_i \Delta_i} + \frac{\nu_{en}}{m_e \Delta_e} & \frac{\Omega_i}{m_i \Delta_i} - \frac{\Omega_e}{m_e \Delta_e} & 0 \\ -\frac{\Omega_i}{m_i \Delta_i} + \frac{\Omega_e}{m_e \Delta_e} & \frac{\nu_{in}}{m_i \Delta_i} + \frac{\nu_{en}}{m_e \Delta_e} & 0 \\ 0 & 0 & \frac{1}{m_i \nu_{in}} + \frac{1}{m_e \nu_{en}} \end{bmatrix} \quad (3.7)$$

and

$$\bar{\rho} = n_e e \begin{bmatrix} \frac{\nu_{in}^2}{\Delta_i} - \frac{\nu_{en}^2}{\Delta_e} & \frac{\Omega_i \nu_{in}}{\Delta_i} + \frac{\Omega_e \nu_{en}}{\Delta_e} & 0 \\ -\frac{\Omega_i \nu_{in}}{\Delta_i} - \frac{\Omega_e \nu_{en}}{\Delta_e} & \frac{\nu_{in}^2}{\Delta_i} - \frac{\nu_{en}^2}{\Delta_e} & 0 \\ 0 & 0 & 0 \end{bmatrix}. \quad (3.8)$$

Let us introduce

$$\sigma_P = n_e e^2 \left(\frac{\nu_{in}}{m_i \Delta_i} + \frac{\nu_{en}}{m_e \Delta_e} \right), \quad (3.9)$$

$$\sigma_H = n_e e^2 \left(\frac{\Omega_e}{m_e \Delta_e} - \frac{\Omega_i}{m_i \Delta_i} \right), \quad \text{and} \quad (3.10)$$

$$\sigma_0 = n_e e^2 \left(\frac{1}{m_i \nu_{in}} + \frac{1}{m_e \nu_{en}} \right). \quad (3.11)$$

It is an easy matter to show that

$$\bar{\rho} \vec{v} = \bar{\sigma} \left(\frac{1}{c} \vec{v} \times \vec{B} \right), \quad (3.12)$$

and we finally obtain

$$\vec{j} = \bar{\sigma} \left(\vec{E} + \frac{1}{c} \vec{v} \times \vec{B} \right). \quad (3.13)$$

Thus, the tensor $\bar{\sigma}$ is the conductivity tensor, which relates the current density \vec{j} to an applied electric field measured in a reference frame moving with the bulk velocity of the neutral gas. The coefficient σ_P is called the Pedersen conductivity and represents the current in the direction along the electric field component perpendicular to the magnetic field; σ_H is the so called Hall conductivity, which gives the current in the direction perpendicular to both magnetic and electric fields; and finally, σ_0 is the tensor component representing the current parallel to the magnetic field direction (parallel conductivity).

3.2 Ionization due to Particle Precipitation

In an undisturbed, quiet ionosphere the primary source of atmosphere ionization is photoionization by the solar photons. However, under some conditions, i.e. during magnetic storms, precipitation of energetic particles becomes more important. The primary auroral particles are populations of electrons and ions with energies from < 100 eV up to small multiples of 100 keV. Some of these particles precipitate into the atmosphere, causing additional ionization.

Figure 3.1 schematically illustrates precipitation of auroral particles into the upper atmosphere. The dots in the figure show the higher-energy particles (> 20 keV), while the triangles represent the medium-energy particles ($\sim 0.5 - 20$ keV) producing the visual aurora. The stars show the lower-energy particles (< 1 keV) that penetrate into the ionosphere through the polar cusp and cause the dayside aurora. The particles from different energy bands have their sources in different regions of the magnetosphere. The most energetic particles lie on a circle of constant latitude and originate in the ring current. The medium-energy particles are accelerated downward along the earth's higher-latitude magnetic-field lines mostly from the magnetotail. The low-energy particles precipitate directly from the magnetosheath through the polar cusp with minimal acceleration.

Precipitating charged particles in the ionosphere are subject to inelastic and elastic collisions with the atmospheric constituents. They lose their energy gradually by

- ionizing and exciting atoms and molecules in the upper atmosphere,
- dissociating atmospheric molecules,
- heating the upper atmosphere, and
- producing bremsstrahlung x-rays.

A rigorous mathematical description of these processes can be found in [Rees, 1989]. Here we will reproduce plots of altitudinal dependence of ionization rates due to precipitating electrons (Fig. 3.2a) and ions (Fig. 3.2b) given in [Rees, 1989]. Thus, given the energies and fluxes of precipitating particles, the ion production rate can be established.

The produced ions and electrons are, in turn, lost in different recombination processes. The loss rate is generally given by

$$L = \alpha n_e n_i \tag{3.14}$$

where α is a recombination coefficient. This quantity is determined by experimental and theoretical methods and can be found in [e.g. Schunk and Nagy, 2000].

Once the ion production and loss rates are found, the altitude distribution of the ionospheric electron density, n_e , can be calculated. In the zeroth approximation (neglecting horizontal or vertical transport of plasma), one can assume

$$\frac{\partial n_e}{\partial t} = Q - L = 0, \tag{3.15}$$

where Q and L are the ion production and loss rates, respectively. Using, (3.14) and quasi-neutrality of plasma one obtains

$$Q = \alpha n_e^2, \quad (3.16)$$

and therefore

$$n_e = \sqrt{\frac{Q}{\alpha}}. \quad (3.17)$$

Equation (3.17) describes the electron density altitudinal profile, once the ion production rate due to precipitation is given. Utilizing (3.9), (3.10), and (3.11) one can now calculate the enhancement in the conductivities since they are proportional to n_e . Fig. 3.3 shows the altitudinal profiles of the electron density for the polar ionosphere used by *Barr and Stubbe* [1984]. The six electron density models represent the typical nighttime (models 1-3) and daytime (models 4-6) ionosphere under conditions of low, moderate, and high solar wind activity, respectively. The figure shows that at the altitude of 100 km the electron density variations from low to high solar wind activity can be up to an order of magnitude. This, however, results in a somewhat smaller increase in the ionospheric conductance due to integration over the height.

3.3 Turbulent Electron Heating

The other mechanism for the enhancement of the conductivity in the polar ionosphere results from the development of Farley-Buneman instability at the electrojet altitudes. This plasma instability (also known as the two-stream

instability) develops when there is a difference between the drift velocities of electrons and ions. Such situation occurs at the polar electrojet altitudes (100-120 km) where the electrons are magnetized ($\Omega_e \gg \nu_{en}$), while the ions are at least partially demagnetized ($\Omega_i \lesssim \nu_{in}$).

Below we briefly outline the most important results related to the mathematical formulation of the problem. Its detailed examination can be found in [Ossakow *et al.*, 1975; Kelley, 1989; Dimant and Milikh, 2003]. First, we notice that for sufficiently low frequency waves the electric field perturbations can be considered potential (electrostatic), i.e. $\delta\vec{E} = -\nabla\delta\Phi$, and therefore,

$$\delta\vec{E} = \begin{pmatrix} \vec{k} \\ k \end{pmatrix} \delta E. \quad (3.18)$$

Here \vec{k} is the wave vector, $k = |\vec{k}|$, and $\delta E = |\delta\vec{E}|$. Further, in the neutral wind frame (the frame where the neutrals are taken to be at rest) and in the same limit of low-frequency and wavelength waves, $\gamma_k \ll \omega_k \gtrsim kC_S \ll \nu_{in}$, the dispersion relation for the waves excited by the instability reads

$$\omega_k = \frac{\vec{k} [\vec{v}_e + \psi (1 + \chi_i^2) \vec{v}_i]}{1 + \psi (1 + \chi_i^2)} \quad (3.19)$$

$$\gamma_k = \psi \frac{(1 - \chi_i^2) (\omega_k - \vec{k} \cdot \vec{v}_i)^2 - k^2 C_S^2}{\nu_{in} [1 + \psi (1 + \chi_i^2)]} \quad (3.20)$$

Here

$$C_S = \sqrt{\frac{T_e + T_i}{m_i}} \quad (3.21)$$

is the isothermal local ion acoustic speed, $T_{e,i}$ are the temperatures of the electrons and ions, respectively. The quantities ω_k and γ_k represent the real and

imaginary parts of the wave frequency: $\omega(\vec{k}) = \omega_k - i\gamma_k$. Finally,

$$\psi = \psi_{\perp} \left(1 + \frac{k_{\parallel}^2 \Omega_e^2}{k_{\perp}^2 \nu_{en}} \right) \quad (3.22)$$

$$\psi_{\perp} = \frac{1}{(\varkappa_e \varkappa_i)} = \frac{\nu_{en} \nu_{in}}{\Omega_e \Omega_i} \quad (3.23)$$

where \varkappa_e and \varkappa_i are the electron and ion magnetization parameters,

$$\varkappa_e = \frac{\Omega_e}{\nu_{en}}, \quad \varkappa_i = \frac{\Omega_i}{\nu_{in}} \quad (3.24)$$

and k_{\parallel} and k_{\perp} are the parallel and perpendicular components of the wave vector with respect to the geomagnetic field, \vec{B}_0 . The drift velocities of strongly magnetized electrons and partially magnetized ions, \vec{v}_e and \vec{v}_i , are given by

$$\vec{v}_e = \frac{\vec{E}_C \times \vec{B}_0}{B_0^2} \quad \text{and} \quad (3.25)$$

$$\vec{v}_i = \frac{\frac{e\vec{E}_C}{m_i \nu_{in}} + \varkappa_i^2 \vec{v}_e}{1 + \varkappa_i^2}, \quad (3.26)$$

where \vec{E}_C is the ambient convective electric field.

The condition for the growth of the instability in linear theory, $\gamma_k \geq 0$, follows from (3.19) and (3.20). An analysis of (3.19) and (3.20) yields that the latter condition is achieved when the ambient convective electric field E_C exceeds a certain threshold. The level of the threshold depends on the direction of the wave propagation, but the value of the threshold is minimal when the wave propagates parallel to the relative electron-ion drift velocity: $\vec{k} \parallel \vec{v}_{rel} = \vec{v}_e - \vec{v}_i$, $k_{\parallel} = 0$. In this case the magnitude of the threshold electric field is given by

$$E_{th} = C_S B_0 \sqrt{\frac{1 - \varkappa_i^2}{1 + \varkappa_i^2}} [1 + \psi(1 + \varkappa_i^2)]. \quad (3.27)$$

In the limit $\nu_{in} \gg \Omega_i$, which is appropriate for most electrojet altitudes, and using $\vec{k} \perp \vec{B}_0$ (this follows from requirement of propagation parallel to the relative drift velocity) one finally obtains

$$E_{th} = C_S B_0 \sqrt{\frac{1 - \chi_i^2}{1 + \chi_i^2}} (1 + \psi_\perp). \quad (3.28)$$

Equation (3.28) is the center point of our discussion. For typical polar electrojet conditions, it yields about 20 mV/m, which can be easily reached in the disturbed ionosphere. The turbulent electric field developing due to the instability provides an additional source of energy for electrons and ions. The latter, though, are not significantly heated by the turbulent electric field at the electrojet altitudes. But the electron temperature can be substantially elevated over the initial temperature. It is important to note that the electrons are mainly heated by the small component of the turbulent electric field that is parallel to the ambient magnetic field. An assessment of the electron temperature can be made based on energy balance considerations [*Dimant and Milikh, 2003*]:

$$\frac{\Delta T_e}{T_0} = \frac{4\chi_i^2 \nu_{in}}{3\delta_{en} \nu_{en}} \frac{E_C^2}{E_{00}^2} \left\{ \left(\frac{1 + \psi_\perp}{1 + \chi_i^2} \right) \frac{(E_C - E_{th})^3}{E_C^2 E_{th}} + \psi_\perp \left[1 + \left(1 - \frac{E_{th}}{E_C} \right)^2 \right] \right\}. \quad (3.29)$$

In the above equation T_0 is the ambient neutral temperature, ΔT_e is the departure of the electron temperature from T_0 , E_{00} is given by

$$E_{00} = \sqrt{\frac{2T_0}{m_i}} B_0, \quad (3.30)$$

and all other terms are as defined above. The first term in the curly brackets on the right-hand side of (3.29) is responsible for the "parallel" heating (i.e. by the

parallel component of the turbulent electric field), while the second term represents the perpendicular heating. It is obvious that the first term dominates the second once the convective electric field exceeds the threshold value by a noticeable amount.

The question of the most interest for us is how the described effect of the turbulent electron heating may affect the ionospheric conductivities. Let us return to equation (3.9). At the electrojet altitudes the ion component of the Pedersen conductivity prevails over the electron component. The only direct effect of the elevated electron temperature on conductivity is through the electron-neutral collision rate, $\nu_{en}(T_e)$. But this quantity enters only the second term in (3.9) and thus does not contribute much to the overall value of the conductivity.

However, the turbulent electron heating can have an indirect influence on the conductivity through the changes in plasma density. According to (3.17), $n_e \propto \alpha^{-1/2}$ where α is the electron-ion recombination rate. The latter decreases with the electron temperature as T_0/T_e and therefore we obtain $\sigma_{P,H} \propto \sqrt{T_e/T_0}$. For strong electron heating of the order of 2000-3000 K, the maximum increase in $\sigma_{P,H}$ can reach a factor of 3. An illustration of how the electron temperature changes when the convective electric field exceeds the threshold value is shown in Fig. 3.4. This plot is based on the mathematical formulation given above and the detailed description of the model can be found in [Milikh and Dimant, 2003], a companion paper to [Dimant and Milikh, 2003]. To give the reader an impression

of the electric field values in the polar ionosphere we also include a color plot of the typical electric field distribution corresponding to storm-like conditions (Fig. 3.5). While the pronounced enhancements of the field close to the boundary on the dayside are numerical artifacts, the wide green spot in the center tipped toward the sun is the electric field distribution between the extrema of the electrostatic potential. The electric field in this area is about 100 mV/m which is about 5 times greater than the threshold electric field of the two-stream instability. Consulting Fig. 3.4 yields $T_e = 2500$ K at the altitude of 110 km which exceeds the ambient temperature by a factor of 5. According to the above estimates this is expected to result in $\sqrt{8} \sim 3$ times increase in the ionospheric conductivity. It should be mentioned, however, that the analysis of Fig. 3.4 yields a somewhat smaller increase in the ionospheric *conductance* due to a nonuniform altitudinal distribution of the electron temperature.

The importance of anomalous electron heating should be specifically emphasized in context of the present work. As discussed in subsequent chapters the transpolar potential saturates when the electric field in the solar wind exceed a threshold of ~ 5 mV/m and the level of saturation is lowered significantly when the ionospheric conductance is increased. On the other hand, the solar wind electric field of ~ 5 mV/m when mapped on the polar cap results in the electric fields that may readily exceed the Farley-Buneman threshold of ~ 20 mV/m leading to the enhancement of the ionospheric conductance. Thus, a high enough solar wind electric field affects the ionosphere via two channels: It tends to

enhance the transpolar potential through building up the reconnection potential, but, on the other hand, it increases the ionospheric conductance which tends to reduce the transpolar potential. We will return to this discussion in chapter 7.

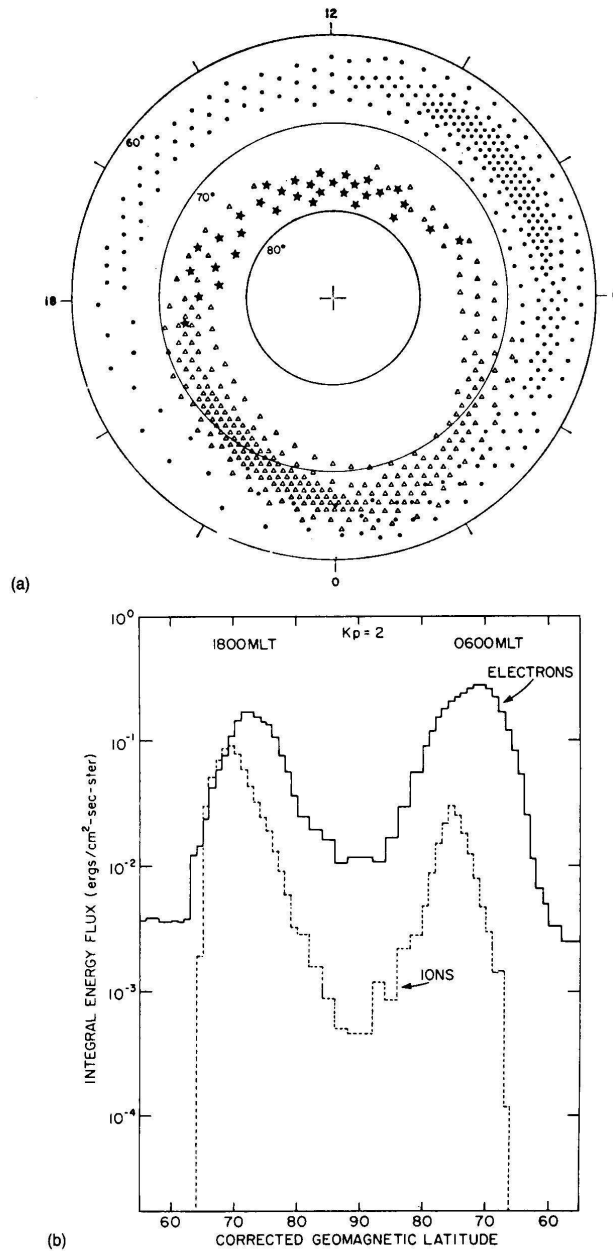


Figure 3.1: (a) Idealized representation of a three-zone auroral-particle precipitation pattern. The auroral-oval (medium-energy) precipitation is represented by the triangles, the auroral-zone (high-energy) by the dots, and the polar-cusp (low-energy) precipitation on the dayside by the stars. The average flux is indicated approximately by the density of the symbols. (b) Integrated energy flux into the auroral ionosphere across the dawn-dusk plane as a function of geomagnetic latitude for electrons and protons. (from [Kivelson and Russell, 1995])

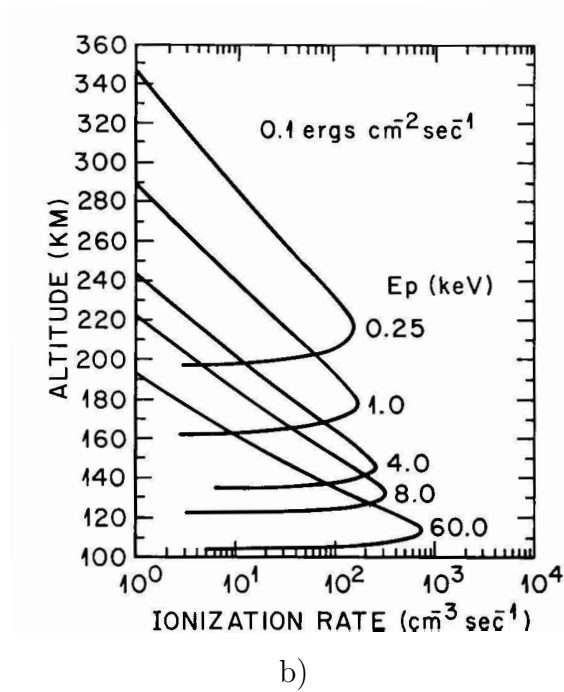
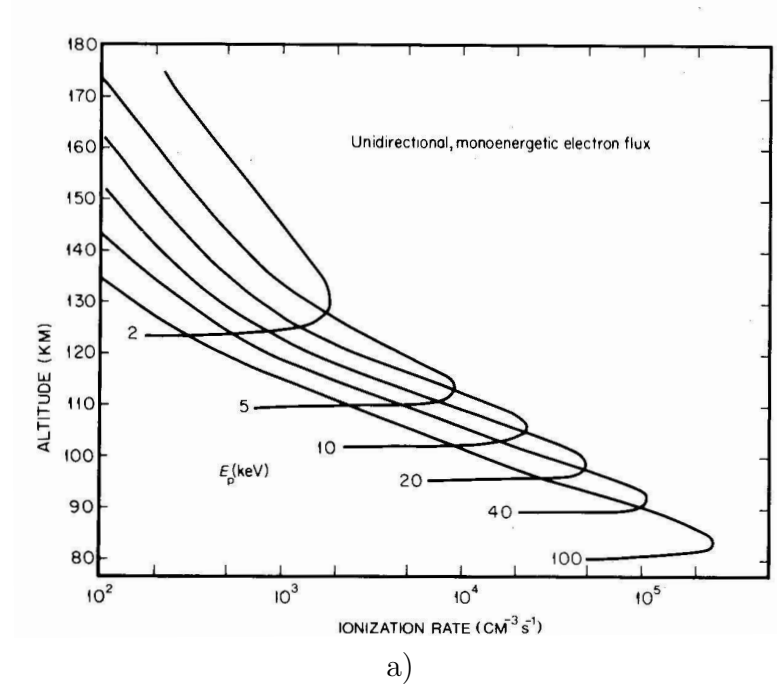


Figure 3.2: Altitudinal profiles of the ionization rate. a) due to a flux of 10^8 electrons/cm²s at several initial values of energy, E_p (keV), precipitating along magnetic field lines into the earth's atmosphere. b) due to proton fluxes with initial energy, E_p , identified on each curve. An isotropic flux over the upper hemisphere is assumed and the energy flux is 0.1 erg/cm²s at every initial proton energy. (from [Rees, 1989])

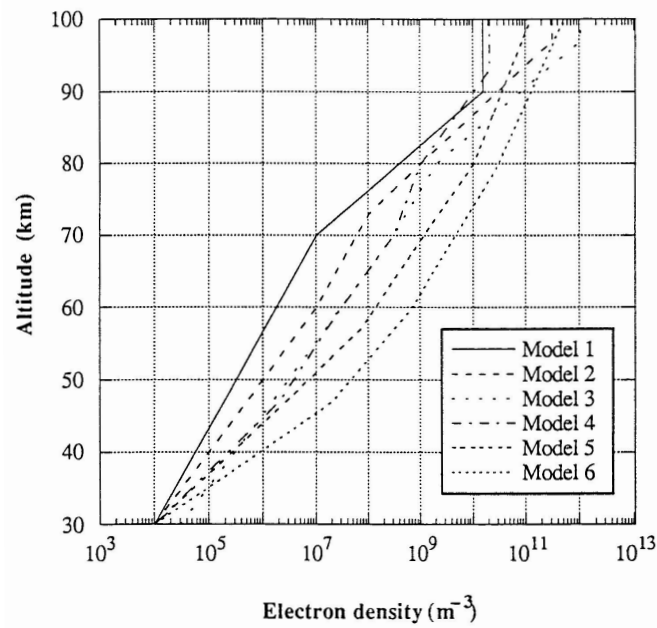


Figure 3.3: Electron density profiles from [Barr and Stubbe, 1984]

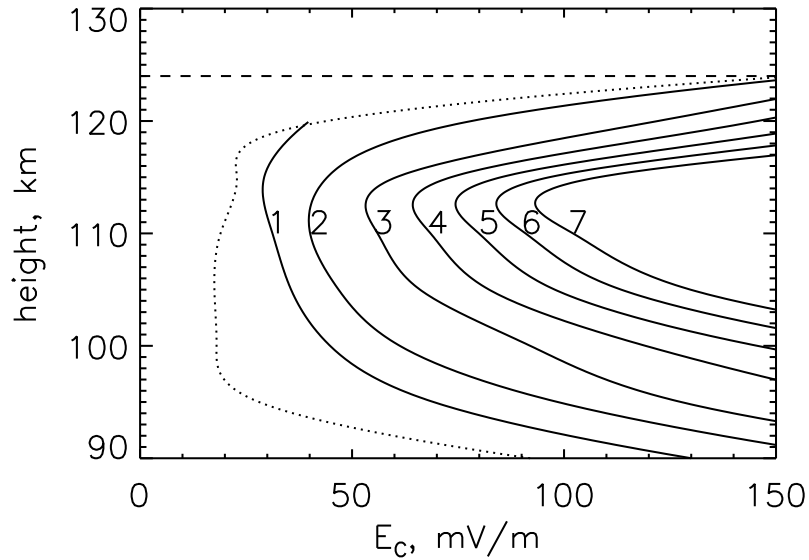


Figure 3.4: Isotherms of the electron temperature. The dotted trace shows the threshold of the Farley-Buneman instability, while the dashed trace shows the ion magnetization height. Numbers from 1 to 7 correspond to $T_e = 300, 500, 1000, 1500, 2000, 2500,$ and 3000 K, respectively. (from [Milikh and Dimant, 2003])

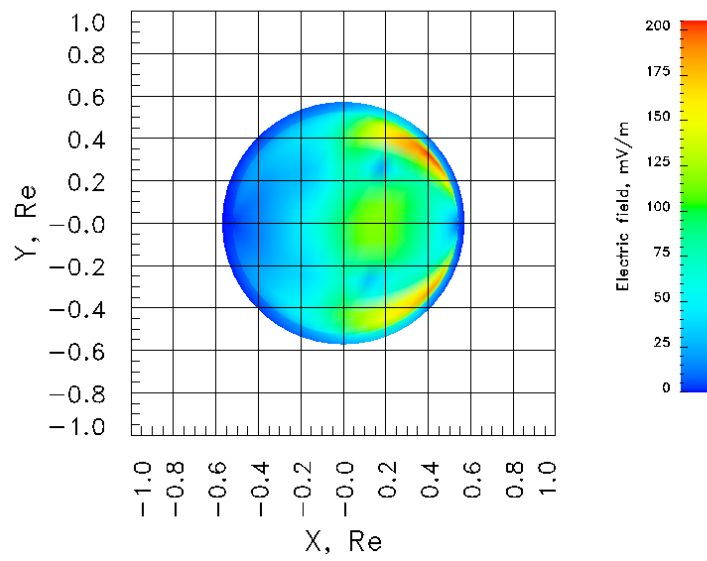


Figure 3.5: A typical distribution of the electric field in the polar ionosphere corresponding to storm-like conditions. The plot is based on global MHD simulations.

Chapter 4

The Cross Polar Cap Potential: Observational Evidence and Theoretical Models of Saturation

The classical model of the "open" magnetosphere first proposed by *Dungey* [1961] implies a two-cell convection pattern in the high-latitude ionosphere described in the Introduction and shown in Fig. 1.4. Experimentally observed convection patterns appear to be more complicated although they typically retain a basic two-cell structure [*Rich and Hairston*, 1994]. The cross polar cap potential is by definition the difference between the maximum and minimum electrostatic potential observed in the polar ionosphere. Since the ionospheric convection pattern is a "footprint" of the magnetospheric convection, the cross polar cap potential or the transpolar potential (henceforth we will occasionally use both terms or just Φ_{PC}) is a significant indicator of the interaction in the SW-M-I system.

Direct measurements of the transpolar potential usually can not be accomplished due to the complexity of the ionospheric convection pattern: the loci of the extrema of the electrostatic potential are not known *a priori* and in order to locate them the entire convection pattern should first be recovered.

However, based on a very large data set of measurements by the Defense Meteorological Satellite Program (DMSP) satellites, *Boyle et al.* [1997] were able

to directly survey the transpolar potential by considering only the orbits lying along the dawn-dusk meridian and assuming that the extrema of the potential are located close to this meridian. Most other observational techniques use satellite, radar, or ground based magnetometer measurements and then fit the result to some functional form to obtain the coverage for the entire polar cap.

The techniques that have been used to measure Φ_{PC} and to study its correlation with solar wind drivers include high-latitude, low-altitude spacecraft measurements of the convecting plasma velocity: OGO6 [Heppner, 1972], AE and S3 [Reiff *et al.*, 1981; Reiff and Luhmann, 1986; Doyle and Burke, 1983], and DMSP [Rich and Hairston, 1994; Boyle *et al.*, 1997; Burke *et al.*, 1999]; assimilation and mapping of ground based magnetometer and radar, and satellite measurements (e.g. Assimilative Mapping of Ionospheric Electrodynamics (AMIE)) [Richmond and Kamide, 1988]; linear regression relationships between solar wind parameters and ground-based magnetometer data such as the Institute of Terrestrial Magnetism, Ionosphere and Radiowave Propagation (IZMIRAN) Electrodynamic Model (IZMEM) [Papitashvili *et al.*, 1994], solar wind parameters and satellite data: DE2 [Weimer, 1995, 1996, 2001] and DMSP [Papitashvili *et al.*, 1999; Papitashvili and Rich, 2002]; and fitting backscattered ionospheric line-of site convection velocities from ground-based radars to functional forms of the electrostatic potential [Ruohoniemi and Baker, 1998; Shepherd *et al.*, 2002].

In this chapter we review some of these techniques with emphasis on the observational evidence for the saturation of the transpolar potential. In addition,

we address the seasonal dependence of Φ_{PC} and discuss theoretical arguments for its saturation.

4.1 Observations of the Cross Polar Cap Potential

It is natural to assume that the transpolar potential varies linearly with the solar wind convective electric field. Indeed, *Reiff and Luhmann* [1986] have speculated that for the southward IMF, 80-95% of the total cross polar cap voltage variation is due to the dayside magnetopause reconnection, while the contribution of the viscous processes and tail-lobe merging is typically less than 10 kV. In the ideal MHD model under steady state conditions the electrostatic potential is mapped from the dayside reconnection line to the polar cap. Since, the reconnection potential is proportional to the electric field in the magnetosheath, one expects a linear dependence of the transpolar potential on the solar wind electric field under assumption (not obvious, however) of a simple linear relation between the electric field in the magnetosheath and in the solar wind.

However, a number of observational studies have suggested that Φ_{PC} tends to saturate with increasing electric field in the solar wind. The effect is counterintuitive and hard to test experimentally, since the conditions under which it occurs are rather rare.

In the following four subsections we discuss different techniques to measure Φ_{PC} . The first of them is based on DMSP spacecraft electric field measurements and provides no evidence of Φ_{PC} saturation. The second one uses the electric

field instrument measurements of the DE2 satellite. The third and the fourth are based on the AMIE procedure and SuperDARN radar observations, respectively. The last three techniques confirm the effect of saturation.

4.1.1 Boyle Empirical Potentials

A number of functional forms have been suggested to represent the dependence of the transpolar potential on the solar wind parameters [*Boyle et al.*, 1997; *Reiff and Luhmann*, 1986]. In fact, *Vasyliunas et al.* [1982] have shown from dimensional analysis that any quantitative estimate of the transpolar potential should be of the form

$$\Phi_{PC} = vB_T l_{CF} Q(\theta, M_A^2) \quad (4.1)$$

where v is the solar wind bulk velocity, B_T is the projection of the IMF on the y - z plane, l_{CF} is the Chapman-Ferraro scale length given by $l_{CF}^6 = M_E^2 / \mu_0 \rho v^2$ with M_E being the earth's magnetic dipole moment and ρ being the mass density, and $Q(\theta, M_A^2)$ is a dimensionless function of two variables: θ , the clock angle, is defined by $\arccos(B_z/B_T)$ and M_A is the solar wind Alfvén-Mach number based on the transverse part of the field, $M_A^2 = \mu_0 \rho v^2 / B_T^2$. *Vasyliunas et al.* [1982] have argued that only two other dimensionless ratios can occur in the formula (4.1): $H = \mu_0 \Sigma_P v$, (where Σ_P is the Pedersen conductance), which measures the relative importance of ionospheric line tying compared to inertial effects, and $R = M_A (\sqrt{2}/\xi) e v B_T l_{CF} / m v^2$, the Reynolds number (where ξ is a dimensionless coefficient, m and e are the proton mass and charge), which

measures the relative importance of inertial vs. viscous effects. *Reiff and Luhmann* [1986] have suggested that each of these ratios may have second-order effects on the determination of the cross polar cap potential. However, in this dissertation we show that the dependence of the reconnection and transpolar potentials on the ionospheric conductance may be crucial for the Φ_{PC} saturation.

Boyle et al. [1997] have conducted a thorough survey of the cross polar cap potential measured by the DMSP F8 and F9 satellites. The polar cap potential database has been compiled using ~ 58000 polar passes with very stringent criteria of data selection. The orbit of the F8 satellite lies approximately along the dawn-dusk meridian, thus the determination of the total polar cap potential has been mainly based on F8's passes. Assuming $\vec{E} \times \vec{B}$ drifts, the measured flow data have been combined with a modeled local B field to determine the electric field along the spacecraft trajectory. The integrated electric field, with appropriate endpoints, gives the potential along the orbit track. However, the difference between the observed extrema $\Phi_+ - \Phi_-$ is generally less than the total cross polar cap potential drop, since the spacecraft generally observes only a portion of the convection pattern during each orbit. A detailed summary of the flow measurements by DMSP satellite instruments can be found in [*Rich and Hairston, 1994*].

In addition, hourly averaged IMP8 solar wind data were used, since the goal of the authors was to study the steady state behavior of the polar cap potential. The upstream plasma and magnetic field parameters were selected from periods

when the IMF was quasi-steady for several hours to ensure that only steady ionospheric patterns have been analyzed.

After applying stringent selection criteria to both DMSP and IMP8 data, the authors ended up with 127 steady passes along the dawn-dusk terminator. Using these data and a number of functional forms of the dependence of the transpolar potential on the solar wind parameters they reported as the best estimate

$$\Phi_{PC} = 10^{-4}v^2 + 11.7B \sin^3(\theta/2) \text{ kV}, \quad (4.2)$$

where v is the solar wind velocity in kilometers per second, B is the magnitude of the IMF in nanotesla, and θ is the clock angle. Fig. 4.1 shows a measured potential plotted against the estimate given by (4.2). It is noteworthy that *Boyle et al.* [1997] have mentioned that the formula predicts the polar cap potential drop for both skewed and unskewed convection very well. Skewed convection refers to situations when the IMF contains a considerable B_y component. Respectively, unskewed convection means that B_z component of the magnetic field dominates in the solar wind. The study showed no dependence on the IMF B_x component.

In order to examine a possible saturation effect in the dependence of the transpolar potential on the solar wind magnetic field, the authors augmented the initial dataset of 127 passes (which included only cases with solar wind $B < 7$ nT) by weakening the selection criteria and including solar wind data with $B > 7$ nT. The authors argued that if there is any saturation effect the observed

potentials would fall below the ones predicted by the model (4.2) for given solar wind conditions. Fig. 4.2 shows the ratio of the observed potentials to the unsaturated prediction given by (4.2) against the IMF magnitude. As the figure does not show a downward tilt the authors concluded that there is no indication of the saturation effect in the dataset used in this study.

It can be, however, argued that the potentials in this study are for the most part below 100 kV and the authors did not correlate them with the interplanetary electric field only with the magnetic field. In an earlier study *Reiff and Luhmann* [1986] based on the data from AE, DE, and S3-2 and S3-3 satellites correlated the cross polar cap potentials among others with the function of the form $\Phi_{PC} = \Phi_0 + vB \sin^n(\theta/2)$ and found a tendency of the corresponding dependence to saturate at high values of the solar wind driving function.

4.1.2 Weimer potentials

Burke et al. [1999] used the so called Weimer potentials [*Weimer*, 1995, 1996, 2001] to correlate the polar cap potential with the solar wind electric field in the Kan-Lee form [*Kan and Lee*, 1979]:

$$E_{K-L} = vB_T \sin^2(\theta/2), \quad (4.3)$$

where all variables are as defined above. The correlation was sought in the following form:

$$\Phi_{PC} = \Phi_0 + LE_{K-L}. \quad (4.4)$$

The Φ_0 term is usually interpreted as the part of the polar cap potential

explained by sources other than the interplanetary electric field (e.g. viscous interaction). The slope L has the physical meaning of the distance along which the upstream electric field should be integrated to yield the reconnection potential. In other words it is an "image" of the reconnection line in the solar wind upstream of the bow shock. We will return to this concept later on.

To obtain the values of Φ_{PC} this study used the same database and technique used by *Weimer* [1995, 1996]. Electric field measurements from the DE2 satellite were integrated to obtain potentials along orbital paths. They were compared with simultaneous measurements of the IMF and the solar wind velocity. The database contained measurements from 2879 polar cap passes with simultaneously available IMF. A small subset (25-50) of the passes representative of similar IMF/solar wind conditions was used to calculate electric potentials as functions of magnetic latitude and local time. Two-dimensional potential maps were obtained by fitting the data to a series of spherical harmonic coefficients. Φ_{PC} is, as usual, the algebraic difference between the maximum and minimum potentials.

The entire DE2 database was divided into four subsets on the basis of the magnitude of the IMF B_T with ~ 720 passes in each group. The sorting groups were $0 < B_T < 3.5$ nT, $3.5 < B_T < 5.2$ nT, $5.2 < B_T < 7.25$ nT, and $B_T > 7.25$ nT. For each of the four groups of measurements with similar B_T , data were fit

by least squares error to the functional form

$$\Phi_{PC} = \Phi_0 + L\bar{v}\bar{B}_T \sin^2(\bar{\theta}/2), \quad (4.5)$$

where the bars above the symbols represent ensemble averages of each quantity. The results of this fitting are summarized in Table 4.1. An interesting feature of the analysis seen in Table 4.1 is that the effective size L tends to decrease as the magnitude of the IMF B_T increases. This can be considered as a sign of the saturation of the dependence of the transpolar potential on the solar wind driving function. However, this tendency is clear only in the correlation with the IMF not with the solar wind electric field.

On the other hand, a plot showing the transpolar potentials observed by *Burke et al.* [1999] against the IEF for purely southward IMF demonstrates a clear saturation effect. *Russell et al.* [2001] reanalyzed the data of *Burke et al.* [1999] summarized in Table 1. They noticed that when plotting a Φ_{PC} dependence on the IEF it is plausible to subtract the residual potential Φ_0 resulting from northward IMF. This yields overall lower potentials than originally reported by *Burke et al.* [1999]. The result is shown in Fig. 4.3. The plot shows that the potential drop is linear with the applied IEF up to about 3 mV/m and very insensitive to it above this level. Strictly speaking, only one point in Fig. 4.3 falls out of the linear dependence. However, this point represents a large number of measurements, and thus Fig. 4.3 provides a solid evidence for the saturation effect.

We have discussed so far two studies based on very extensive satellite data sets. One of them does not indicate saturation while the other shows a tendency of Φ_{PC} to saturate as the IEF increases. It should be noticed that the effect may be difficult to test observationally because the conditions for which Φ_{PC} saturates rarely occur. In the following subsections we provide the results of more recent studies aimed specifically on the investigation of the saturation effect. One of them is based on the measurements of the transpolar potential given by the Assimilative Mapping of Ionospheric Electrodynamics (AMIE) procedure for five selected storms and the other is a comprehensive survey of the polar cap potentials observed by the SuperDARN radar array.

4.1.3 AMIE Polar Cap Potentials

AMIE is a technique for mapping high-latitude electric fields and currents and their associated magnetic variations from sets of localized observational data [Richmond and Kamide, 1988]. The specific feature of the technique is that many different types of measurements can potentially be used: electric fields from radars and satellites; electric currents from radars; magnetic perturbations on the ground and at satellite heights. The mathematical approach to this model is essentially very similar to Kalman filtering used in various engineering applications and meteorological data assimilation [e.g. Gershenfeld, 1999; Ghil and Malanotte-Rizzoli, 1991]. A brief formulation of the problem that AMIE attempts to solve is as follows: suppose there is a set of observations directly or

indirectly related to the ionospheric electric field and current patterns available for some time or set of times of interest. For example, there may be radar or satellite measurements of convection velocity at certain points (direct measurements) as well as magnetic variations on the ground or at a satellite (indirect measurements). In addition, certain information is available about interrelationships among the electrodynamic quantities, e.g., Ohm's law relating electric fields and currents. Furthermore, there is *a priori* information about the probable values of the electrodynamic features of interest, i.e., there may be a statistically averaged model along with some measure of variance from the average. The task then is to combine all of this information to come up with an optimized estimate of the electrodynamic features as well as an indication of the accuracy of the estimate. As was already mentioned this task is tackled using mathematical methods very similar to Kalman filtering.

Russell et al. [2001] used AMIE to study the effect of Φ_{PC} saturation during five selected storms: September 24-25, 1998; May 2-5, 1998; January 9-11, 1997; October 18-20, 1995; and October 18-20, 1998. In this study the data from ground based magnetometers, DMSP and NOAA satellites as well as SuperDARN radars were used as input to the AMIE procedure. DMSP spacecraft contributed particle data and ion drift measurements and NOAA satellites provided only electron energy flux and mean energy to calculate Pedersen and Hall conductances. The values of Φ_{PC} and the Joule dissipation in the polar cap were the outputs of the AMIE procedure.

The results of this study are summarized in Fig. 4.4. The plots show the values of Φ_{PC} and Joule heating versus the upstream solar wind electric field for the five storms. The saturation effect can be clearly seen on all plots although on the plots a) and b) the evidence for the saturation is much stronger since the IEF went to very high values during these two storms. However, for all five storms the transpolar potential shows a tendency to saturate after the IEF goes beyond about 3 mV/m and it never exceeds the threshold of 200 kV.

4.1.4 SuperDARN Polar Cap Potentials

The SuperDARN is an array of HF radars operating in both northern and southern hemispheres which cover a sizable fraction of the entire convection zone (approximately one-third) with time resolution of ~ 2 min [Ruohoniemi and Baker, 1998]. The radars measure the convection velocity by observing the drift of small-scale irregularities in the ionospheric F region. Backscattering occurs from HF rays that come in contact with the irregularities propagating orthogonally to the geomagnetic field lines. The Doppler shift in the backscattered signal provides an estimate of the line-of-sight component of the convection velocity. In the SuperDARN the radars are paired such that observations in common-volume areas are bidirectional and the two-dimensional $\vec{E} \times \vec{B}$ velocity can be resolved unambiguously.

To prevent nonphysical solutions in areas lacking measurements, data from a statistical model [Ruohoniemi and Greenwald, 1996] are added in these regions.

The radar data along with the statistical data are fitted into an expansion of spherical harmonic functions to recover the convection pattern over the polar cap. This technique is similar to the one used in [Weimer, 1995, 1996, 2001] and is referred to as APL FIT. Φ_{PC} is determined as usual as the difference between the extrema of the observed electrostatic potential.

Shepherd et al. [2002] applied APL FIT to investigate the relationship between the solar wind and the transpolar potential. Φ_{PC} was determined for 9464 10-min averaged periods between 1 February 1998 and 31 December 2000 when the solar wind was quasi-steady for no less than 40 minutes. The solar wind data were provided by the ACE spacecraft. The periods were chosen to minimize uncertainty in determining the geoeffective solar wind and interplanetary magnetic field conditions and to occur during times when APL FIT provided a suitable determination of Φ_{PC} .

Figures 4.5a- 4.5e show the convection pattern observed by SuperDARN for five sample 10-min periods. The small dots indicate the positions of the SuperDARN measurements. Contours are the equipotentials as determined by the APL FIT procedure spaced at 6-kV increments. During the periods shown backscatter from SuperDARN radars was observed over a large region of the dayside between ~ 0600 and 1800 MLT and, in some areas, from $< 65^\circ$ to nearly 90° latitude. There is also a large region of the post-midnight sector from which backscatter was observed.

As a solar wind driving function this study has used the Kan-Lee electric field

described in 4.1.2. The dependence of the observed cross polar cap potential on the solar wind electric field is shown in Fig. 4.6. Fig. 4.6a shows all 9464 10-min periods satisfying the quasi-stability condition imposed by the authors, while Fig. 4.6b contains only 1638 high-confidence periods with most reliable measurements of Φ_{PC} . A histogram on the right of each plot shows the distribution of Φ_{PC} values. Note that the Kan-Lee electric field units are kV/R_E which correspond to $\sim 0.16 \text{ mV/m}$. For each whole number of E_{KL} up to 40 kV/R_E , a sliding, linear least squares fit was performed to the data within a 10 kV/R_E window centered on that value. The resulting fit and corresponding $2\text{-}\sigma$ standard deviations are shown as dark line segments bounded by lighter line segments. For the data in the range $E_{KL} > 40 \text{ kV}/R_E$ a single fit was performed due to the sparsity of data at high values of E_{KL} .

Fig. 4.6 is the center point of the study. It clearly shows the effect of saturation when the solar wind electric field reaches about 20 kV/R_E or 3 mV/m in agreement with the results of *Russell et al.* [2001] described above. Due to the large number of measurements in the dataset this survey can be considered as a very strong evidence in favor of the cross polar cap potential saturation. It should be mentioned, however, that while the data from this study suggest that saturation of Φ_{PC} occurs, difficulties arise in using the APL FIT technique for large negative values of IMF (large southward magnetic field) and E_{KL} . The problem arises when extremely disturbed solar wind causes the polar cap to expand to magnetic latitudes equatorward of $\sim 55^\circ$. The SuperDARN radars in

the northern hemisphere are located between 56° and 65° magnetic latitude. Because of the propagation conditions necessary to achieve perpendicularity to the magnetic field at ionospheric altitudes and detect backscatter, the effective lowest magnetic latitude for observing backscatter tends to range from 58° to 63° , depending on the radar. This may result in a situation when the extrema of the cross polar cap potential lie beyond the boundary of the network observational field, and thus the APL FIT procedure tends to underestimate the value of Φ_{PC} for high IEF.

4.2 Seasonal Dependence of the Cross Polar Cap Potential

The seasonal dependence of the cross polar cap potential has been addressed in a number of studies dealing with polar convection patterns. In this section we give a brief overview of observational findings of some of these studies. It should be noted that seasonal dependence of the polar convection patterns is different for the two hemispheres. Summer in the northern hemisphere corresponds to winter in the southern one while during equinoxes we expect the two hemispheres to be equally affected by the geomagnetic activity. In what follows when we refer to a season we mean the season in the northern hemisphere.

The comprehensive study based on the dataset of DMSP spacecraft polar passes [Boyle *et al.*, 1997] was described in section 4.1.1. The average cross polar cap potentials for different seasons inferred from this dataset are summarized in Fig. 4.7. The standard deviations are shown by error bars and it can be seen in

the figure that they are much smaller than the differences between the averages for each season. Fig. 4.7 shows that the average potential is higher in winter than in summer and that there are pronounced maxima at the equinoxes.

An earlier survey of DMSP data [*Rich and Hairston, 1994*] based on essentially the same database yields somewhat different results. These authors binned the observed transpolar potential by both strength and clock angle of the IMF. For the range of the IMF strength $5 < B < 11$ nT they show the plots depicting average convection patterns for the northern hemisphere for eight values of the clock angle for each season (see Figs. 4-6 in [*Rich and Hairston, 1994*]). Averaging over the clock angle distribution yields an average value of the cross polar cap potential for equinox, summer and winter in the specified range of the IMF strength: 48, 44 and 48 kV with standard deviations 23, 20 and 21 kV, respectively. The fact that the standard deviations are almost half of the average in each case means that it is probably meaningless to average the potential over the IMF clock angle since the impact of the solar wind on the ionospheric convection varies drastically with the clock angle. Thus no conclusions can be drawn about the seasonal dependence of the transpolar potential from this analysis.

Due to the extremely large database used in [*Rich and Hairston, 1994*] we can infer the seasonal dependence of the potential by looking only at the cases with due southward IMF which is the most geoeffective situation. Using data from [*Rich and Hairston, 1994*] we plot in Fig. 4.8 the dependence of the average

cross polar cap potential on the IMF strength for each season and purely southward solar wind magnetic field. The solid line represents winter, the dotted line represents summer, and the dashed line represents equinox. Each line is based on three values of the average transpolar potential corresponding to the shown range of the IMF strength. Although the average winter potential shown in Fig. 4.8 is higher than the equinox and summer potentials (89 kV for winter, 87 kV for summer, and 83 kV for equinox) the standard deviations are still too big (32 kV, 26 kV, and 22 kV, respectively) to draw any general conclusions about the seasonal dependence. However, it should be mentioned that for high IMF values the cross polar cap potential shows a tendency to grow gradually from summer to winter as seen in Fig. 4.8.

The difference between this study and the results by *Boyle et al.* [1997] is probably due to different data selection criteria. In addition, in the latter model the potentials were averaged over all solar wind conditions (strength and direction of the IMF) while the shown results of the model by [*Rich and Hairston*, 1994] are based on the polar cap measurements corresponding to due southward IMF and three specified ranges of its strength.

We finally consider the study of the seasonal dependence of the cross polar cap potential in [*Papitashvili and Rich*, 2002]. They surveyed the average potentials observed by seven different polar convection models with the IMF strength $B_T = \sqrt{B_Y^2 + B_Z^2} = 5$ nT and structured the potentials by the IMF clock angle. We will use the results of only four models which have measurements

for summer, winter, and equinox: IZMEM is the Institute of Terrestrial Magnetism, Ionosphere and Radio Wave Propagation (Russian Academy of Sciences) electrodynamic model [Papitashvili *et al.*, 1994]; IZMEM/DMSP uses both the results of the IZMEM model and measurements from DMSP satellites [Papitashvili *et al.*, 1999]; DE2 is the model based on the potentials observed by DE2 spacecraft [Weimer, 1995]; and DICM is an extension of IZMEM/DMSP model [Papitashvili and Rich, 2002].

In Fig. 4.9 the average cross polar cap potentials produced by each of the four models are presented for southward IMF with strength $B_T = 5$ nT. Triangles show the average Φ_{PC} for equinox while diamond signs and squares correspond to summer and winter, respectively. The plot shows that there is no agreement between the models on the seasonal dependence of the transpolar potential. IZMEM/DMSP model and DICM model which is an extension of the former yield higher potential for winter than for summer while the equinox value is almost indistinguishable from the summer value. On the other hand, the IZMEM model and Weimer model (denoted as DE2) do not reveal any difference between summer and winter potentials while the equinox values are somewhat higher.

In summary, four of six models discussed yield higher winter average cross polar cap potential than summer potential. There is no agreement between models concerning the equinox potential. It should be mentioned, however, that all models are based on different datasets. Fig. 4.7 shows Boyle *et al.* [1997] potentials without structuring them by the strength or clock angle of the IMF.

The model *Rich and Hairston* [1994] uses basically the same dataset but the cross polar cap potential shown in Fig. 4.8 is taken for the cases with purely southward solar wind magnetic field. Finally, the results of the models from the study of *Papitashvili and Rich* [2002] shown in Fig. 4.9 correspond to the solar wind $B_z = -5$ nT.

The seasonal dependence of the cross polar cap potential is very relevant to the issue of its saturation. As we show in this dissertation the level of saturation depends strongly on the ionospheric conductance which grows by 30-40% from winter to summer. This suggests that the saturated potential may have a seasonal dependence as well. Unfortunately, there is no database existing so far that contains only saturated cross polar cap potentials. This is mostly due to the fact that conditions for which saturation is observed rarely occur as was mentioned earlier. In addition, it should be mentioned that during periods of extremely disturbed solar wind conditions, precipitating energetic particles from the solar wind cause a growth of the ionospheric conductance which may exceed seasonal variations greatly (see Chapter 3). Therefore, a possible seasonal dependence of the saturated cross polar cap potential is not obvious and requires future statistical studies.

4.3 The Hill/Siscoe model of the cross polar cap potential saturation

4.3.1 Formulation

Having reviewed the observational evidence for the saturation of the transpolar potential we turn to the discussion of theoretical grounds for the existence of this effect. The only theoretical model existing so far that predicts the effect of the saturation is the so called Hill model. *Hill et al.* [1976] and *Hill* [1984] have argued that there is a natural limit on the value of the convection potential in the polar cap. The limit is set by the convection potential that drives ionospheric currents and associated region 1 currents between the magnetopause and ionosphere sufficiently large to cause major alterations (the amount of major alteration is defined later) in the magnetic field near the dayside magnetopause. The limiting potential is then approximately given by

$$\Phi_i \equiv R_M B_d / (\mu_0 \Sigma_P), \quad (4.6)$$

where R_M is the radius of the magnetosphere, B_d is the magnetic field just inside the magnetopause due to the earth's dipole, Σ_P is the ionospheric Pedersen conductance, and we have kept the original notation of *Hill et al.* [1976]. On the other hand, there is an upper limit on the magnetic reconnection speed which is set by the local Alfvén speed, v_A . The maximal reconnection potential is then determined as

$$\Phi_M \equiv v_A B_M R_M, \quad (4.7)$$

where B_M is the magnetic field in the magnetosheath. In general, the cross polar cap potential, Φ_{PC} , is given by Φ_i or Φ_M , whichever is smaller, and one can write

$$\Phi_{PC} \lesssim \frac{\Phi_i \Phi_M}{\Phi_i + \Phi_M} = \frac{\Phi_M}{1 + \Sigma_P / \Sigma_0}, \quad (4.8)$$

where

$$\Sigma_0 \equiv \frac{B_d}{\mu_0 B_M v_A}. \quad (4.9)$$

Recently, *Siscoe et al.* [2002b] have reported a model of the transpolar potential saturation based on the Hill model. This model (we will refer to it as the Hill/Siscoe model) incorporates the saturation effect "by construction". It is formulated in the following manner. As in the Hill model, the limit on the transpolar cap potential is set by the potential that drives region 1 currents sufficiently large to significantly influence the dipole magnetic field at the nose of the magnetopause. It is then postulated that for a weak solar wind driver the cross polar cap potential is equal to the reconnection potential Φ_M , while for large driver Φ_{PC} is equal to the saturated potential Φ_S :

$$\Phi_{PC} = \frac{\Phi_S \Phi_M}{\Phi_S + \Phi_M}. \quad (4.10)$$

This formulation is similar to (4.6)–(4.9) where the notation is changed so that Φ_i is substituted by Φ_S . However, an essential difference between the original Hill model and the interpretation of *Siscoe et al.* [2002b] is that the former does not allow the transpolar potential to differ from the reconnection potential. It just postulates that Φ_{PC} is always smaller than the *upper* limit on the reconnection

potential, while the Hill/Siscoe model requires that the saturated transpolar potential $\Phi_{PC} = \Phi_S$ be smaller than the reconnection potential Φ_M . We shall return to this discussion later on.

The relation between Φ_{PC} and the magnitude of the region 1 currents is the ionospheric Ohm's law:

$$I = \xi \Sigma_P \Phi_{PC}, \quad (4.11)$$

where Σ_P is the ionospheric Pedersen conductance and ξ is a coefficient depending on the geometry of currents flowing in the ionosphere. Its value is between 3 and 4, which is supported by various MHD simulations [*Siscoe et al.*, 2002b, and this dissertation as shown below]. Equation (4.11) is expected to hold in particular for the saturated region 1 current I_S . Thus, combining (4.10) and (4.11) one obtains

$$\Phi_{PC} = \Phi_M - (\Phi_M/I_S) I. \quad (4.12)$$

The quantity Φ_M/I_S represents the effective internal resistance of the generator. An important difference between the Hill and Hill/Siscoe models is in the way the quantities Φ_M , Φ_S , and I_S are determined. In the Hill/Siscoe model the expression for the reconnection potential at the magnetopause, Φ_M , is based on the general relation (4.1):

$$\Phi_M = \chi L_r E_{sw} p_{sw}^{-1/6} F(\theta), \quad (4.13)$$

where L_r is the magnetopause reconnection line length in units of the earth's radii, E_{sw} is the convective solar wind electric field in mV/m, p_{sw} is the solar

wind ram pressure in nPa, and $F(\theta)$ is some function of the IMF clock angle such that $F(\pi) = 1$ and $F(0) = 0$. The coefficient χ quantifies the effects of magnetosheath compression and reconnection efficiency:

$$\chi = 4f_r (2\kappa\rho_{sw}/\rho_{sh})^{1/2}, \quad (4.14)$$

where f_r is the reconnection efficiency factor (ratio of reconnection velocity to Alfven velocity) and ρ_{sh} and ρ_{sw} are the mass densities in the magnetosheath and solar wind, respectively. The coefficient κ is the ratio of the stagnation pressure to the dynamic pressure upstream of the bow shock. Its magnitude can be analytically determined considering a hydrodynamical flow [*Landau and Lifshitz, 1959*]:

$$\kappa = \frac{1}{\gamma} \left(\frac{\gamma + 1}{2} \right)^{\frac{\gamma+1}{\gamma-1}} \left(\gamma - \frac{\gamma - 1}{2M^2} \right)^{-\frac{1}{\gamma-1}}, \quad (4.15)$$

where γ is the ratio of specific heats and M is the flow Mach number upstream of the bow shock. It is easy to see that the coefficient κ is of order unity and very rapidly tends to the asymptotic value of 0.88 with increasing Mach number. The hydrodynamic result for the ratio of the mass densities reads [*Landau and Lifshitz, 1959*]

$$\rho_{sw}/\rho_{sh} = \frac{(\gamma - 1)M^2 + 2}{(\gamma + 1)M^2}. \quad (4.16)$$

Let us now estimate the magnitudes of the terms in (4.13). Values taken for f_r and L_r by *Siscoe et al. [2002b]* are 0.1 and 30 R_E , respectively, so that their product yields ~ 3.0 . *Siscoe et al. [2002b]* estimate the density ratio (4.16) for magnetosonic Mach number equal to 3.74 but the result is insensitive to M over

a wide range of values. Combining all the terms, (4.13) can be evaluated:

$$\Phi_M(\text{kV}) = 57.6 E_{sw}(\text{mV/m}) p_{sw}(\text{nPa})^{-1/6} F(\theta). \quad (4.17)$$

To obtain an expression for the region 1 current causing sufficient changes in the dipole magnetic field at the magnetopause subsolar point, I_S , *Siscoe et al.* [2002b] use an idealized geometrical model. The region 1 current is modeled via two circular loops that form a figure eight in the terminator plane. Such current system generates a southward magnetic field at the magnetopause subsolar point, which strength is given by

$$B_{r1} = G(x_s, r) \frac{\mu_0 I}{R_E} p_{sw}^{1/6}, \quad (4.18)$$

where the denominator of the ratio in the equation represents the ram pressure scaling of the magnetopause subsolar distance x_s (the Chapman-Ferraro scaling). The distances x_s and r are numerical estimates of the above distance and the radius of the loop expressed in the earth's radii. *Siscoe et al.* [2002b] adopt $x_s = 10$ and $x_s/r = 3/4$. Then, numerically, $G(x_s, r) = 0.014$. Evaluation of terms in (4.18) yields

$$B_{r1}(\text{nT}) = 2.8 I(\text{MA}) p_{sw}^{1/6}. \quad (4.19)$$

The idea behind the Hill/Siscoe model is that when $I = I_S$ the above magnetic field is a significant fraction of the dipole magnetic field at the stagnation point. *Siscoe et al.* [2002b] define "significant fraction" as about 1/2. Finally,

$$I_S(\text{MA}) = 4.6 p_{sw}(\text{nPa})^{1/3} \quad (4.20)$$

where the change in pressure scaling results from the dipole field strength at the stagnation point scaling as $p_{sw}^{1/2}$. Putting all terms together gives the expression for Φ_{PC} :

$$\Phi_{PC}(\text{kV}) = \frac{57.6 E_{sw} p_{sw}^{1/3} F(\theta)}{p_{sw}^{1/2} + 0.0125 \xi \Sigma_P E_{sw} F(\theta)}, \quad (4.21)$$

where E_{sw} is in mV/m and the Pedersen conductance Σ_P is in mho.

4.3.2 Comparison with observations

Since the Hill/Siscoe model is the only quantitative model of the transpolar potential saturation it is very important that it predict the saturated potential at observed levels. Several attempts have been made to test the model against observations.

The original article by *Siscoe et al.* [2002b] provides a comparison of the cross polar cap potential drop dependence on the solar wind convective electric field for 24, 25 September 1998 geomagnetic storm as observed by *Russell et al.* [2000] and the Hill/Siscoe model (see Fig. 4.10). The figure reveals a good resemblance of the model with data. It should, however, be mentioned that the dynamical pressure and the conductance are used practically as free parameters in the Hill/Siscoe model in the above comparison. The modeled saturated potential depends strongly on both of these quantities and the functional form of (4.21) is such that with proper adjusting of the parameters any saturation-like dependence can be fitted with this function. For instance, for $p_{sw} = 5$ nPa, which is consistent with the main phase of the storm [*Russell et al.*, 2000], the modeled

saturated potential is about 250 kV, i.e. about 50 kV higher than the highest cross polar cap potential seen in the data (Fig. 4.10). For $p_{sw} = 10$ nPa the model yields 310 kV.

Hairston et al. [2003] have done a comparison of the Hill/Siscoe model with the cross polar cap potentials observed by DMSF F13 satellite during 31 March 2001 geomagnetic storm. In Fig. 4.11 the potentials measured by the spacecraft during six polar passes are shown along with the predictions of Boyle model (see 4.1.1) and full magnetospheric potential given by (4.17). Once again we see a good correlation between the transpolar potential predicted by the Hill/Siscoe model and the observations. However, it should again be mentioned that Fig. 4.11 demonstrates that the proper choice of the dynamical pressure and ionospheric conductance are crucial in the model.

Shepherd et al. [2003] have tested the Hill/Siscoe model against the potentials measured by the SuperDARN radar array. Their results suggest that the best fit of the Hill/Siscoe potentials to the observed ones is obtained when the ionospheric conductance $\Sigma_P = 23$ mhos and a constant potential $\Phi_0 = 17$ kV is added. In Fig. 4.12 the comparison of the SuperDARN data with the model is shown. In addition, for comparison, the results of the Hill/Siscoe model for two extremal values of ionospheric conductance $\Sigma_P = 2$ and 44 mhos, and the Boyle potentials are shown. While the figure demonstrates that some aspects of the data agree very well with the model, including the mean value and the saturation effect, the value of the ionospheric conductance used to obtain the fit is too high

(usually used values are $\lesssim 10$ mhos). However, there is a problem with SuperDARN measurements of the cross polar cap potential discussed earlier (see section 4.1.4). SuperDARN data tend to underestimate Φ_{PC} for big storms which can lead to an increase in the effective conductance used in the Hill/Siscoe model to obtain the best fit to the data.

It should also be noticed that the dynamical pressure dependence of the saturated potential predicted by the Hill/Siscoe model is inconsistent with observations of SuperDARN. The latter reveal no dependence on the dynamical pressure while the model suggests $\sim p^{1/3}$ scaling.

4.4 Discussion

The effect of the transpolar potential saturation has become well known by now. Because of its importance for space weather and the geospace environment, it has gained a growing interest recently. A number of observational techniques reviewed above confirm the existence of the effect. They include satellite and radar measurements of the convection in the ionosphere as well as the data from ground based magnetometers. On the other hand, there have been suggested theoretical arguments that provide analytical grounds for the explanation of the effect [*Hill et al.*, 1976; *Hill*, 1984; *Siscoe et al.*, 2002b,a]. The Hill/Siscoe model provides a functional form of the transpolar potential dependence on the solar wind parameters including the IEF and the solar wind ram pressure and ionospheric conductance.

Equation (4.21) is the basic point of the Hill/Siscoe model. An important feature of this relation is that it does not imply any dependence of the reconnection potential on the ionospheric conductance. The reconnection potential is given by the numerator of the formula divided by the first term of the denominator. The second term of the denominator, which includes the dependence on the conductance, epitomizes the feedback from the region 1 current and results in the saturation effect.

Let us turn to equation (4.10) underlying the Hill/Siscoe model. It assumes that the direct mapping of the reconnection potential onto the ionospheric polar cap occurs only when the reconnection potential Φ_M is small enough. For a stronger solar wind driver the direct mapping is prevented due to unspecified physical mechanisms. The conditions that ensure the mapping of the electrostatic potential include infinitely conducting magnetic field lines (ideal MHD) and quasi-steadiness of the driver. The difference between the magnetospheric (reconnection) potential and the cross polar cap potential arising from (4.21) can be as large as several hundred kilovolts (Fig. 4.11: the difference between the Φ_M line and $\Sigma_P = 10$ line, for example). The observed parallel potential drops in the inner magnetosphere are rarely reported to be higher than ~ 30 kV. Thus, the difference between the reconnection potential and Φ_{PC} resulting from parallel potential drops can be estimated at about 60 kV at the most. The time-variation effects are usually considered small, taking into account that most observational techniques average the cross polar cap potential over several tens of minutes.

Therefore, inconsistency between the reconnection potential and Φ_{PC} seen in (4.21) cannot be explained in terms of parallel potentials or time varying conditions. The Hill/Siscoe model does not discuss this breakdown of ideal MHD model. Instead, it incorporates the saturation effect in an *ad hoc* manner.

However, besides its analytical formulation, the Hill/Siscoe model emphasizes an important effect of the ionospheric feedback on the solar wind-magnetosphere-ionosphere coupling. The feedback results from the region 1 current significantly weakening the dipole magnetic field at the magnetopause subsolar point. In addition to this effect, *Siscoe et al.* [2002a] reported another mechanism for the saturation of the cross polar cap potential. It is based on a paradigm of a previously unrecognized storm-time magnetosphere in which the region 1 current rather than the Chapman-Ferraro current is dominant on the dayside magnetopause. In this model it is the region 1 current that balances the solar wind ram pressure and thus it cannot exceed the level required to resist the solar wind.

These ideas provide a broad framework for a future work. The discrepancy between the transpolar and the reconnection potential pertaining to the Hill/Siscoe model suggests that the influence of the ionospheric conductance on the reconnection potential should be studied. The necessity to tune the dynamic pressure and the ionospheric conductance terms in the Hill/Siscoe model to make it fit to data suggests that the feedback of the ionospheric conductance is not limited to the effects discussed. There exists probably another mechanism by

which the ionosphere can regulate the coupling between the solar wind and the magnetosphere-ionosphere system. In the next two chapters we present the results of global MHD simulations whose objective is to resolve these issues.

Table 4.1: Correlation fit to (4.5). R stands for the correlation coefficient. (from [Burke et al., 1999])

B_T , nT	\bar{v} , km/s	Φ_0 , kV	L , R_E	R
2.3	458.	31.24	4.62	0.958
4.3	448.	24.55	4.55	0.982
6.1	456.	22.40	4.38	0.991
10.4	465.	31.94	2.94	0.990

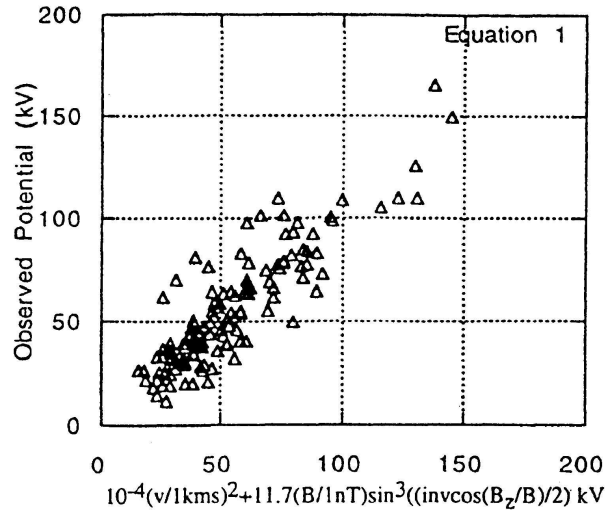


Figure 4.1: Relationship between the observed potential and the predictions of equation (4.2). This fit and the plot use 127 cleanest passes with 4 hours of steady IMF which occurred near the terminator. (from [Boyle et al., 1997])

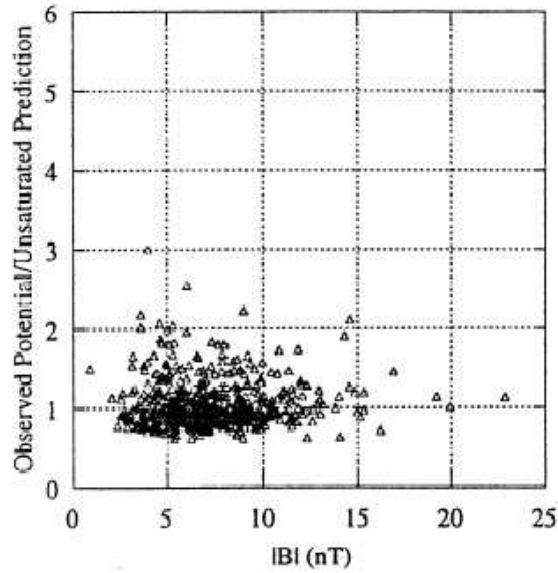


Figure 4.2: Observed cross polar cap potentials normalized by the unsaturated value predicted by the model (4.2) versus a single hour average IMF with requirement of 2 hours steady IMF. (from [Boyle *et al.*, 1997])

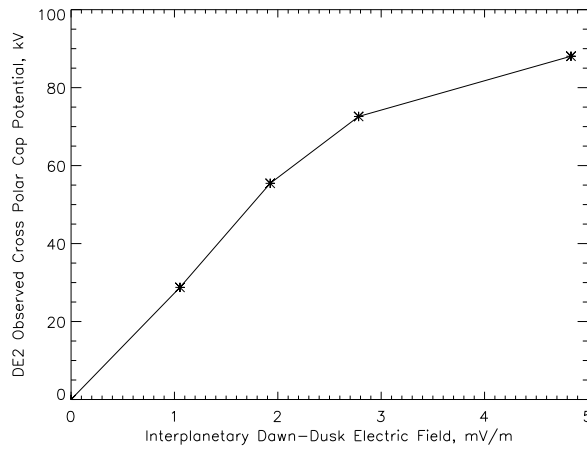


Figure 4.3: Potential drop plotted versus the corresponding value of the IEF for due southward IMF from the measurements by *Burke et al.* [1999] (after [Russell *et al.*, 2001])

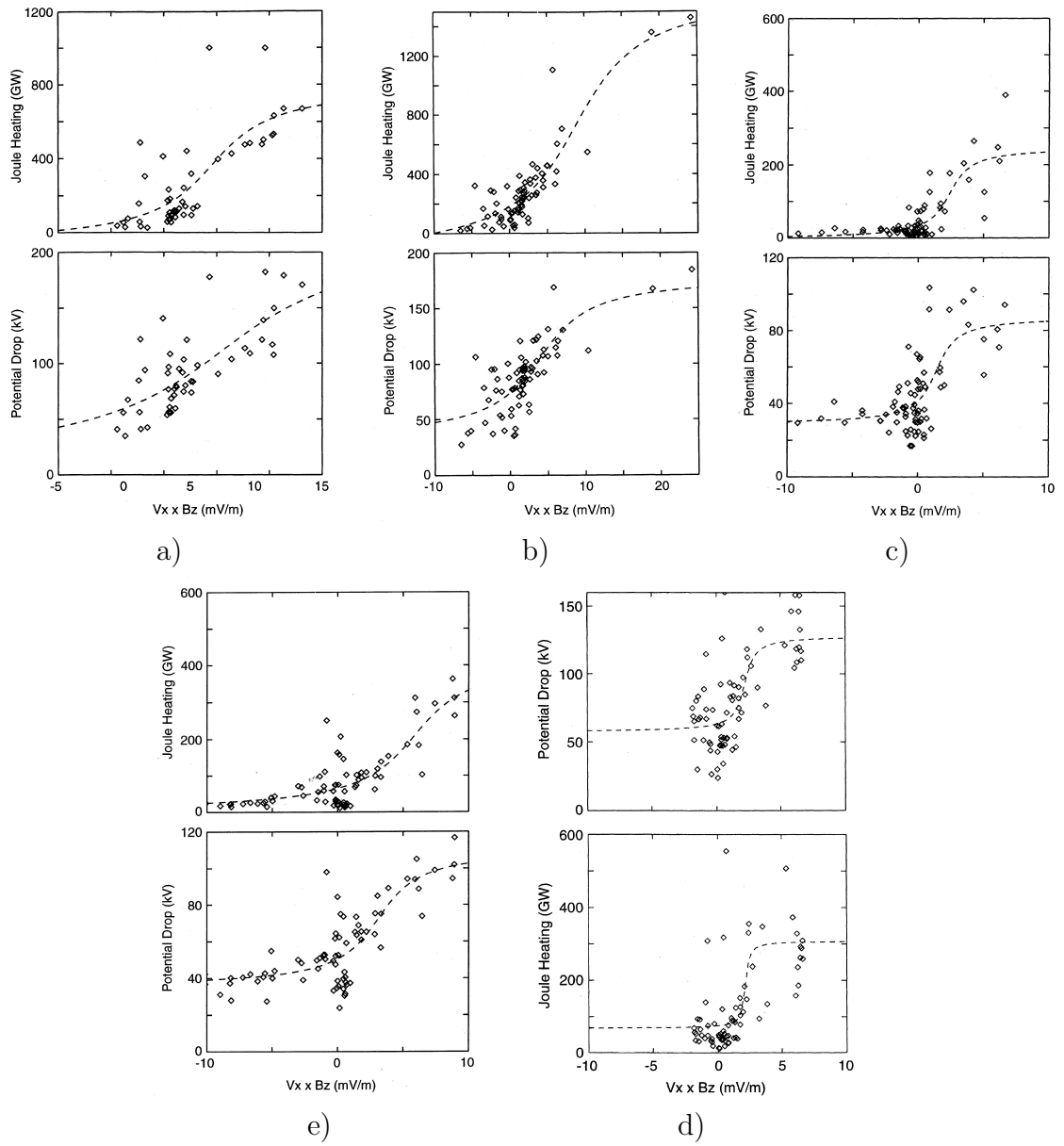


Figure 4.4: One hour averages of the cross polar cap potential and the Joule heating versus the IEF with arctan fit during a) September 24-25, 1998 storm; b) May 2-4, 1998 storm; c) January 9-11, 1997 storm; d) October 18-20, 1995 storm; e) October 18-20, 1998 storm (from [Russell et al., 2001])

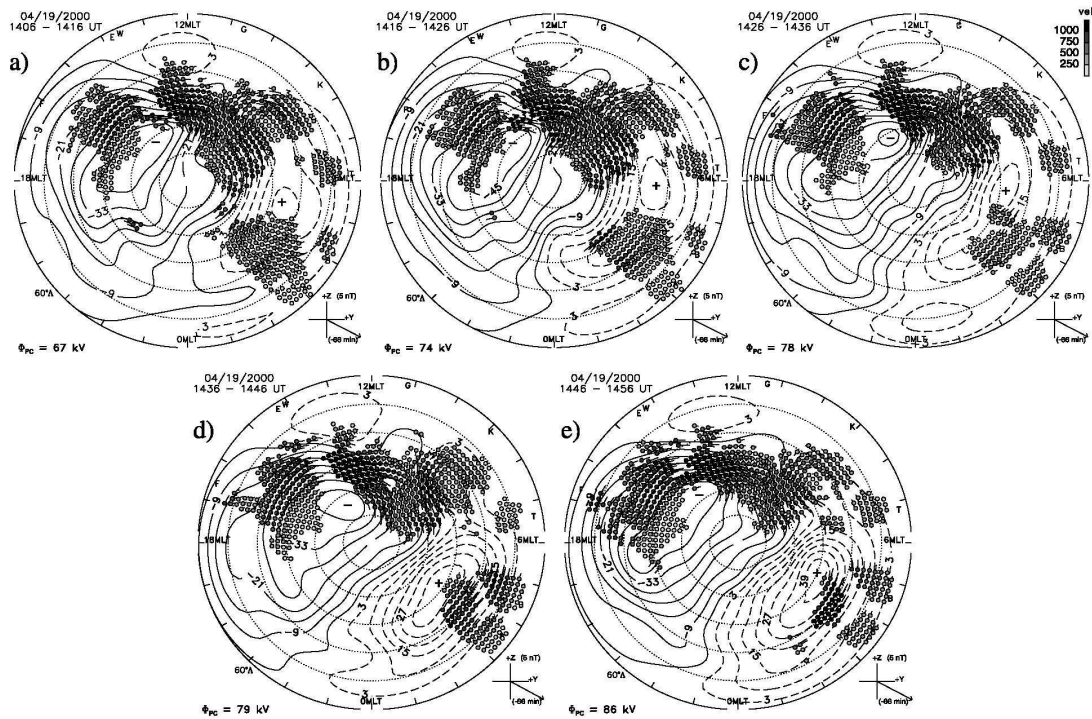


Figure 4.5: Solutions of the electrostatic potential using APL FIT for the shown 10-min periods. The small dots indicate the positions of the SuperDARN measurements. Contours are the equipotentials as determined by the APL FIT procedure spaced at 6-kV increments. (from [Shepherd *et al.*, 2002])

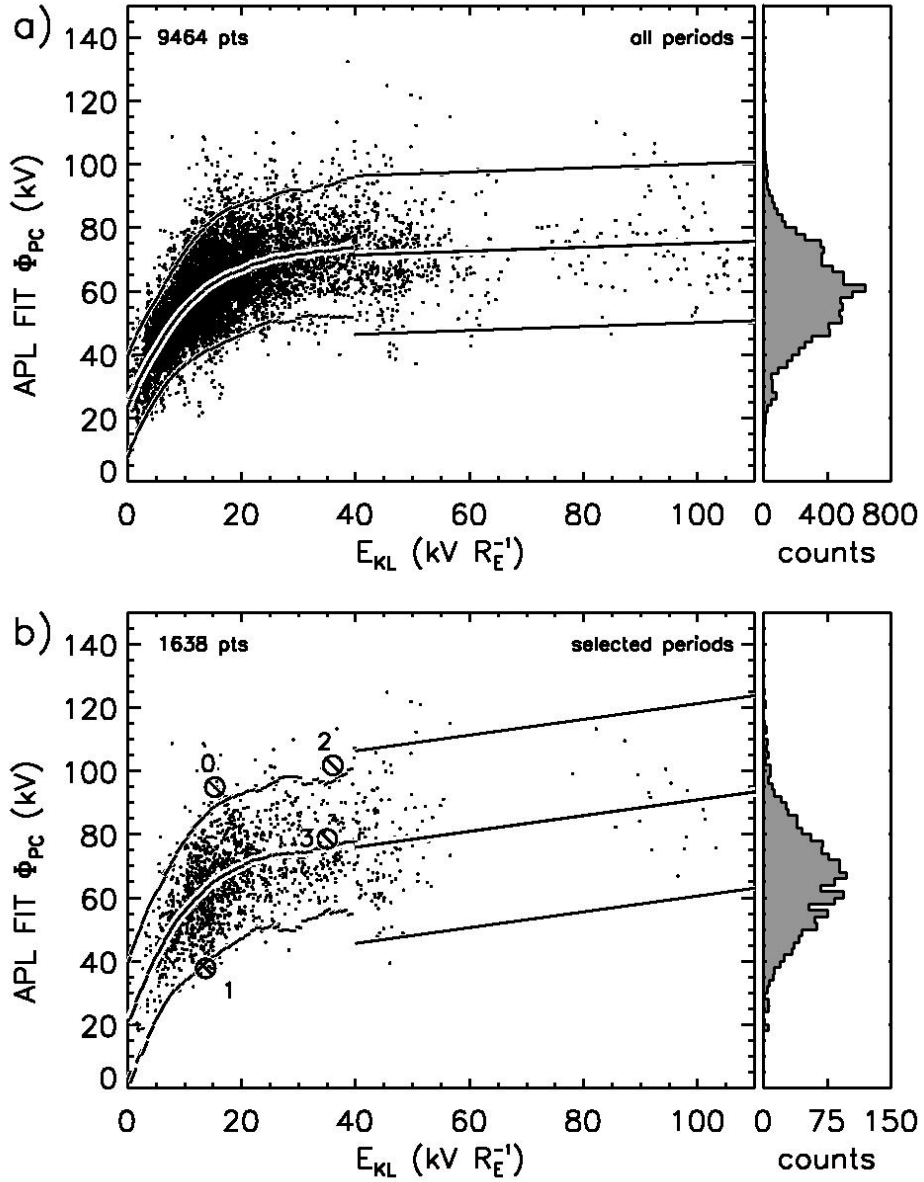


Figure 4.6: Φ_{PC} as a function of E_{KL} as determined using APL FIT for a) all 10-min periods satisfying the quasi-stability condition and b) those periods where the SuperDARN data sufficiently determine Φ_{PC} . Each 10-min period is represented by a dot. A sliding, linear least squares fit to data within a 10 kV/R_E window, and corresponding $2\text{-}\sigma$ deviations, are shown for each unit of E_{KL} up to 40 kV/R_E . Due to the sparsity of data in the range $E_{KL} > 40 \text{ kV/R}_E$, a single fit was performed on these data. (from [Shepherd et al., 2002])

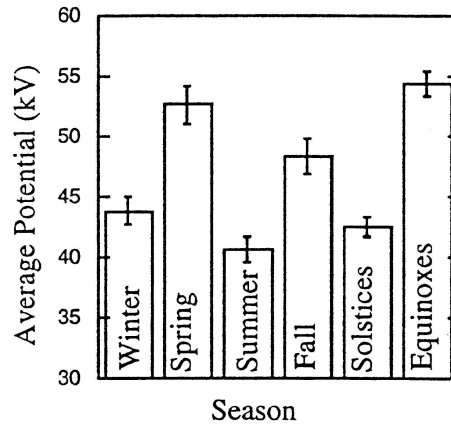


Figure 4.7: Average cross polar cap potentials by seasons for the northern hemisphere inferred from DMSP satellite polar passes. (from [Boyle *et al.*, 1997])

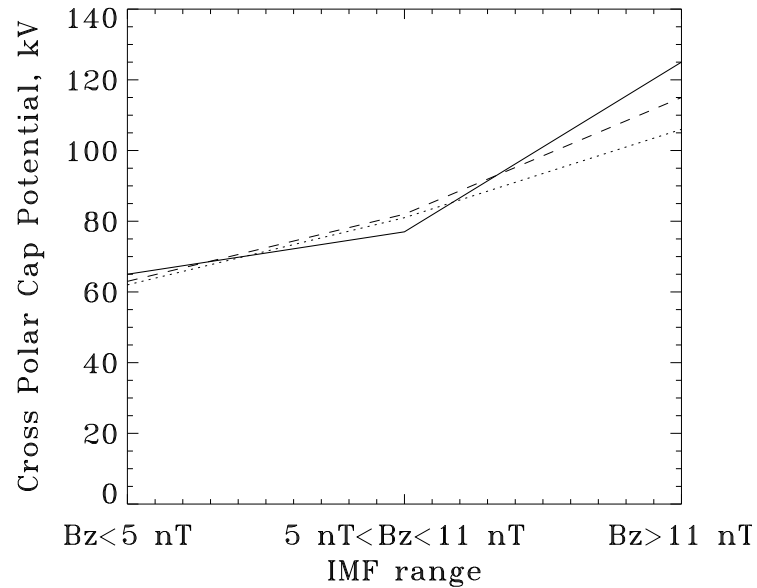


Figure 4.8: The dependence of the average cross polar cap potential on the IMF strength range for due southward IMF. The solid line corresponds to winter, the dotted line is for summer, and the dashed line is for equinox. The figure is based on the data from DMSP satellites during the period September 1987 to December 1990 as presented by Rich and Hairston [1994].

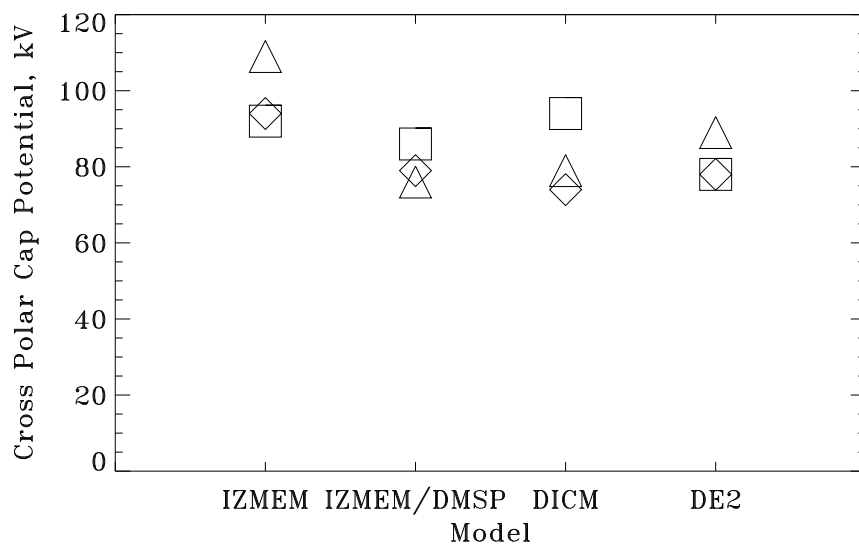


Figure 4.9: The transpolar potential given by the four shown models of polar convection for each season. The IMF conditions correspond to $B_T = 5$ nT and due southward magnetic field. Triangles correspond to equinox, diamond signs correspond to summer, and squares are for winter.

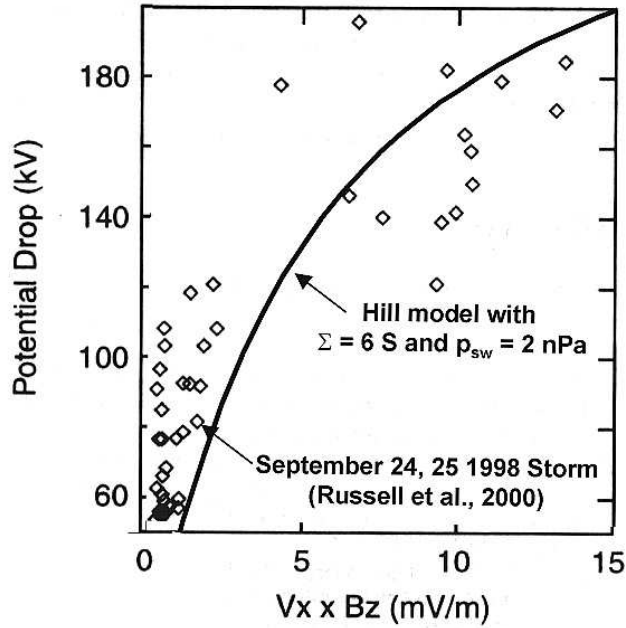


Figure 4.10: Comparison of cross polar cap potential as given by Hill/Siscoe model and data from a magnetic storm of 24, 25 September 1998 (from [Siscoe et al., 2002b])

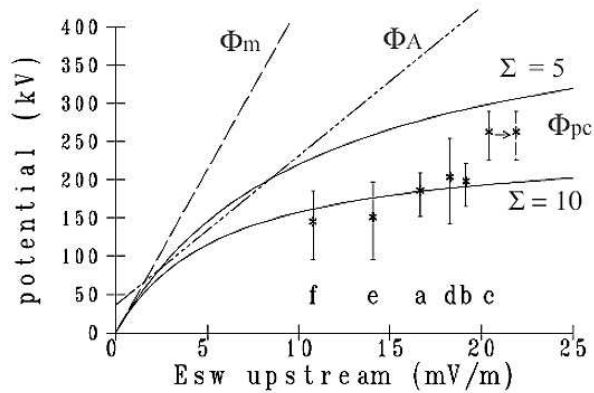


Figure 4.11: Comparison of saturation as given by Hill/Siscoe model and data from six DMSP F13 passes during a magnetic storm of 31 March 2001. The Φ_{PC} curves are the potentials from the Hill/Siscoe model with $\Sigma_P = 5$ and 10 mhos and $p_{sw} = 6.08$ nPa. The Φ_A line is the Boyle potentials [Boyle et al., 1997]. The Φ_M line is the calculated potential as given by (4.17) (from [Hairston et al., 2003])

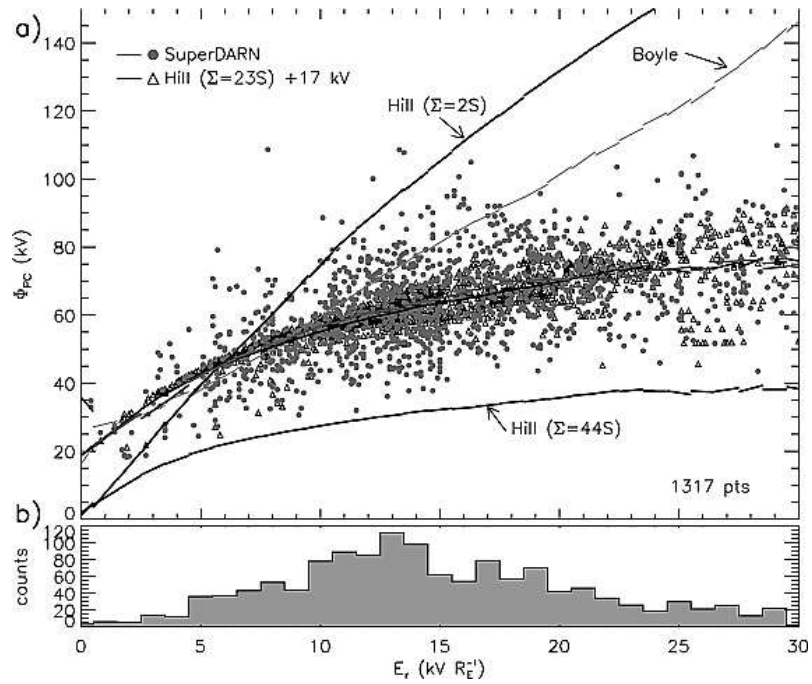


Figure 4.12: a) Cross polar cap potentials observed by SuperDARN and the best fit Hill/Siscoe model ($\Sigma = 23$ mhos and the constant potential $\Phi_0 = 17$ kV) plotted against the reconnection electric field. Also the potentials from Boyle model and Siscoe/Hill model with $\Sigma = 2$ and $\Sigma = 44$ mhos are shown. b) Distribution of events in reconnection electric field. (from [Shepherd *et al.*, 2002])

Chapter 5

Global MHD Simulations of the Earth's Magnetosphere Under Strong Southward IMF

In this chapter we discuss the results from a series of LFM simulations designed to study the behavior of the SW-M-I system under strong solar wind conditions and to investigate the effect of the Φ_{PC} saturation. In order to understand the role of the ionospheric conductance, the simulations were carried out for two values of the ionospheric Pedersen conductance. The simulations show that the cross polar cap potential is always reduced compared to the corresponding potential in the solar wind due to the stagnation of the magnetosheath flow and the existence of parallel potentials. However, it is the ionospheric conductance that affects the value of Φ_{PC} the most: the transpolar potential saturates only for high enough ionospheric conductance. A mechanism in which the ionospheric conductance changes the properties of the magnetosheath flow is proposed. This mechanism assumes mapping of the electrostatic potential in the ideal MHD system and yields a self-consistent response of the reconnection and transpolar potentials to changes in the ionospheric conductance.

5.1 Code Run Specifications

A series of simulations using the LFM code was conducted, whose objective was to understand the behavior of the SW-M-I system under various solar wind conditions. The conditions of the solar wind were ideal: the velocity had only a horizontal component which was kept constant throughout the simulation runs and equal to 400 km/s and the magnetic field was purely southward with a value from -10 nT to -40 nT. These conditions correspond to a solar wind convective electric field, E_y , in the range of 4 to 16 mV/m. In determining the simulation parameters it is important to remember that the position of the bow shock depends strongly on the magnetosonic Mach number, M_{ms} , of the solar wind flow. For low enough values of M_{ms} (lower than 2 for this code) one finds the bow shock well outside the boundary of the grid located at about $x_{GSM} = 24 R_E$. Since M_{ms} reduces when the magnetic field increases we had to adjust the density in order to keep M_{ms} above 2. As a result we could not separate effects of the convective electric field on the transpolar potential from the effects of the dynamic pressure. However, the emphasis here is not on the separate effect of the IEF but rather on the behavior of Φ_{PC} under extreme solar wind conditions corresponding to a strong geomagnetic storm. Such conditions would require the density to grow together with the IEF, because strong storms are usually associated with the arrival to the earth of large CME's, i.e. clouds of dense hot plasma from the sun. Indeed, the magnetosonic Mach number is given by

$M_{ms}^2 = v_{sw}^2 / (C_S^2 + v_a^2)$, where v_{sw} is the velocity of the solar wind, C_S is the thermal velocity, $v_a = B / \sqrt{4\pi\rho}$ is the Alfvén speed, and B and ρ are the solar wind magnetic field and mass density. Thus, due to the fact that both the solar wind magnetic field and the density rise during storms, the Mach number almost never drops lower than 2. The solar wind parameters used in the simulation runs are listed in Table 5.1.

To examine the dependence of the cross polar cap potential on the ionospheric conductance and to facilitate the interpretation of the results the conductance was taken as a uniform Pedersen conductance, Σ_P . All runs were repeated for two values of Σ_P equal to 5 and 10 mhos. The simulations were designed so that the IMF was first kept constant and positive for about 4 hours. The IMF was then turned strictly southward and the constant solar wind conditions were held long enough (typically 5 hours) so that the system evolved into the steady state [*Slinker et al.*, 1995] and the typical two-cell convection pattern was formed in the ionosphere. The parameters summarized in Table 5.1 correspond to the solar wind conditions after the southward turning of the IMF. In Fig. 5.1 the temporal evolution of Φ_{PC} over the last 5 hours of the simulation is presented. The figure shows that following the southward turning of the solar wind magnetic field at approximately $t = 40$ min, the system reaches steady state within $\sim 1 - 2$ hours. The results presented here correspond to a typical instant during steady state and the magnitude of Φ_{PC} is usually averaged over about 40 min during the steady state.

5.2 Cross Polar Cap Potential and Reconnection Potential

In the ideal MHD model and under steady state solar wind conditions the electrostatic potential is projected from the dayside magnetopause and from the magnetotail onto the polar ionosphere almost completely. The presence of non-ideal effects results in a relatively small potential attenuation due to the development of parallel electric fields along the magnetic field lines. Thus, the values of Φ_{PC} and the reconnection potential are strongly related, and should be studied together. In a global MHD code the determination of physical quantities at the magnetopause is complicated due to the problem of locating the magnetopause, the absence of reconnection physics, and contamination with numerical noise. These difficulties are overcome, at least in part, by the following technique. The extrema of the electrostatic potential are located inside the convection cells in the polar ionosphere. These points lie on the boundary separating regions of open and closed magnetic field lines, and thus the field lines originating there connect to the ends of the reconnection line on the dayside magnetopause. The potential difference between two points lying on the two field lines can be computed by integrating the parallel electric field component along the field lines. The potential drop between the two points will then be given by $\Delta\Phi = \Phi_{PC} + \Phi_{\parallel}^{(1)} + \Phi_{\parallel}^{(2)}$, where $\Phi_{\parallel}^{(1,2)}$ are the parallel potential drops along the field lines. In this representation the two quantities are positive, i.e. the electric field is integrated in opposite direction along the two field lines. For two

symmetric points (e.g. the ends of the reconnection line), the potential difference reads $\Delta\Phi = \Phi_{PC} + 2\Phi_{\parallel}$. It should be noted that the parallel electric fields in the ideal MHD code are of numerical nature and therefore the specific magnitudes of the parallel electric fields obtained from the code should not be interpreted in terms of physical processes.

A 3-D illustration of the procedure is presented in Fig. 5.2. Since the procedure is subject to noise in the simulation data as well as the integration error, the footprints of the field lines should be determined carefully to make them pass as close as possible to the ends of the reconnection line. The results of this procedure are shown in Figs. 5.3 and 5.4. Fig. 5.3 demonstrates the potential difference between the two field lines plotted against the distance from the inner boundary of the code measured along the field line. Points corresponding to $d = 0$ lie on the inner boundary and represent the corresponding cross polar cap potential while the rightmost points correspond to the potential between the field lines in the solar wind which we will refer to as the reconnection potential as explained below. In Fig. 5.4 Φ_{PC} and the reconnection potential calculated using this procedure are shown as functions of the solar wind convective electric field, E_y , for the two values of the ionospheric conductance used in the simulations. Evidently, the differences between the two corresponding curves are due to the parallel potential drop. It should be noted that in Fig. 5.4 the potential difference between the solid and dashed lines for a given value of Σ_P is the difference between points on the two magnetic field lines. Therefore, the actual

parallel potential drop along one field line is half the value in the figure. Let's consider the case with the largest parallel potential drop shown in Fig. 5.4: $E_y = 16$ mV/m and $\Sigma_P = 5$ mhos. For this case the difference between the solid and dashed line is equal to 180 kV, and thus the actual parallel potential drop along one field line is 90 kV. Further, the parallel electric field along the field lines is integrated up to the very end of the field line (where it reaches the boundary of the code grid) because of the problem locating the intersection of the field line with the magnetopause. The parallel electric field component is naturally much higher inside of the magnetopause than outside of it as can be inferred from Fig. 5.3. Moreover, beyond the bow shock the parallel electric field component becomes negligible in comparison with the total value of the electric field, but if the integration is continued over a long distance it still may give rise to a considerable potential drop as a result of accumulated numerical error. Consequently, for the specific case discussed here this procedure yields a parallel potential which is about 30-40 kV higher than the potential difference between the point where the field line touches the reconnection line and its ionospheric footprint. The potential drop upto the magnetopause is about 50-60 kV, making the total parallel potential drop of about 90 kV. The solid lines depicted in Fig. 5.4 represent overestimates of the reconnection potential and the actual value should be between the corresponding solid and dashed lines.

An attempt to calculate the reconnection potential more accurately raises new issues. The problem is that this procedure is subject to several sources of errors.

First, the footprints of the field lines that connect to the ends of the reconnection line should be chosen carefully. Due to numerical uncertainties tracing the field lines precisely from the locations of extrema of the potential on the inner boundary of the code results in the field lines that do not connect exactly to the ends of the reconnection line. Further, once the footprints have been carefully chosen the problem of finding the crossing of the field line with the magnetopause arises. As discussed earlier the computed field-aligned electric fields are naturally higher inside of the magnetopause than outside of it. So, the integration can be performed up to a point where the parallel electric field significantly reduces. Evidently, the choice of such point is associated with ambiguities. Finally, the parallel potentials calculated along the two field lines are not quite symmetric contrary to what one expects in the completely symmetrical case simulated. Summarizing all the errors, the uncertainty in the reconnection potential may be up to about 50 kV. This procedure results in the plot similar to Fig. 5.4 with the solid lines lying, as expected, lower than the ones in Fig. 5.4. But taking into account all the uncertainties in such calculation of the reconnection potential, it is more plausible to use the upper estimate of the reconnection potential instead, which is the potential difference between the field lines calculated at the edge of the code grid. The uncertainty in this potential difference is much less than in the reconnection potential determined as described above. The conclusions of this chapter are based on the assumption of the mapping of the electrostatic potential, which implies that the reconnection potential saturates similarly to the

transpolar potential. As Fig. 5.4 shows this is true for the upper estimate of the reconnection potential, and thus this is even more true for the reconnection potential, which is *a priori* smaller than the potential shown in Fig. 5.4.

The saturation of the reconnection potential is discussed in the following section. The other important feature of Fig. 5.4 is a significant difference between the values of Φ_{PC} and the corresponding reconnection potentials for different values of the ionospheric conductance. The saturation value of Φ_{PC} at $\Sigma_P = 5$ mhos is unrealistically high as compared with the experimentally observed magnitudes [Russell *et al.*, 2001; Hairston *et al.*, 2003]. However, for $\Sigma_P = 10$ mhos the situation improves: the level of $\Phi_{PC} = 300$ kV at rather high solar wind convective electric field is much closer to the observations. The fact that the ionospheric conductance affects the value of the reconnection potential is indicative of its influence on the properties of the magnetosheath flow. This is discussed in section 5.4.

5.3 Magnetosheath Flow Stagnation and Saturation of the Reconnection Potential

In this section we address the question of the role of the magnetosheath flow in formation of the reconnection potential. The ideal Ohm's law ties the convective electric field to the flow velocity. Thus, hydrodynamical properties of the flow around the magnetopause influence significantly essentially electromagnetic quantities in the system, in particular, the reconnection potential. The question is especially important for us since as we have seen in the previous section Φ_{PC}

saturation is matched by saturation of the reconnection potential, given by the reconnection electric field and the length of the reconnection line. The reconnection electric field, in turn, is determined by the properties of the magnetosheath flow. In a hydrodynamic flow past an obstacle there is always a stagnation region where the velocity component transverse to the direction of the flow grows while the parallel component is reduced. In an MHD flow, the situation is similar to the hydrodynamic case, but the frozen-in magnetic field is compressed so that the change in the convective electric field $\vec{E} = -\vec{v} \times \vec{B}$ is expected to be smaller. This is examined using the simulation for the solar wind $B_z = -40$ nT and $v_x = -400$ km/s ($E_y = 16$ mV/m), and $\Sigma_P = 10$ mhos. In this case the magnetic field at the nose of the magnetopause is compressed by a factor of ~ 3.1 while the velocity is reduced by a factor ~ 7.7 , as compared to the upstream values. This leads to a reduction of the convective electric field by more than 50%. Note that the change of the electric field across the bow shock can be neglected since the tangential component of the field must be conserved. The shock surface is quasi-perpendicular to the direction of the solar wind flow in a large region around the symmetry axis so that the electric field is mostly tangential to the shock and does not differ considerably on the two sides of the shock. Attenuation of this electric field in the magnetosheath leads to reduction of the reconnection potential.

The full magnetospheric potential taken as the product of the solar wind electric field and the characteristic size of the magnetosphere will correspond to a

line that is above all the curves in Fig. 5.4. The reason for this is the stagnation of the flow in the magnetosheath. However, the specific shape of the curves requires a more detailed analysis. The Hill/Siscoe model [*Siscoe et al.*, 2002b] described in the previous chapter provides a functional form of the transpolar potential dependence on the solar wind electric field and dynamic pressure. Further, *Siscoe et al.* [2002a] suggested that the intensity of the region 1 current is limited by the solar wind dynamic pressure under extremely disturbed solar wind conditions, which causes the saturation of the transpolar potential. It should be emphasized here that irrespective of the saturation mechanism, it should affect the global geometry of the system, and therefore, the magnetosheath flow so that the reconnection potential takes values consistent with the values of the transpolar potential. The above should be true if the assumed mapping of the electrostatic potential is valid, as expected in the ideal MHD model and under steady state conditions.

This picture is supported by testing the Hill/Siscoe model against our simulation results. In order to proceed with the comparison we rewrite (4.21) in the following form:

$$\Phi_{PC}(\text{kV}) = \frac{\alpha(\Sigma_P) E_{sw} p_{sw}^{1/3} D^{4/3} F(\theta)}{p_{sw}^{1/2} D + \beta \xi \Sigma_P E_{sw} F(\theta)} + \Phi_0, \quad (5.1)$$

where the coefficients α and β given by *Siscoe et al.* [2002b] are 57.6 and 0.01, respectively, and the notation $\alpha(\Sigma_P)$ emphasizes that α can depend on Σ_P as discussed below. In addition, we have added a constant term Φ_0 which is

common for empirical functional forms of the transpolar potential dependence on the solar wind driving function (see Chapter 4). We will look for values of α , β and Φ_0 providing the best least squares fit to our data.

It turns out that the least square error function has multiple local minima so that it is impossible to derive the only triple $\{\alpha, \beta, \Phi_0\}$ providing the best fit of the function (5.1) to the data. We overcome this problem by using the following procedure. We find the range of parameters resulting in error function lower than some threshold, e.g. 20% of the minimum transpolar potential simulated for a given value of the ionospheric conductance, and plot Φ_0 as a function of α and β in this range for the two values of the ionospheric conductance used in the simulations. The results of this procedure are shown in Fig. 5.5. The solid contours show values of Φ_0 for $\Sigma_P = 5$ mhos while the dashed contours show the same for $\Sigma_P = 10$ mhos. The parameter range shown obviously contains unphysical solutions, for example, those with too high values of Φ_0 . However, from the figure we can conclude that for any given value of the parameter β the corresponding parameter α is 1.5-2 times greater in the case of the smaller ionospheric conductance independent of the level of Φ_0 . We do not expect the parameter β to vary significantly when the conductance is changed, since it describes the magnetic field created by the figure-eight current loop in the terminator plane and depends only on the geometry of the loop and the magnetopause subsolar distance which are altered only slightly with changing conductance as we show below. Since α determines the reconnection potential in

the Hill/Siscoe model, we conclude that in order to fit to the simulation data presented here the reconnection potential in the Hill/Siscoe model should depend on the ionospheric conductance. This suggests that to explain the effect of the ionospheric conductance seen in Fig. 5.4 there should be another mechanism by which the ionospheric conductance can provide a feedback on the cross polar cap potential in addition to the mechanism of the Hill/Siscoe model. This mechanism should incorporate the influence of the ionospheric conductance on the reconnection potential.

5.4 Effect of the Ionospheric Conductance

The global MHD simulations show that the reconnection and transpolar potentials saturate as the solar wind electric field increases, as shown in Fig. 5.4. However, the saturation level depends strongly on the ionospheric conductance. We have discussed above the reduction in the cross polar cap potential arising from the stagnation of the magnetosheath flow upstream of the magnetopause. We now address the question of how the ionosphere affects the properties of the magnetosheath flow.

The role of the ionosphere in controlling magnetospheric convection as seen in global MHD simulations was first addressed by *Fedder and Lyon* [1987]. They discussed two distinct ways for such a control. First, it controls the length of the reconnection line, thus regulating the total amount of energy supplied to the ionosphere from the solar wind dynamo. Second, by regulating the strength of

the region 1 currents it influences the size of the region in the polar ionosphere through which open polar magnetic flux passes into the magnetosheath.

The ionospheric control of the SW-M-I coupling is shown in Fig. 5.6. In this figure the magnetosphere in the GSM XY plane is shown with the locations of the magnetopause and the bow shock for $\Sigma_P = 5$ mhos (solid lines) and $\Sigma_P = 10$ mhos (dashed lines). The background is the color coded plasma density on a logarithmic scale for $\Sigma_P = 5$ mhos. The solar wind electric field corresponds to the largest value used in the simulations: $E_y = 16$ mV/m. From the figure one can easily see that for the higher ionospheric conductance the magnetopause becomes wider at the flanks while the subsolar point distance does not change. This is a consequence of the increase of the region 1 Birkeland currents and the associated change in the location of the surface across which pressure balance is achieved, viz. the position of the magnetopause [Siscoe *et al.*, 2002a]. However, the constancy of the magnetopause subsolar point distance as seen in the simulations may follow from the fact that the field aligned currents do not pass close to the nose of the magnetopause and thus do not contribute to the balancing of the solar wind pressure there.

The widening of the magnetopause is accompanied by an increase in the bow shock stand off distance, as seen in Fig. 5.6. This is consistent with the results of an extensive study of the possible effects of changes in the geometry of an obstacle on the bow shock stand off distance in a supersonic MHD flow [Farris and Russell, 1998]. Following their work we made a simple estimate of what

would be the bow shock shift in our case.

Farris and Russell [1998] represent the magnetopause (the obstacle for the solar wind flow) as a general conic of revolution:

$$r = \frac{\kappa}{1 + \varepsilon \cos \theta}, \quad (5.2)$$

where r is the distance from the focus to a particular point on the curve, θ is the angle from the Sun-obstacle line to the point on the curve, ε is the eccentricity of the curve governing the shape of the obstacle, and κ is the distance from the focus to the curve for $\theta = 90^\circ$, which governs the size of the obstacle. The radius of curvature at the nose of any conic of revolution can be shown to be equal to κ . Furthermore, the stand off distance of the bow shock from the center of the obstacle, D_{BS} , is then given by [*Farris and Russell*, 1998]

$$D_{BS} = D_{OB} + R_C \cdot 0.8 \frac{(\gamma - 1)M^2 + 2}{(\gamma + 1)(M^2 - 1)}, \quad (5.3)$$

where D_{OB} is the stand off distance of the obstacle from its center (the magnetopause subsolar point distance), M is the magnetosonic Mach number of the flow, and R_C is the radius of curvature of the obstacle at the nose.

Using the values of $\gamma = 5/3$ and $M = 2.43$ appropriate for run #7 (see Table 1), to which Fig. 5.6 corresponds, we obtain

$D_{BS} = D_{OB} + 0.363R_C = D_{OB} + 0.363\kappa$. Since, as Fig. 5.6 shows, the magnetopause subsolar point distance does not change as we vary the ionospheric conductance from 5 mhos to 10 mhos, the shift of the bow shock is represented by

$$\Delta = D_{BS}(10 \text{ mhos}) - D_{BS}(5 \text{ mhos}) = 0.363[\kappa(10 \text{ mhos}) - \kappa(5 \text{ mhos})]. \quad (5.4)$$

Given that the shape and the size of the magnetopause satisfy (5.2) we can estimate κ for the particular situation represented in Fig. 5.6 . From the figure we get $\kappa(10 \text{ mhos}) = 10.25 R_E$ and $\kappa(5 \text{ mhos}) = 9.5 R_E$. Using (5.4) we find $\Delta \sim 0.3 R_E$. From Fig. 5.6 we determine this shift to be roughly $0.5 R_E$, which is consistent with the semi-empirical estimate.

The displacement of the bow shock toward the Sun while the magnetopause subsolar point distance has not changed, leads to a wider magnetosheath. This means that the flow has more space to brake, and the solar wind convective electric field is expected to be smaller on the nose of the magnetopause. In Fig. 5.7 we present the profiles of E_y along the GSM x-axis from 4 to 24 R_E . From this figure we estimate that the difference between E_y at the nose of the magnetopause for the two conductances is about 3 mV/m. The point at which the electric field is measured is displaced 1 R_E from the magnetopause subsolar point to make sure that the numerical errors arising inside of the reconnection region are not included in the calculation. Assuming a reconnection line length of 17 R_E for $\Sigma_P = 5 \text{ mhos}$ and 20 R_E for $\Sigma_P = 10 \text{ mhos}$ (which corresponds to the simulations) we get a difference of the reconnection potential of about 200 kV. A potential difference of the same order of magnitude is seen in Fig. 5.4. Thus, a slight shift of the bow shock toward the Sun by about 1 R_E leads to a significant additional drop in the reconnection potential and consequently in the cross polar cap potential. The spacial scales of the system are so large that even small variations of the electric field result in appreciable potential drops.

5.5 Effect of the Solar Wind Dynamic Pressure

In order to test a dependence of Φ_{PC} on the solar wind dynamic pressure another set of LFM model runs was conducted. In this case the solar wind electric field magnitude was constant while the density, the magnetic field, and the plasma velocity were varied appropriately. All runs were repeated for $\Sigma_P = 5$ and $\Sigma_P = 10$ mhos. The parameters of this series of simulations are summarized in Table 5.2. The last simulation (#5) on this table is the same as simulation #5 on Table 5.1. The reason it appears on the table is that it corresponds to the same solar wind electric field but different dynamic pressure and thus complements the picture of Φ_{PC} dependence on the dynamic pressure. The code as always was run until the system reached steady state and the magnitude of Φ_{PC} was averaged over about 40 min during steady state.

Fig. 5.8 shows the results of the simulation. The lines represent the best linear fit to the simulation data. The figure indicates a weak dependence of the transpolar potential on the solar wind dynamic pressure. In the case of the higher conductance the slope of the line is positive while for the lower conductance it is negative. While this can be a result of numerical errors it is clear that no conclusion can be made about the scaling of Φ_{PC} with dynamic pressure from this plot. However, the main conclusion that one draws from Fig. 5.8 is that the Φ_{PC} dependence on the solar wind dynamic pressure is much weaker than the effect of the ionospheric conductance. The range of dynamic pressure from 5 to

20 nPa covered in Fig. 5.8 represents the most typical values of the solar wind plasma from quiet to storm-like conditions. In this range, as Fig. 5.8 demonstrates, the effect of the ionospheric conductance is dominant. Note, that the Hill/Siscoe model predicts $p_{dyn}^{1/3}$ scaling of the saturated transpolar potential. In the considered range of dynamic pressure, this would result in the associated change of Φ_{PC} by a factor of ~ 1.6 , comparable to the effect of the ionospheric conductance. A possible reason for this discrepancy will be discussed later.

5.6 Discussion and Conclusions

In this chapter we studied the behavior of the steady state cross polar cap potential under solar wind electric fields in the range 4 to 16 mV/m and two values of the ionospheric conductance ($\Sigma_P = 5$ and 10 mhos) using global MHD simulations. The results of the simulations show that Φ_{PC} saturates as E_y increases, and the saturation level is strongly affected by the ionospheric conductance.

The reconnection potential at the magnetopause, which is mapped to the polar ionosphere along equipotential magnetic field lines, is determined by the properties of the flow in the magnetosheath. Thus, independent of the physical mechanism that regulates the cross polar cap potential [*Siscoe et al.*, 2002b,a] the geometry of the system and consequently the magnetosheath flow should change in a self-consistent manner. In this respect, the effect of the ionospheric conductance presented here becomes very important. The simulation clearly

indicates that under the same solar wind conditions the geometry of the magnetopause depends on the ionospheric conductance. For bigger conductances the magnetopause becomes wider at the flanks while preserving the subsolar point distance. This is a result of the increase of the region 1 currents and their possible sunward displacement on the surface of the magnetopause. The magnetopause widening leads to the bow shock shifting toward the Sun and a reduction of the convective electric field on the nose of the magnetopause. This, in turn, provides for smaller reconnection potential and consequently for smaller cross polar cap potential compared to the value at the smaller conductance.

This picture is supported by fitting the simulation data to the Hill/Siscoe model. The fitting procedure suggests that proper results are obtained only if the reconnection potential given by the Hill/Siscoe model implies a dependence on the ionospheric conductance. The ionospheric conductance feedback pertaining to the Hill/Siscoe model (the second term in the denominator of (4.21)) is insufficient to explain the difference between the two dashed curves in Fig. 5.4.

Fedder and Lyon [1987] suggested that the SW-M-I system is self-regulating. This means that an increasing power input from the solar wind to the polar ionosphere leads to an increase in the ionospheric conductance which reduces the coupling efficiency. The effect of the ionospheric conductance presented here is consistent with this picture and provides a mechanism by which the conductance can regulate the coupling of the solar wind to the magnetosphere and ionosphere.

The recent model of *Siscoe et al.* [2002b], based on the role of region 1

current, yields an analytic form of the transpolar potential and its saturation. The self-consistent relationship between the magnetosheath flow, reconnection, and transpolar potentials presented here provides a broader framework and complements the analytic Hill model [*Siscoe et al.*, 2002b].

The results of a series of additional simulations intended to study the Φ_{PC} dependence on the dynamic pressure have shown that the effect of p_{dyn} is much weaker than the effect of the ionospheric conductance. While it is important in establishing a specific shape of the Φ_{PC} functional dependence on the IEF for a constant ionospheric conductance it becomes insignificant once the latter has been varied.

In the next chapter we elaborate on the ionospheric conductance effect outlined here. Two questions should be addressed. First, the mechanism by which the change in the ionospheric conductance leads to the alterations in the magnetopause size should be described. Second, the effect of the magnetopause size on the properties of the magnetosheath should be addressed in more detail.

Table 5.1: The solar wind plasma parameters used in the simulation of the Φ_{PC} dependence on the IEF

Run #	1	2	3	4	5	6	7
B_z , nT	-10	-15	-20	-25	-30	-35	-40
V_x , km/s	-400	-400	-400	-400	-400	-400	-400
n , cm^{-3}	5	5	5	15	20	25	30
E_y , mV/m	4	6	8	10	12	14	16
M_{ms}	3.81	2.65	2.02	2.73	2.64	2.53	2.43

Table 5.2: The solar wind plasma parameters used in the simulation of the Φ_{PC} dependence on the solar wind dynamic pressure

Run #	1	2	3	4	5
B_z , nT	-25	-20	-15	-25	-30
V_x , km/s	-480	-600	-800	-480	-400
n , cm^{-3}	20	20	20	30	20
E_y , mV/m	12	12	12	12	12

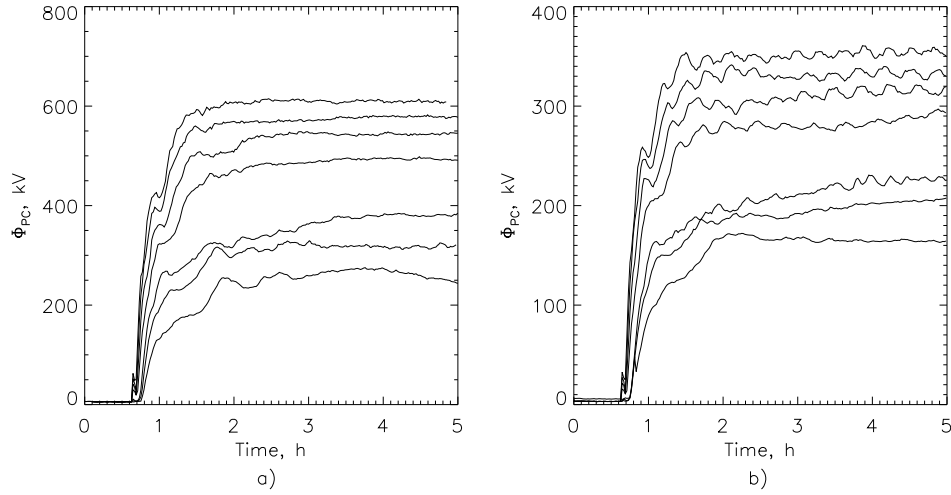


Figure 5.1: Temporal evolution of the cross polar cap potential over the last five hours of simulation. a) $\Sigma_P = 5$ mhos, b) $\Sigma_P = 10$ mhos. On the two plots the curves from the lowest to the highest represent runs from #1 to #7, respectively (see Table 5.1).

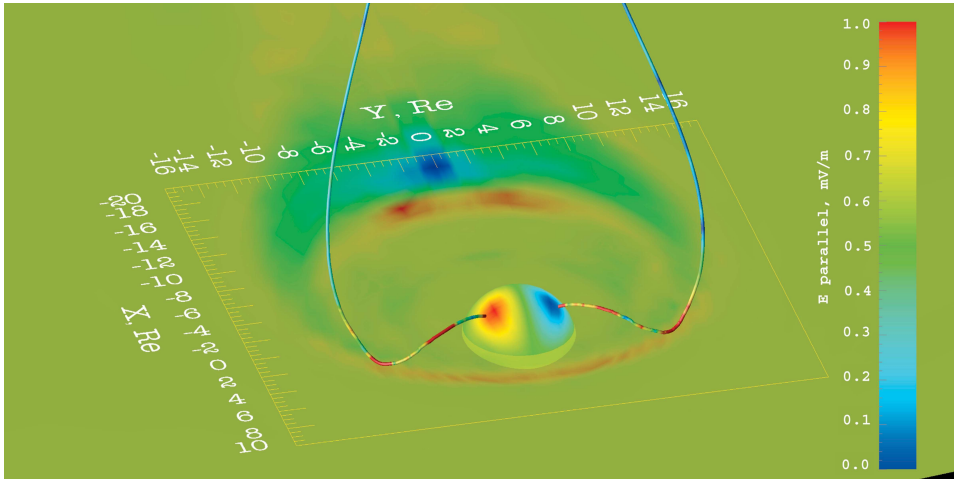


Figure 5.2: A 3D illustration of the magnetic field lines attached to the locations of the extrema of the electrostatic potential in the ionosphere. The background represents the z -component of the plasma velocity in the GSM $z=1$ plane so that the reconnection line is easily identified. The magnitude of the parallel electric field is color coded and plotted over the field lines. Also, the electrostatic potential pattern on the inner boundary of the code is shown in color.

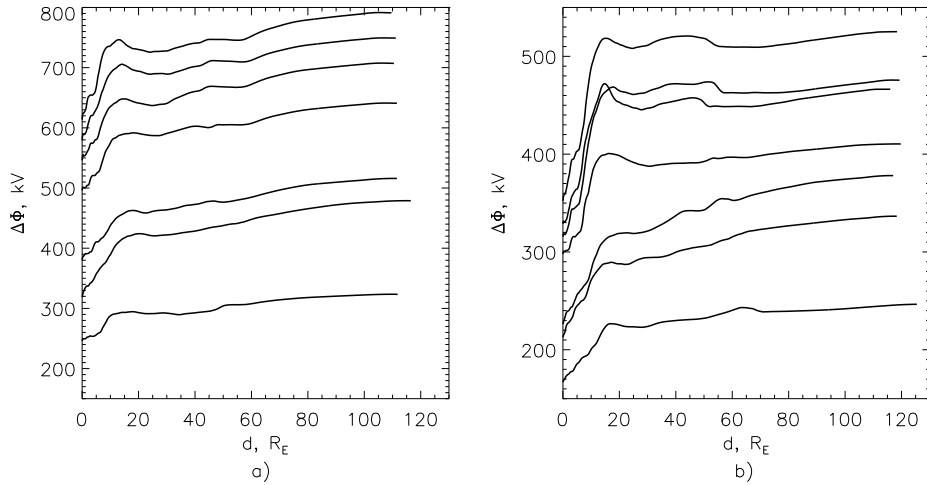


Figure 5.3: Potential drop between the field lines, $\Delta\Phi$, as a function of the distance from the inner boundary along the field line, d . The leftmost point on every curve lies on the inner boundary and represents the corresponding cross polar cap potential; the rightmost point corresponds to the potential between the field lines in the solar wind. a) $\Sigma_P = 5$ mhos, b) $\Sigma_P = 10$ mhos. On both plots the curves with the corresponding cross polar cap potential from the lowest to the highest represent runs from #1 to #7, respectively.

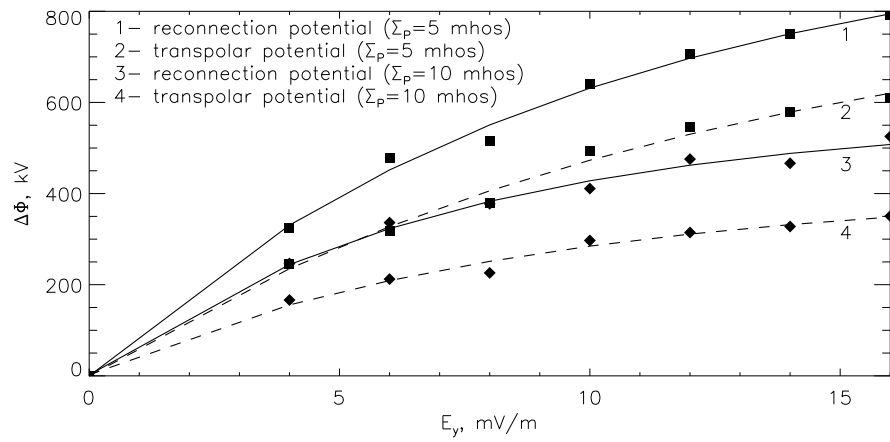


Figure 5.4: The dependence of the cross polar cap potential and reconnection potential, $\Delta\Phi$, on the solar wind convective electric field, E_y . The lines are a fit to the simulation data.

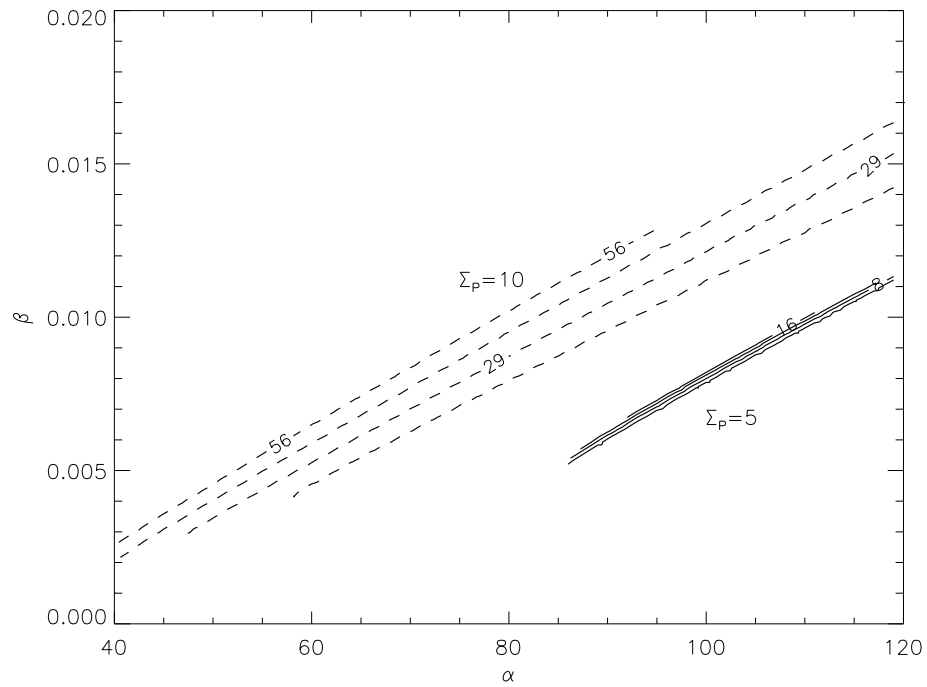


Figure 5.5: Contours of the constant term Φ_0 in α, β space. The parameters shown here result in the least squares error function which is less or equal than 20% of the minimum transpolar potential simulated for a given value of the ionospheric conductance. The dashed lines represent $\Sigma_P = 10$ mhos, while the solid lines are for $\Sigma_P = 5$ mhos.

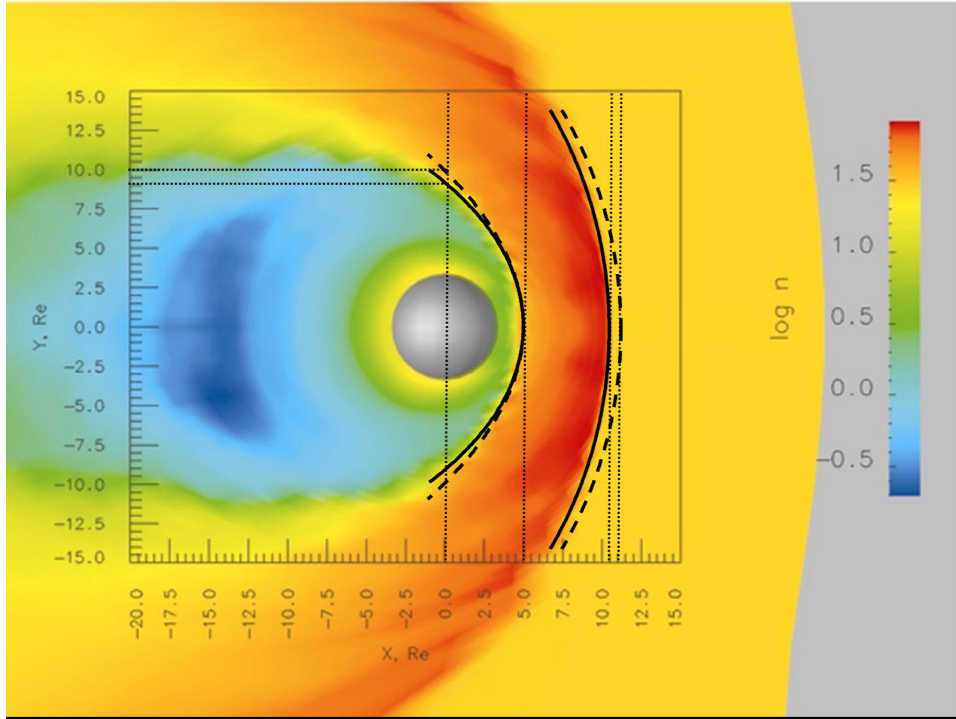


Figure 5.6: The magnetopause and the bow shock for the run #7. The background is color coded plasma density on a logarithmic scale for $\Sigma_P = 5$ mhos. The curves are of the form $r = \kappa/(1 + \varepsilon \cos\theta)$ where κ and ε are found from subsolar and terminator distances determined by the density jump.

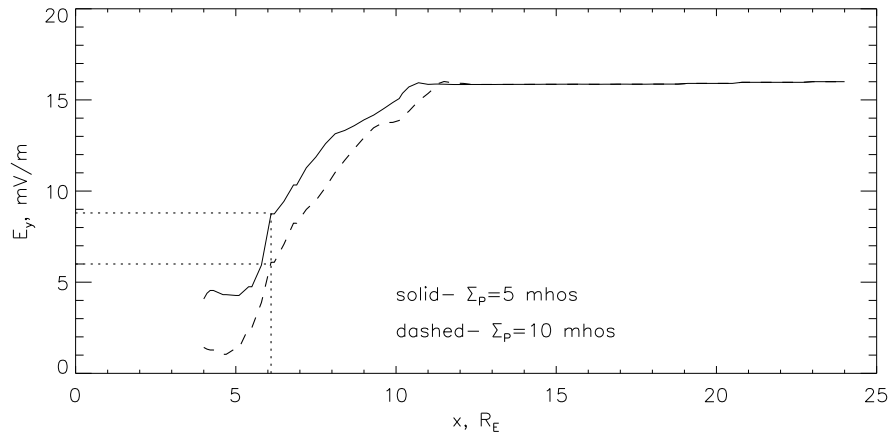


Figure 5.7: Profiles of E_y along the GSM x-axis in the magnetosheath for the run #7. The vertical dotted line represents the location of the point moved about 1 R_E toward the Sun from the magnetopause subsolar point as determined from the density jump (see Fig. 5.6). This is to make sure that numerical errors arising from the solution inside of the reconnection region are not included in the calculation.

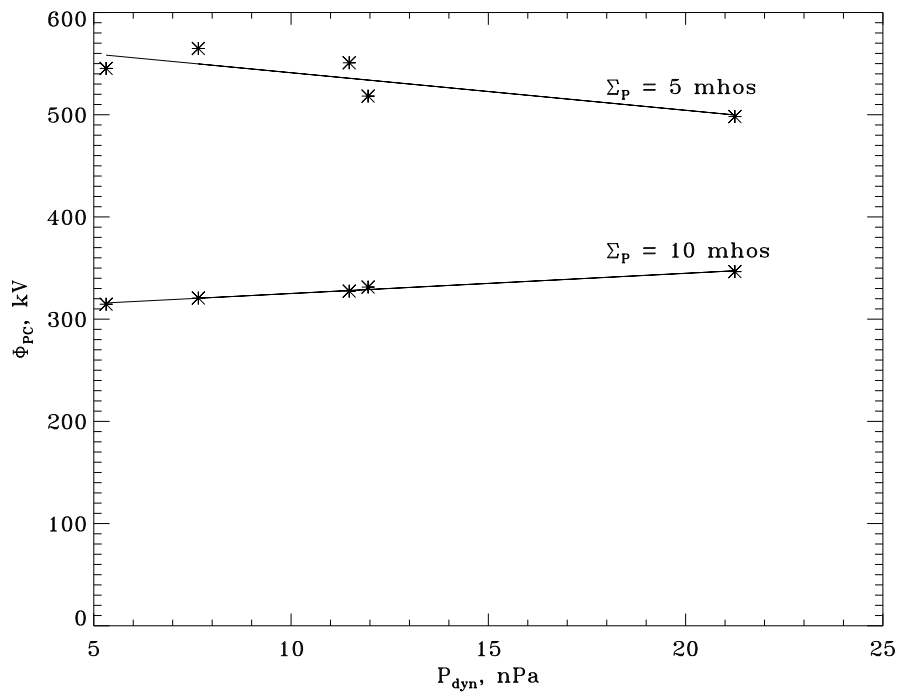


Figure 5.8: The dependence of the steady state transpolar potential on the solar wind dynamic pressure for the shown values of the ionospheric conductance and $E_y = 12$ mV/m for the solar wind electric field. The lines represent the best linear fit to the simulation data.

Chapter 6

Ionospheric Conductance Control of the Magnetopause Size and Magnetosheath Flow

In this chapter we present a study of the role of the ionospheric conductance in the control of the magnetopause size and location and of the influence of the resultant geometry of the magnetopause on the properties of the flow in the magnetosheath. A set of global MHD simulation runs used in this chapter is designed to isolate the effects of the ionospheric conductance. We show that the field-aligned currents, whose magnitude depends on the ionospheric conductance, affect the size of the magnetopause at the flanks by increasing the local magnetic pressure and thus altering the surface equilibrium at the magnetopause. A current system is identified that generates the magnetic stresses controlling the location and geometrical structure of the magnetosphere observed in the simulations. A change in the geometry of the magnetopause resulting from this mechanism leads to changes in the magnetosheath flow even for a constant solar wind input. This provides a feedback of the ionospheric conductance on the reconnection potential and, consequently, on the cross polar cap potential.

6.1 Introduction

The magnetopause is usually defined as a surface of the total pressure balance: the earth's dipole magnetic field pressure with small contribution from the thermal plasma pressure inside the magnetopause balances the outside solar wind dynamic pressure. Further, the solar wind flow velocity is tangential to the pressure-balanced surface of the magnetopause at all points (in the absence of reconnection). As a result the magnetopause is often considered as an obstacle in the way of the solar wind flow. Some aspects of the solar wind-magnetosphere interaction have been studied in a manner similar to the problem of a supersonic hydrodynamic flow past an obstacle [e.g. *Petrinec and Russell, 1997*, and references therein]. The location, size, and the shape of the magnetopause are determined by the fluid properties of the solar wind and by the conditions of the internal magnetic field and plasma which are affected by the ionospheric conductance. In this chapter it is conclusively demonstrated using global MHD simulations that the value of the ionospheric conductance plays a critical role in controlling the geometric properties of the magnetopause surface in steady state. As a result the flow in the magnetosheath can be significantly modified while the solar wind conditions upstream of the bow shock remain the same. Such situation can result in dramatic changes in the behavior of the SW-M-I system.

In the previous chapter we have outlined the mechanism of the ionospheric conductance feedback on the reconnection and transpolar potentials. In this

chapter we present a detailed study of this mechanism based on the LFM global MHD simulations. The LFM simulation runs used in this study were designed to separate the effect of the ionospheric conductance on the SW-M-I coupling.

Thus, the solar wind input conditions were fixed and only the Pedersen ionospheric conductance was varied. The following solar wind parameters were used: $v_x = -400$ km/s, $B_z = -40$ nT, $n = 30$ cm⁻³, corresponding to purely anti-sunward solar wind velocity and southward magnetic field. The Pedersen conductance, Σ_P , was taken equal to 1, 2.5, 5, 10, 15 and 20 mhos, respectively. In each case the code was run until the system reached steady state as described in the previous chapter.

6.2 Effect of the Ionospheric Conductance on the Transpolar Potential and the Size of the Magnetopause

Figure 6.1a shows the dependence of the cross polar cap potential and of the ionospheric integrated field aligned current averaged over about 40 minutes during steady state on Σ_P . As the conductance changes from 1 to 20 mhos, Φ_{PC} drops by a factor of approximately 6: from 1200 kV to 200 kV, demonstrating a key role of the ionospheric conductance in regulating the transpolar potential (note that the solar wind conditions are the same for all shown simulations).

Correspondingly, the field aligned current grows from about 5 MA to 10 MA.

The current and the voltage turn out to satisfy the relation $I_1 = \xi \Sigma_P \Phi_{PC}$ where ξ is a coefficient dependent on the geometry of the currents in the ionosphere with a value between 3 and 4. This is consistent with the results of *Siscoe et al.*

[2002b]. An important feature of Fig. 6.1a is the presence of clear saturation effects on both quantities.

An important result of the study shown in Fig. 6.1b demonstrates the dependence of the size of the magnetopause on the conductance Σ_P . Here the size of the magnetopause is defined as the distance between the center of the earth and the magnetopause along y-direction. This distance is determined by the location of the jump of the mass density measured along the GSM y-axis.

Figs. 6.1a,b show that the effect of the ionospheric conductance on the transpolar potential outlined in the previous chapter is robust, i.e. it shows a clear tendency of Φ_{PC} to decrease as the ionospheric conductance increases when the solar wind conditions remain the same. In addition, the connection between the size of the magnetopause and the values of Φ_{PC} becomes evident from 6.1b. In the next sections the physical mechanism of such dependence is discussed.

6.3 Pressure Balance and the Magnetopause Size

As noted previously the magnetopause equilibrium requires balance of the total pressure across the discontinuity. As follows from the simulations described above, an increase in the ionospheric conductance results in production of additional pressure inside of the magnetopause since for the same solar wind dynamic pressure upstream of the bow shock, the magnetopause is found farther from the earth (at least at the flanks). Our methodology searches for the sources of additional pressure required to satisfy the total pressure balance condition at

the flanks of the magnetopause. In attempting to follow this method a difficulty arises in measuring the quantities across the magnetopause surface in the code due to the uncertainty in its location. To avoid this difficulty we first measure the size of the magnetopause and then recast the pressure balance equation in terms of the measured size.

The size of the magnetopause can be measured fairly easily in the simulations and the measurement error can be estimated from the code resolution. In the so called Newtonian approximation the pressure balance condition at any given point of the magnetopause can be written as [*Spreiter et al.*, 1966]:

$$\frac{(2fB_{dip})^2}{8\pi} = \varkappa\rho v_{sw}^2 \cos^2 \theta, \quad (6.1)$$

where the variables are the dipole magnetic field inside the magnetopause (B_{dip}), the density of the plasma in the magnetosheath (ρ), and the angle between the magnetopause normal and the earth-sun line or the flaring angle (θ). It was assumed here that the compressed dipole magnetic field has a value twice its uncompressed value and the coefficient f describes deviation from this assumption. The coefficient \varkappa represents the ratio of the stagnation point static pressure to the solar wind dynamic pressure upstream of the bow shock as well as the uncertainty in the Newtonian approximation. On the symmetry axis of the flow (where $\theta = 0$) the coefficient \varkappa can be obtained analytically by considering a purely hydrodynamic problem [*Landau and Lifshitz*, 1959]. For flow Mach numbers greater than 2 (normally the Mach number of the solar wind flow is

much higher) \varkappa is less than 1 and tends steeply to the value of 0.88 with increasing Mach number. In general, according to [Sibeck *et al.*, 1991] \varkappa may range from 0.67 to 1.0 and f from 1.0 to 1.5.

For the reasons discussed above we need to recast (6.1) in terms of the geometric characteristics of the magnetopause. To proceed with this task we describe the magnetopause as a general conic of revolution:

$$r = \frac{\kappa}{1 + \varepsilon \cos \phi}, \quad (6.2)$$

where r is the distance from the focus (center of the earth) to a particular point on the surface, ϕ is the angle from the earth-sun line to the point on the surface, ε is the eccentricity, which governs the shape of the magnetopause, and κ is the distance from the focus to the surface for $\phi = 90^\circ$, that is the size of the magnetopause as it is defined above.

We need to derive a relationship between κ and $\cos \theta$. It is easy to show that the equation for the normal to the conic of revolution at the point $\phi = 90^\circ$ is

$$\vec{n} = \frac{1}{\sqrt{1 + \varepsilon^2}} \begin{pmatrix} \varepsilon \\ 1 \end{pmatrix}, \quad (6.3)$$

where \vec{n} is a two-dimensional unit length vector lying in a plane containing the symmetry axis of the conic. Consequently,

$$\cos \theta = \frac{\varepsilon}{\sqrt{1 + \varepsilon^2}}. \quad (6.4)$$

The magnetopause subsolar point distance, D , is determined from (6.2) when

$\phi = 0$:

$$\frac{\kappa}{1 + \varepsilon} = D. \quad (6.5)$$

Finally, express ε in terms of κ and D and substitute to (6.4):

$$\cos \theta = \frac{\frac{\kappa}{D} - 1}{\sqrt{1 + \left(\frac{\kappa}{D} - 1\right)^2}}. \quad (6.6)$$

Equation (6.6) allows us to recast the solar wind dynamical pressure at the surface of the magnetopause on the right hand side of (6.1) in terms of distances easily measured in the simulations.

6.4 Field Aligned Current System and the Size of the Magnetopause

The ionosphere is physically connected to the magnetopause at the flanks by means of field-aligned currents. They produce a magnetic field that is added to the dipole field thus modifying the total pressure inside the magnetopause. Since the magnetopause is the surface of the total pressure balance, the magnetic field of the field-aligned currents can modify the shape of the surface itself. The idea that the field aligned currents can significantly change the structure of the magnetic field inside the magnetopause was discussed earlier by *Maltsev and Lyatsky* [1975]. They proposed a model linking the erosion of the magnetopause during the early stages of the magnetospheric substorms to the distortion of the dipole magnetic field at the subsolar point by the additional magnetic field produced by the field aligned current loop. Further, the Hill/Siscoe model of the cross polar cap potential saturation [*Siscoe et al.*, 2002b] is based on the

hypothesis that the dipole magnetic field at the subsolar point is reduced significantly by the magnetic field due to the field aligned current. We will use the same idea but apply it to the problem of determining the magnetopause location at the flanks rather than at the subsolar point. This approach is in agreement with [Siscoe *et al.*, 2002a].

6.4.1 Figure-Eight Field Aligned Current

Following [Siscoe *et al.*, 2002b] we start by considering the field aligned current as a figure-eight loop in the terminator plane, that drives a magnetic field in the x-direction at the flanks thereby enhancing the dipole magnetic pressure. As a result the flaring angle increases and the location of the magnetopause changes to accommodate for new pressure balance conditions while the solar wind remains constant.

We consider below two simulated cases, $\Sigma_P = 2.5$ mhos and $\Sigma_P = 10$ mhos, and calculate the additional magnetic pressure produced by the field aligned currents along with the difference in the flaring angle. Including the contribution of the field aligned currents the magnetic pressure inside the magnetopause becomes

$$P = \frac{(2fB_{dip})^2}{8\pi} + \frac{B_x^2}{8\pi}. \quad (6.7)$$

Assuming that only the change in the ionospheric conductance is responsible for widening of the magnetosphere at the flanks while the compressed dipole field

and the coefficients \varkappa and f remain the same, from (6.1) we find

$$\frac{\Delta\left(\frac{B_x^2}{8\pi}\right)}{\rho v_{sw}^2} = \varkappa \Delta(\cos^2 \theta), \quad (6.8)$$

where the dipole part of the field has been canceled. For the sake of simplicity assume that the magnetopause is a circle in the terminator plane and the north and the south current loops are the circles of the half-diameter of the magnetopause with centers lying on the z -axis. The direction of the current is counterclockwise for the northern loop and clockwise for the southern loop. The magnetic fields created by the two loops at the flanks of the magnetopause will cancel each other on the GSM y -axis, but not off the axis. The total magnetic field driven by the current system at the right (positive y_{GSM}) flank of the magnetopause at the elevation from the equatorial plane equal to $z = \delta r$, where r is the radius of one of the loops (half-radius of the magnetopause) and δ is the fraction of the loop radius characterizing the elevation, can be found as

$$B_x = B_+ - B_-, \quad (6.9)$$

where

$$B_{\pm} = \frac{I}{cr} \int_0^{2\pi} \frac{A_{\pm} \cos \theta - 1}{1 + A_{\pm}^2 - 2A_{\pm} \cos \theta} d\theta. \quad (6.10)$$

Here B_{\pm} is the magnetic field from the northern/southern current loop, I is the current, c is the speed of light and $A_{\pm} = \sqrt{4 + (1 \mp \delta)^2}$. The integral in (6.10) computed numerically yields $B_x = 0.12 \text{ MA}/cR_E$ for $\Sigma_P = 2.5$ mhos and $B_x = 0.10 \text{ MA}/cR_E$ for $\Sigma_P = 10$ mhos. As a result the figure-eight model of the

field aligned current results in the erroneous sign of the change in the magnetic field; the additional magnetic pressure decreases while we expect it to increase with increasing current. This inconsistency is obviously due to the specific geometry of the current loop chosen here. The important aspect is that a current of such or similar geometry cannot provide sufficient magnetic pressure at the flanks of the magnetopause to account for the magnetosphere widening seen in the simulations. According to (6.8) we find

$$\Delta(\cos^2 \theta) \simeq 10^{-4}. \quad (6.11)$$

This is a negligible difference in the flaring angle as compared to $\Delta(\cos^2 \theta) \simeq 10^{-1}$ calculated from the simulation results using (6.6).

6.4.2 Field Aligned Current Inferred from the Simulations

The above considerations lead to the conclusion that the current should flow along a different path that provides a stronger magnetic field at the flanks. Indeed, the profile of the magnetic field x-component measured along the y-axis in the $z=1$ plane (Fig. 6.2) suggests that the field aligned current has a structure different from that described above. The upward (northward) current would produce a magnetic field in the negative x-direction (for positive y and z quadrant). However, from Fig. 6.2 one can see that closer to the magnetopause the magnetic field driven by the field aligned current becomes sunward and reaches a rather high level. This can be the case only if there is a southward current flowing close to the surface of the magnetopause. Also, the upward

direction of the magnetopause current increases this sunward magnetic field even more. This suggests the current configuration shown schematically in Fig. 6.3a. Indeed, we see signatures of such current system in our simulations (Fig. 6.3b). This figure shows the z-component of the current density on a logarithmic scale in the terminator plane. If the measurement was taken exactly in the equatorial plane the southern and the northern current loops would cancel each other's magnetic field exactly as it would happen for the figure-eight current. However, for the $z=1 R_E$ plane, the current loop shown in Fig. 6.3a drives a rather strong positive x-directed magnetic field at the flank (for positive y and z coordinates) just between the downward and upward current branches. Comparing the magnitudes of the field for the selected cases ($\Sigma_P = 2.5$ mhos and $\Sigma_P = 10$ mhos) we can estimate the variation in the flaring angle produced by the corresponding change of the magnetic pressure inside the magnetopause. The observed x-component of the magnetic field is found to be approximately 40 nT and 55 nT, respectively. Repeating the calculations from the previous section and using (6.8) we obtain

$$\Delta(\cos^2 \theta) \simeq 8 \cdot 10^{-2}, \quad (6.12)$$

which is very close to the value 10^{-1} seen in the simulations (see previous section).

To verify the suggested field aligned current geometry we consider the pressure balance at the flanks of the magnetopause for a number of simulations.

A straightforward way of doing this would be to check the dependence of the field aligned current on the pressure just outside the magnetopause. This dependence is expected to form a straight line in the (I^2, P) space, where I is the ionospheric integrated field aligned current magnitude and P is the total pressure $p + B^2/8\pi$ just outside of the magnetopause at its flanks, since the additional magnetic field produced by the current I is proportional to its magnitude. As mentioned earlier measuring physical quantities at the surface of the magnetopause is complicated in the code. This is why we will utilize the results of Section 6.3, i.e. use the Newtonian approximation for the total pressure outside of the magnetopause and rewrite it using the distances which are easy to measure.

Using (6.6) we can recast the total pressure from outside the magnetopause in terms of the size κ and the subsolar point distance D . Having done this we can calculate $\cos \theta$ for each case since we are able to measure κ and D and we can estimate the error of measurement. According to (6.1) the dependence of $\cos \theta$ on the ionospheric field aligned current is expected to be linear in terms of squared magnitudes. In Fig. 6.4 we present this dependence along with the error bars calculated assuming that the accuracy of measuring κ and D is equal to $\sim 0.3 R_E$ as given by the local code resolution. The figure clearly indicates the expected linear dependence. Note that Fig. 6.4 demonstrates the results of the simulations, in which only the ionospheric conductance was varied while the solar wind conditions remained constant. This result shows how the ionospheric conductance controls the size of the magnetopause: By regulating the strength of the field

aligned current it influences the location of the pressure-balanced magnetopause surface. The squared magnitudes of the current and the cosine of the flaring angle are in a simple linear relation, provided that the solar wind input is constant.

6.5 The Magnetopause Size and the Flow in the Magnetosheath

So far we have discussed the ionospheric control of the magnetopause size. We have introduced a concept of the magnetopause as an obstacle in the way of the solar wind and we have seen in Chapter 5 how a change in the size of the obstacle influences the flow in front of it. We now address a question of how the geometry of the magnetopause affects the properties of the magnetosheath flow and the reconnection potential in more detail.

Fig. 6.5 sheds some light on this problem. In this figure the magnetosphere is shown in the $z = 1$ plane simulated for $\Sigma_p = 1$ and $\Sigma_p = 10$ mhos. The background is the plasma mass density on a logarithmic scale. In addition, streamlines of the flow, originating upstream of the bow shock at equidistant points with y -coordinate ranging from 0.5 to $3 R_E$ lying in the plane, are shown. The lines in the figure are, in fact, projections of the 3-dimensional streamlines on the plane. Therefore, the lines that seem to penetrate the magnetopause actually reach the dayside reconnection line and hence are diverted in the z -direction giving an impression that they get across the magnetopause boundary. Along with overall differences in the geometry of the system in Figs. 6.5a,b, i.e. the size of the magnetopause, the width of the magnetosheath, and the bow shock stand

off distance, the figures show how the magnetosheath flow responds to such changes in the geometry of the system. In the case of the greater conductance (the wider magnetopause) the deflection of the flow in the magnetosheath is much stronger so that only the streamline originating almost at the symmetry axis reaches the reconnection line while the other streamlines "skim" the obstacle. Unlike this case, the flow in Fig. 6.5a, corresponding to the smaller ionospheric conductance, experiences almost no deflection in the magnetosheath (in accordance with the small size of the obstacle and thinner magnetosheath) and all the shown streamlines reach the dayside reconnection line.

This picture elucidates why the reconnection potential and consequently the transpolar potential are smaller in the case of the greater conductance. In the ideal MHD context the streamlines are equipotential just like the magnetic field lines. This results from the ideal Ohm's law $\vec{E} = -\frac{1}{c}\vec{v} \times \vec{B}$, which states that the electric field vector is always normal to both the magnetic field and the velocity. A streamline is, by definition, a line tangential to the velocity vector at any point, and therefore, the electric field component parallel to a streamline is identically equal to 0. In an ideal symmetric situation with due southward IMF, as in Figs. 6.5a,b, there always exist two "special" streamlines that connect to the ends of the dayside reconnection line. The potential difference between these streamlines defines the reconnection potential, and the distance between them upstream of the bow shock is determined by the degree of deflection of the flow in the magnetosheath. We will refer to the segment of the solar wind flow between

these lines upstream of the bow shock to as the "image" of the reconnection line in the solar wind. The size of this segment is obviously smaller in the situation depicted in Fig. 6.5b than in Fig. 6.5a. This leads us to an anti-intuitive conclusion that despite a little longer reconnection line in the case of a wider magnetopause, the reconnection potential is actually smaller in this case, since the distance along which the electric field is integrated in the solar wind to obtain the potential drop across the image of the reconnection line is shorter. Note, that the plasma parameters upstream of the bow shock are completely identical in the two cases, and hence, the change in the reconnection potential is determined by the change in the size of the image of the reconnection line.

This approach is basically equivalent to the explanation of the reconnection potential difference given in Section 5.4. Changes in the size of the magnetopause, the width of the magnetosheath, and the location of the bow shock are all parts of the same process. Braking of the flow in the magnetosheath leading to a drop in the electric field on the nose of the magnetopause is identical to the concept of the stronger deflection of streamlines in case of a higher ionospheric conductance.

To verify our conclusion about shrinking of the image of the reconnection line accompanying an increase in the ionospheric conductance we need to extend our study to a number of simulated cases. In order to obtain the size of the image of the reconnection line we adopt the following technique. Consider the flow in the equatorial plane. The streamlines originating inside the image are expected to reach the reconnection line, and thus, the z-component of the flow velocity

measured along these streamlines should experience a jump as fluid elements moving along the streamlines cross the reconnection region. On the other hand, the streamlines originating outside of the image, are deflected in the same plane and are not expected to have a significant z -component of the velocity. The streamlines that connect to the ends of the reconnection line skim the obstacle. This is unlike a hydrodynamic flow where the boundary of the section of the obstacle by the equatorial plane would coincide with the streamline originating infinitely close to the symmetry axis. By measuring the maximum z -component of the velocity along a streamline one can distinguish between the populations of streamlines starting inside and outside of the image of the reconnection line. In Fig. 6.6 the results of this procedure are shown. The plots correspond to different values of Σ_P shown in the upper right corner of each plot. The horizontal axis shows the starting y -positions of streamlines (y_0) while the vertical axis shows the maximum z -component of the plasma velocity measured along a particular streamline. The black arrows indicate an approximate location of the end of the image of the reconnection line. The product of the solar wind electric field and $2y_0$ gives the reconnection potential. While it is obvious that no quantitative information can be extracted from these plots due to appreciable width of the transition region from high to low maximal v_z , the tendency of the size of the image as indicated by the black arrows to shrink with increasing conductance (i.e. the size of the magnetopause) is clear. Note, that v_z does not vanish as y_0 is increased. This is because the shown streamlines originate in the $z = 1$ plane

rather than in the equatorial plane.

6.6 Ram Pressure Effect Revisited

We now return to the question of the solar wind ram pressure on the saturated transpolar potential discussed in subsection 5.5. As noticed earlier, a number of tests showed that the solar wind dynamic pressure, while being important in establishing a specific shape of the functional dependence of the potential on the IEF, plays a much smaller role in controlling the saturated potential as compared to the ionospheric conductance. As our simulations showed, the saturated cross polar cap potential experiences almost no dependence on the solar wind dynamic pressure as opposed to the Hill/Siscoe model that predicts $p_{dyn}^{1/3}$ scaling, which follows from Chapman-Ferraro scaling. A reason for this discrepancy may be in the fact that while the solar wind dynamic pressure works to compress the magnetopause (Chapman-Ferraro scaling) and shorten the dayside reconnection line, the results discussed in subsection 6.5 suggest that a smaller magnetopause deflects the flow less effectively and the geoeffective distance in the solar wind is larger in this case. Thus, although the reconnection line shrinks as dynamic pressure increases, its image in the solar wind grows, and the effect of the dynamic pressure on the reconnection potential is significantly weakened.

6.7 Conclusions

In this chapter we described a series of LFM model simulations intended to study the effect of the ionospheric conductance on the geometry of the magnetopause

and properties of the magnetosheath flow for an invariant solar wind input. It was found that the ionospheric conductance controls the size of the magnetopause at the flanks by means of the field aligned currents. The current system creates an additional magnetic pressure inside the magnetopause that changes the pressure balance at its surface.

We considered two cases of the field aligned current systems. The figure-eight current loop was shown to be inconsistent with the magnetopause size change seen in the code. The additional magnetic pressure produced by such a current system is too weak at the flanks of the magnetopause. On the other hand, the simulations suggest a different path for the field aligned current closure. The additional magnetic field driven by the proposed current system has been shown to be consistent with the increase in the magnetopause size observed in the simulations. Further analysis demonstrated that the integrated ionospheric field aligned current and the size of the magnetopause are in a simple algebraic relation based on analytic pressure balance considerations.

We discussed so far the effect of the ionospheric conductance on the geometry of the magnetopause for a constant solar wind. The alterations in the size of the magnetopause, in turn, result in a reconfiguration of the magnetosheath flow in response to the change of the boundary conditions. The size of the geoeffective segment of the solar wind, i.e. the segment of the flow that reaches the dayside reconnection line, depends on the size of the magnetopause. A wider magnetopause requires a smaller image of the reconnection line because it

deflects the flow more effectively than a smaller magnetopause.

The described chain of events provides a feedback of the ionospheric conductance on the reconnection potential and consequently the transpolar potential. This lays a foundation for a phenomenological model of the transpolar potential saturation which will be described in the last chapter of this dissertation.

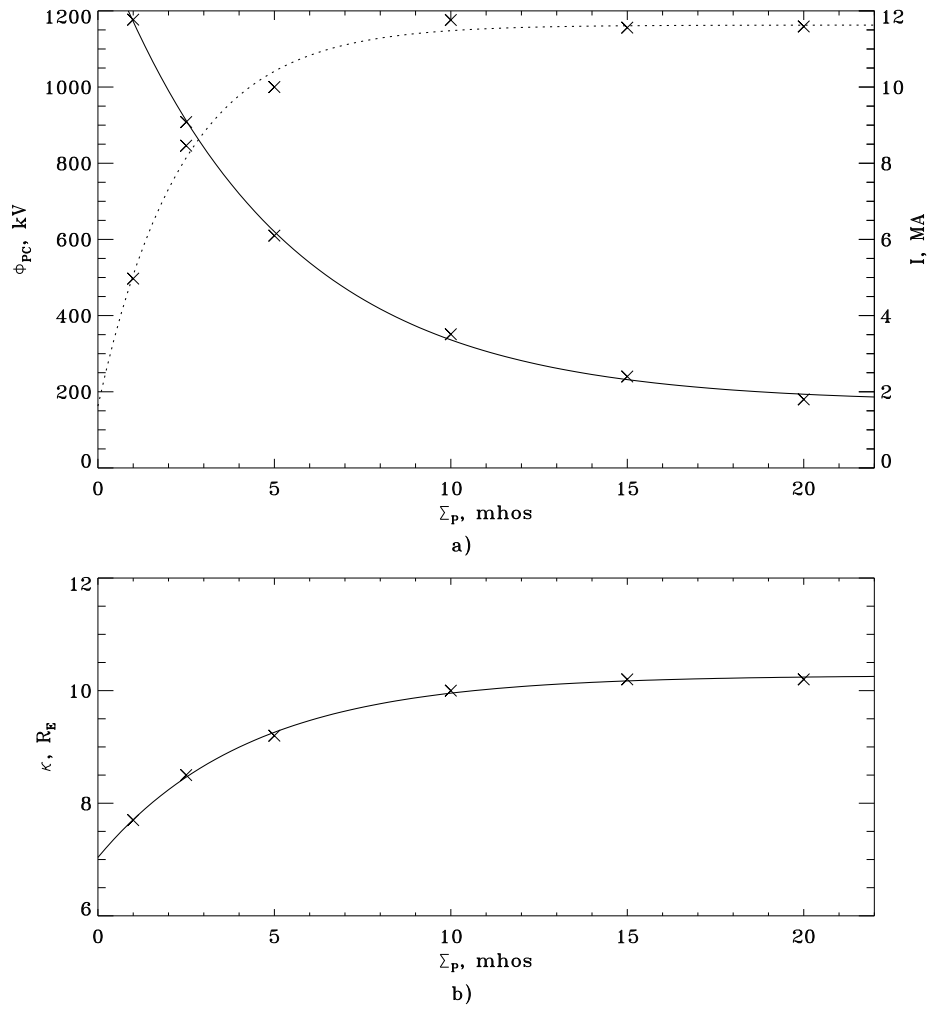


Figure 6.1: The dependence on the ionospheric Pedersen conductance: a) of the cross polar cap potential (solid line) and the ionospheric field aligned current (dashed line); b) of the magnetopause size in the terminator plane, κ .

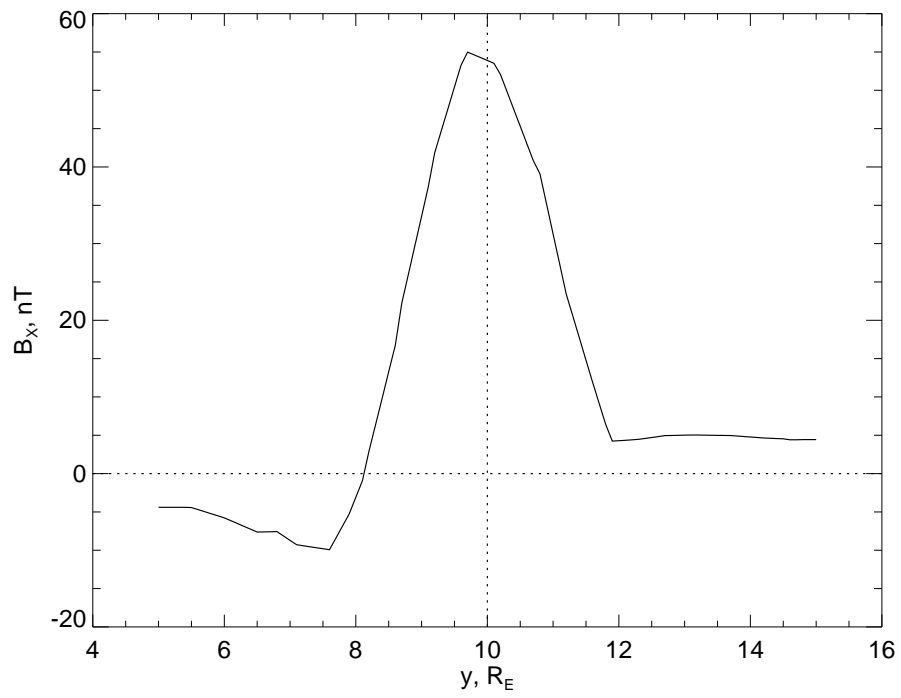


Figure 6.2: Profile of B_x along the GSM y -axis in the terminator plane. The vertical dashed line denotes the location of the magnetopause as defined by the jump of the density.

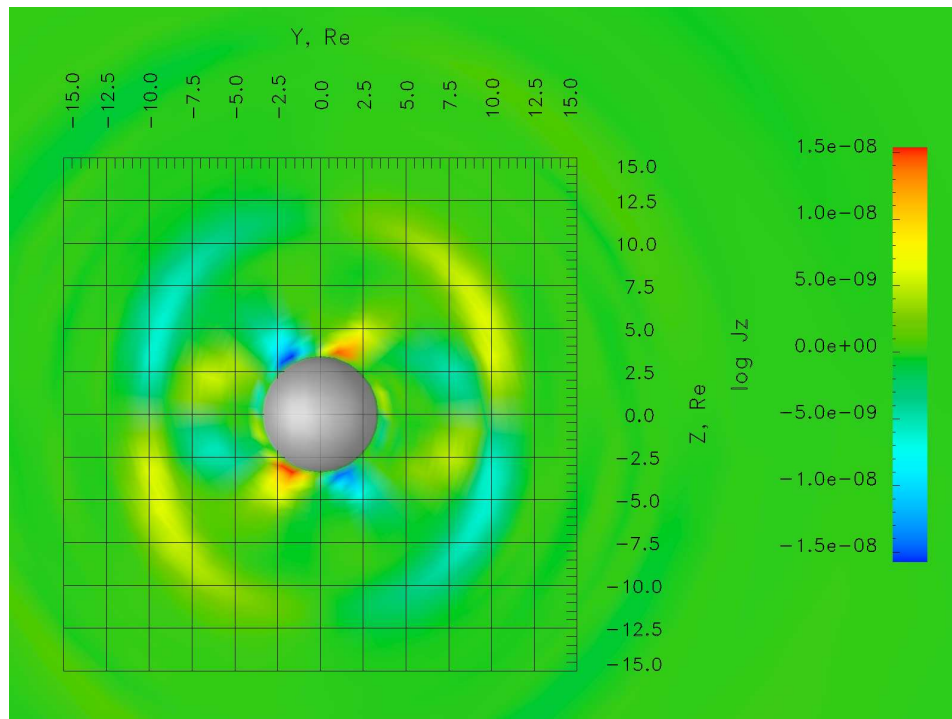
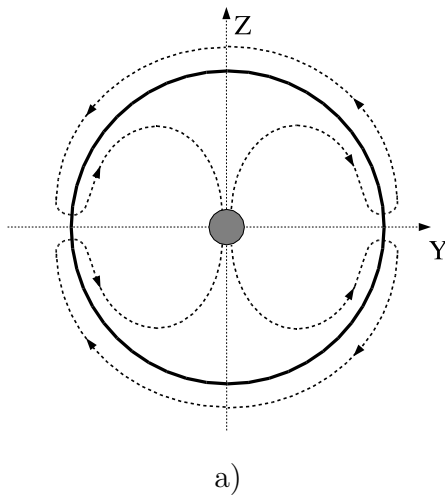


Figure 6.3: a) A sketch of the current loop in the terminator plane. b) z-component of the current in the terminator plane on a logarithmic scale for $\Sigma_P = 10$ mhos.

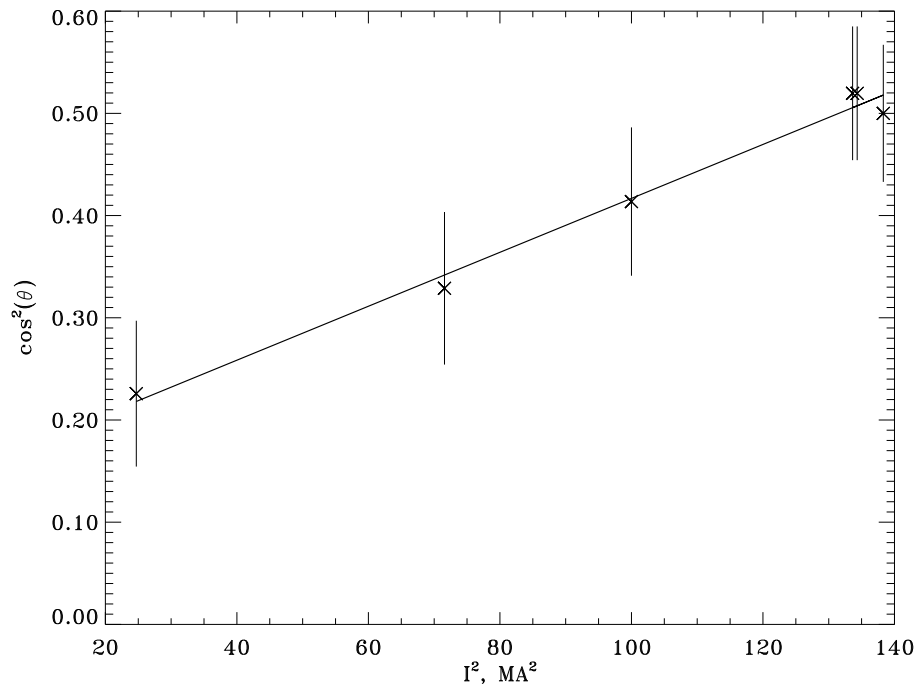
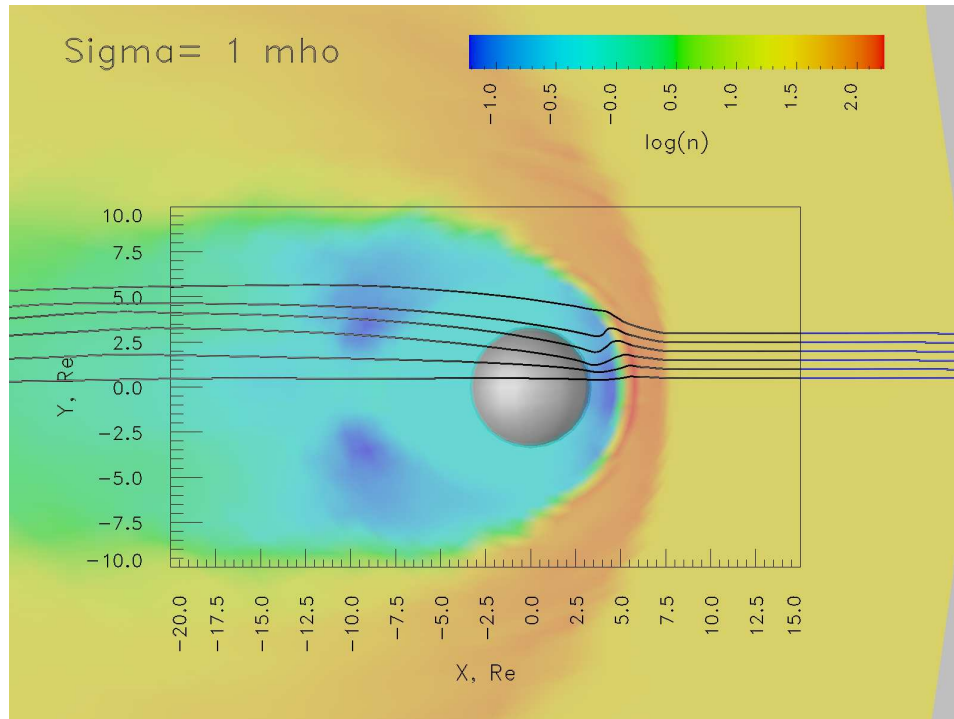
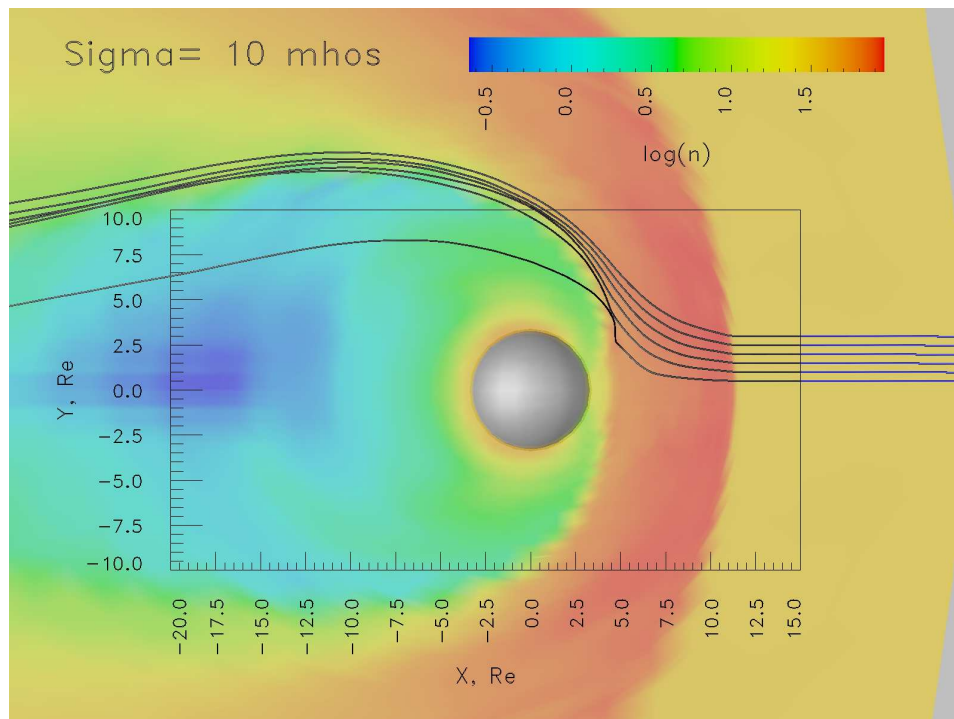


Figure 6.4: The dependence of the cosine squared of the flaring angle on the squared magnitude of the ionospheric integrated field aligned current. The error bars show the error estimations assuming the accuracy of a distance measurement equal to $\sim 0.3 R_E$ based on the local code resolution.



a)



b)

Figure 6.5: The magnetosphere in the $z=1$ plane. The background is the plasma mass density on a logarithmic scale. The lines are the projections of 3D flow streamlines. a) $\Sigma_P = 1$ mho, b) $\Sigma_P = 10$ mhos.

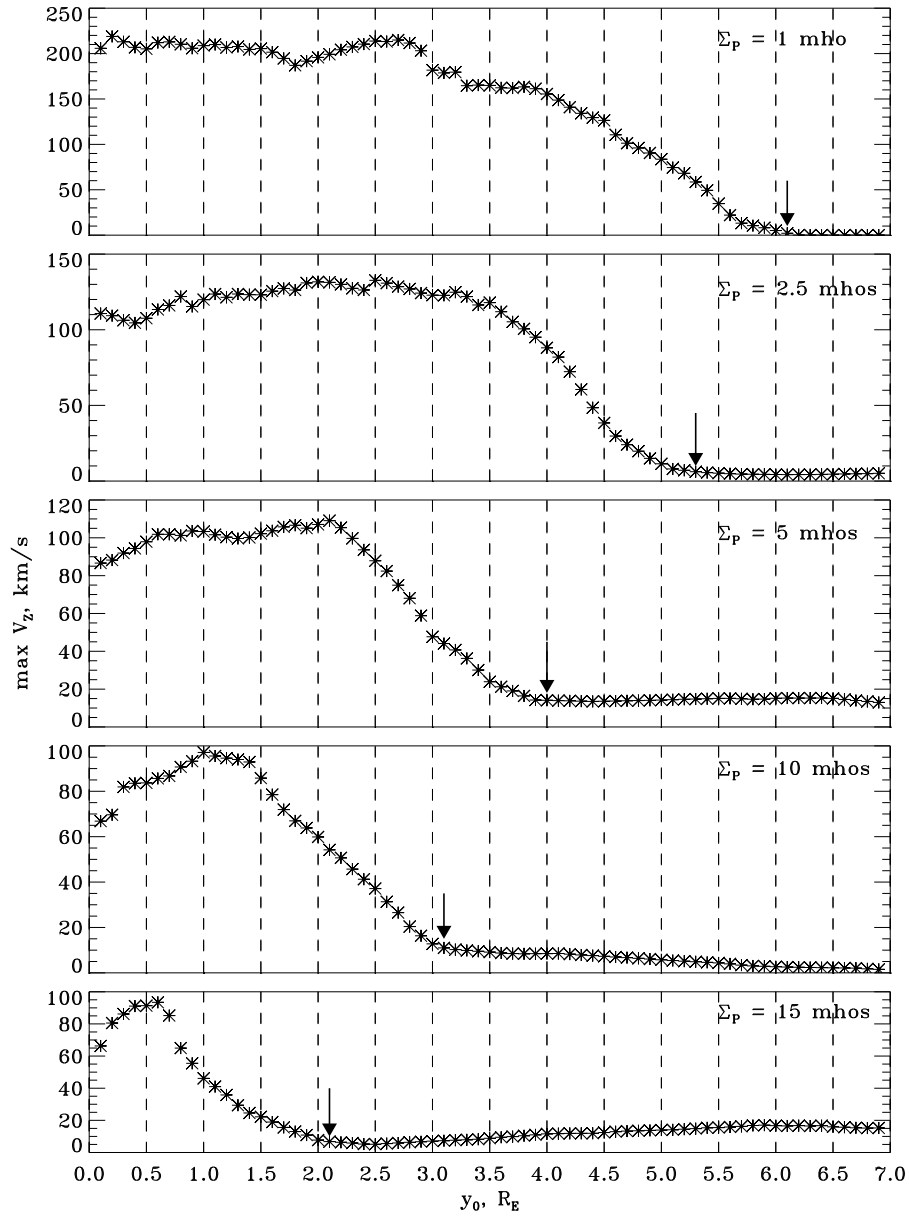


Figure 6.6: The maximum v_z component of the plasma velocity measured along a streamline originated in the solar wind upstream of the bow shock in the $z = 1$ plane at a distance y_0 from the symmetry axis.

Chapter 7 Summary and Future Work

Saturation of the cross polar cap potential remains one of yet to be fully understood phenomena in the magnetospheric physics. A number of recent observational techniques have confirmed that the transpolar potential does not grow linearly with the solar wind electric field, but rather saturates at a relatively low level limiting the amount of energy dissipated in the ionosphere. The Hill/Siscoe model, while being the only theoretical model of Φ_{PC} saturation, does not always agree with data and implies no direct mapping of the electrostatic potential from the dayside reconnection line to the ionosphere. In this dissertation we presented the results of global MHD modeling of the earth's magnetosphere intended to identify the physical processes behind the effect of the cross polar cap potential saturation.

7.1 Summary and Conclusions

The primary question raised in attempting to explain the phenomenon of the transpolar potential saturation is whether the effect can be described in terms of ideal MHD physics or it requires taking non-ideal effects into account. The Hill/Siscoe model includes non-MHD physics by construction: It leads to field-aligned potential drops between the dayside magnetopause and the

ionospheric polar cap. A number of problems arise when such an approach is used. First, parallel potential drops of the magnitudes predicted by the Hill/Siscoe model have never been observed. Furthermore, the model fails to match certain observations (e.g. ram pressure dependence issue discussed in [Shepherd *et al.*, 2003]), while agrees with others.

In this dissertation we took a different approach to the problem. The fact that global MHD models yield saturation of the cross polar cap potential means that the effect can, at least partly, be described within the ideal MHD domain. Ideal MHD description imposes strict limitations on the ways of the system evolution. The necessity for the reconnection potential to match the transpolar potential leads to a self-consistent development of all the components of the SW-M-I system. A change in the transpolar potential is accompanied by the reconfiguration of the entire system needed to accommodate new conditions, so that the dayside reconnection potential takes a value consistent with the value of the transpolar potential.

Based on these ideas and on the results of the simulations conducted we can now formulate a phenomenological model of saturation of the transpolar potential. A block diagram of this model is shown in Fig. 7.1. The model is formulated in the following manner. The solar wind activity influences the cross polar cap potential via two channels: (i) The solar wind convective electric field affects directly the reconnection potential which is mapped to the ionosphere and an increase in the IEF tends to amplify the transpolar potential; (ii) On the

other hand, as discussed in Chapter 3, the solar wind activity affects the ionospheric conductance either directly through energetic particle precipitation or indirectly through development of the two-stream plasma instability which heats electrons along the field lines. An increase in the ionospheric conductance provides a negative feedback on the reconnection potential through the entire chain of events discussed in the previous chapters. Components of this chain are summarized in the dashed box on the left of Fig. 7.1. First, the increase of the ionospheric conductance leads to the growth of the ionospheric field aligned currents which modify the pressure balance conditions at the flanks of the magnetopause. The additional magnetic pressure driven by these currents pushes the pressure-balanced surface of the magnetopause outward creating new boundary conditions for the magnetosheath flow (see sections 5.4, 6.2, 6.3, 6.4). Further, once the size of the magnetopause has been increased, the magnetosheath flow reconfigures, the stagnation is enhanced, and the reconnection potential is reduced (see sections 5.3, 5.4, 6.5). Finally, mapping of the electrostatic potential leads to a consecutive reduction of the cross polar cap potential (see section 5.2). The direct effect of the solar wind electric field on the reconnection potential is therefore balanced by the adverse effect of the ionospheric conductance, which leads to saturation.

7.2 Implications for Future Work

In this dissertation we have described in detail the feedback of the ionospheric conductance on the reconnection and transpolar potentials. However, the influence of the solar wind activity on the ionospheric conductance necessary for the model outlined above remains to be explored. The ionization and deposition of energy due to particle precipitation is included in most of global MHD models (see subsection 2.3.2), but it does not describe the dependence of the ionospheric conductance on the solar wind electric field crucial in relevance to the transpolar potential saturation. Besides that, the tendency of most global MHD models to overestimate the transpolar potential for real case simulations suggests that empirical models of ionospheric conductance lack important physics leading to the conductance enhancement. The anomalous electron heating in the ionosphere (see section 3.3) fills this gap in our understanding and provides a dependence of the ionospheric conductance on the solar wind electric field. Thus, a necessity to include the mechanism of anomalous heating in the models of the ionospheric conductance is obvious.

The first step toward incorporation of the anomalous electron heating into the ionospheric model is to make the ionospheric conductance a simple function of the local electric field. This approach mimics a parametrized dependence of the conductance on the solar wind electric field. We have accomplished a test simulation with the ionospheric Pedersen conductance $\Sigma_P = \Sigma_P^0 \sqrt{E/E_{thr}}$ and

$E_y = 16 \text{ mV/m}$, where $\Sigma_P^0 = 10$ mhos is the background Pedersen conductance, E_y is the solar wind electric field, E is the magnitude of the local ionospheric electric field, and $E_{thr} = 20$ mV/m is the Farley-Buneman threshold. The results of this simulation are shown in Figs. 7.2, 7.3. Fig. 7.2 shows the time evolution of the transpolar potential for the two cases: with the anomalous heating switched off (the upper curve) and switched on (the lower curve), respectively. As seen from the figure, the enhancement of the ionospheric conductance due to the turbulent electron heating leads to the drop in the cross polar cap potential of ~ 130 kV making the simulated potential close to the realistic value corresponding to a strong storm ($E_y = 16$ mV/m and $\Sigma_P = 10$ mhos).

Figs. 7.3a,b show moderation in the ionospheric electric field and potential distributions due to the anomalous electron heating as expected. These results show that incorporation of the turbulent electron heating in the ionospheric module of global MHD codes is crucial for them to produce results matching observations.

The success of the first test suggests the direction for future investigations. A more profound parametrization of Σ_P on local ionospheric electric field should be accomplished based on the non-linear theory of the instability saturation including MLT, altitudinal, and latitudinal dependence of plasma parameters (recombination coefficients, collision rates, etc.) [*Milikh and Dimant, 2003*]. With more realistic parametrization, extensive tests on real case simulations should be undertaken to validate the results against observations.

Model of Cross Polar Cap Potential Saturation

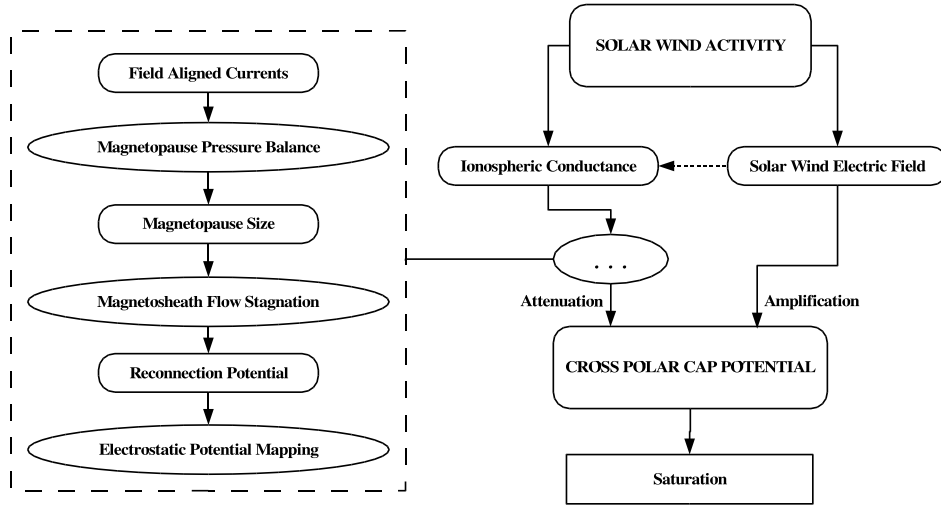


Figure 7.1: A block diagram of the phenomenological model of Φ_{PC} saturation.

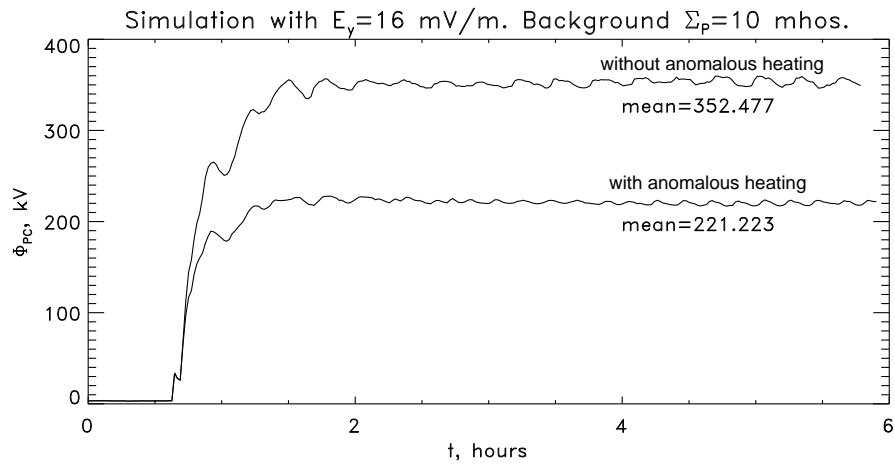


Figure 7.2: Time evolution of the transpolar potential simulated without (the upper curve) and with (the lower curve) turbulent electron heating in the ionosphere.

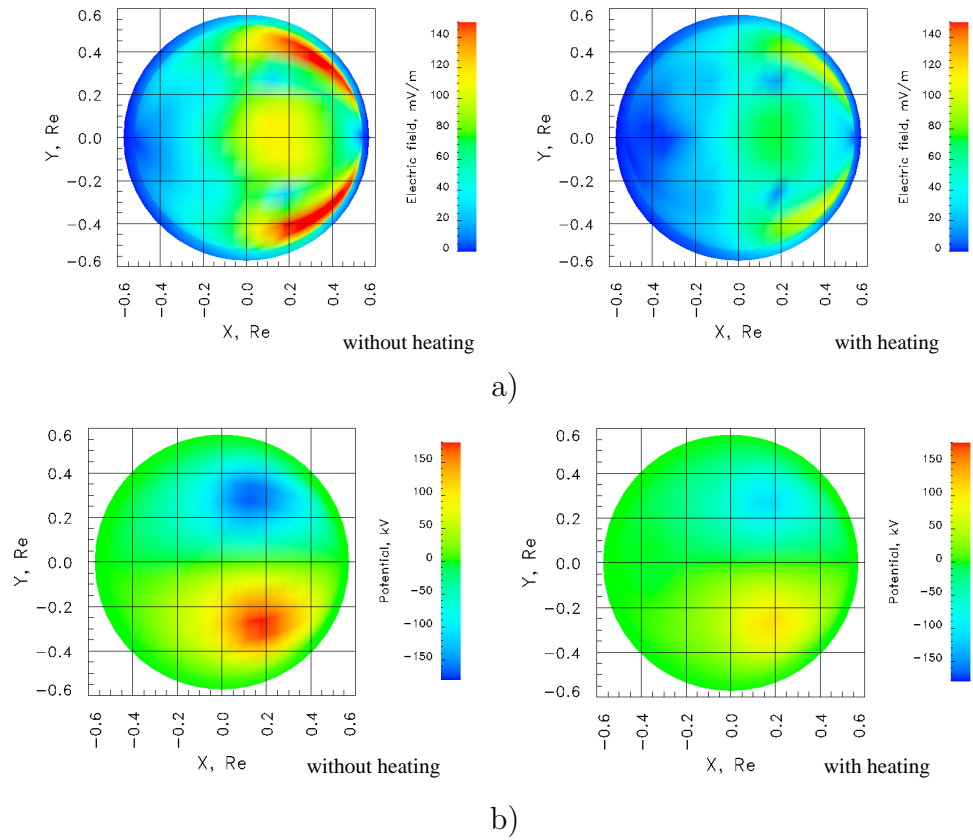


Figure 7.3: Distributions of the electric field (a) and electrostatic potential (b) in the polar ionosphere for the simulations with anomalous heating switched off (on the left) and switched on (on the right). Parameters of simulations are: solar wind electric field $E_y = 16$ mV/m and background ionospheric Pedersen conductance $\Sigma_P^0 = 10$ mhos.

BIBLIOGRAPHY

- Barr, R., and P. Stubbe, ELF and VLF radiation from the 'Polar Electrojet Antenna' (U), *Radio Sci.*, *19*, 1111, 1984.
- Baumjohann, W., and R. A. Treumann, *Basic Space Plasma Physics*, 87 pp., Imperial College Press, London, 1996.
- Boris, J., and D. Book, Flux-corrected transport I: SHASTA, a fluid transport algorithm that works, *J. Comp. Phys.*, *11*, 38–69, 1973.
- Boyle, C. B., P. H. Reiff, and M. R. Hairston, Empirical polar cap potentials, *J. Geophys. Res.*, *102*, 111–125, 1997.
- Brackbill, J. U., and D. C. Barnes, The effect of non-zero $\nabla \cdot \vec{B}$ on the numerical solution of the magnetohydrodynamic equations, *J. Comput. Phys.*, *35*, 426–430, 1980.
- Burke, W. J., D. R. Weimer, and N. C. Maynard, Geoeffective interplanetary scale sizes derived from regression analysis of polar cap potential, *J. Geophys. Res.*, *104*, 9989, 1999.
- Chiu, Y. T., and J. M. Cornwall, Electrostatic model of a quiet auroral arc, *J. Geophys. Res.*, *85*, 543, 1980.

- Chiu, Y. T., A. L. Newman, and J. M. Cornwall, On the structures and mapping of auroral electrostatic potentials, *J. Geophys. Res.*, *86*, 10,029, 1981.
- Dimant, Y. S., and G. M. Milikh, Model of anomalous electron heating in the E region: 1. Basic theory, *J. Geophys. Res.*, *108*, doi:10.1029/2002JA009524, 2003.
- Doyle, M. A., and W. J. Burke, S3-2 measurements of the polar cap potential, *J. Geophys. Res.*, *88*, 9125, 1983.
- Drake, J. F., Magnetic reconnection: A kinetic treatment, in *Physics of the Magnetopause, Geophysical Monograph*, vol. 90, edited by P. Song, B. U. Ö. Sonnerup, and M. F. Thomsen, pp. 155–165, American Geophysical Union, Washington DC, 1995.
- Dungey, J. W., Interplanetary magnetic field and the auroral zones, *Phys. Rev. Lett.*, *6*, 47, 1961.
- Durran, D. R., *Numerical Methods for Wave Equations in Geophysical Fluid Dynamics*, 241 pp., Springer, New York, 1999.
- Evans, C. R., and J. F. Hawley, Simulation of magnetohydrodynamic flows: A constrained transport method, *Astrophys. J.*, *332*, 659–677, 1988.
- Farris, M. H., and C. T. Russell, Determining the standoff distance of the bow shock: Mach number dependence and use of models, *J. Geophys. Res.*, *99*, 17,681–17,689, 1998.

- Fedder, J. A., and J. G. Lyon, The solar wind-magnetosphere-ionosphere current-voltage relationship, *Geophys. Res. Lett.*, *14*, 880–883, 1987.
- Fedder, J. A., and J. G. Lyon, The Earth’s magnetosphere is 165 R_E long: Self consistent currents, convection, magnetospheric structure, and processes for northward interplanetary magnetic field, *J. Geophys. Res.*, *100*, 3623, 1995.
- Fedder, J. A., J. G. Lyon, S. P. Slinker, and C. M. Mobarry, Topological structure of the magnetotail as function of interplanetary magnetic field direction, *J. Geophys. Res.*, *100*, 3613, 1995a.
- Fedder, J. A., S. P. Slinker, J. G. Lyon, and R. D. Elphinstone, Global numerical simulation of the growth phase and the expansion onset for substorm observed by Viking, *J. Geophys. Res.*, *100*, 19,083, 1995b.
- Freidberg, J. P., *Ideal Magnetohydrodynamics*, 7 pp., Plenum Press, New York and London, 1987.
- Gershenfeld, N., *The nature of mathematical modeling*, 186 pp., Cambridge University Press, Cambridge, 1999.
- Ghil, M., and P. Malanotte-Rizzoli, Data assimilation in meteorology and oceanography, *Adv. Geophys.*, *33*, 141, 1991.
- Goodrich, C. C., J. G. Lyon, M. J. Wiltberger, J. A. Fedder, and S. P. Slinker, Understanding magnetic storms and substorms through data closure with

- global MHD simulations, in *Proceedings of the Sixth International School/Symposium for Space Plasma Simulations*, edited by J. Büchner, C. T. Dum, and M. Scholer, Garching, Germany, 2001.
- Hairston, M. R., T. W. Hill, and R. A. Heelis, Observed saturation of the ionospheric polar cap potential during the 31 March 2001 storm, *Geophys. Res. Lett.*, *30*, 1325, 2003.
- Heppner, J. P., Polar-cap electric field distributions related to the interplanetary magnetic field direction, *J. Geophys. Res.*, *77*, 4877, 1972.
- Hill, T. W., Magnetic coupling between solar wind and magnetosphere: Regulated by ionospheric conductance?, *EOS, Trans. Am. Geophys. Un.*, *65*, 1047–1048, 1984.
- Hill, T. W., A. J. Dessler, and R. A. Wolf, The role of ionospheric conductivity in the acceleration of magnetospheric particles, *Geophys. Res. Lett.*, *3*, 429–432, 1976.
- Kan, J. R., and L. C. Lee, Energy coupling function and solar wind-magnetosphere dynamo, *Geophys. Res. Lett.*, *6*, 577, 1979.
- Kelley, M. C., *The Earth's ionosphere. Plasma physics and electrodynamics*, Academic Press, Inc., San Diego, CA, 1989.
- Landau, L. D., and E. M. Lifshitz, *Fluid Mechanics*, Pergamon Press, New York, 1959.

- Landau, L. D., and E. M. Lifshitz, *Electrodynamics of Continuous Media*, 2 ed., Pergamon Press, Oxford, 1985.
- Lax, P. D., Weak solutions of non-linear hyperbolic equations and their numeric computation, *Comm. Pure and Applied Mathematics*, 7, 159–193, 1954.
- Maltsev, Y. P., and W. B. Lyatsky, Field-aligned currents and erosion of the dayside magnetopause, *Planet. Space Sci.*, 23, 1257–1260, 1975.
- Milikh, G. M., and Y. S. Dimant, Model of anomalous electron heating in the E region: 2. Detailed numerical modeling, *J. Geophys. Res.*, 108, doi:10.1029/2002JA009527, 2003.
- Mobarry, C., J. A. Fedder, and J. G. Lyon, Equatorial plasma convection from global simulations of the Earth’s magnetosphere, *J. Geophys. Res.*, 101, 7859, 1996.
- Orens, J. H., and J. A. Fedder, The effects of geomagnetic field aligned potential difference on precipitating magnetospheric particles, *NRL Memo. Rep.*, p. 3573, 1978.
- Ossakow, S. L., K. Papadopoulos, J. Orens, and T. Coffey, Parallel propagation effects on the type 1 electrojet instability, *J. Geophys. Res.*, 80, 141–148, 1975.
- Papitashvili, V. O., and F. H. Rich, High-latitude ionospheric convection models derived from Defense Meteorological Satellite Program ion drift observations

- and parameterized by the interplanetary magnetic field strength and direction, *J. Geophys. Res.*, *107*, doi:10.1029/2001JA000264, 2002.
- Papitashvili, V. O., B. A. Belov, D. S. Faermark, Y. I. Feldstein, S. A. Golyshev, L. I. Gromova, and A. E. Levitin, Electric potential patterns in the northern and southern polar regions parameterized by the interplanetary magnetic field, *J. Geophys. Res.*, *99*, 13,251–13,262, 1994.
- Papitashvili, V. O., F. H. Rich, M. A. Heinemann, and M. R. Hairston, Parameterization of the Defense Meteorological Satellite Program ionospheric electrostatic potentials by the interplanetary magnetic field strength and direction, *J. Geophys. Res.*, *104*, 177–184, 1999.
- Petrinec, S. M., and C. T. Russell, Investigations of hydrodynamic and magnetohydrodynamic equations across the bow shock and along the outer edge of planetary obstacles, *Adv. Space Res.*, *20*, 743–746, 1997.
- Rees, M. H., *Physics and chemistry of the upper atmosphere*, Cambridge University Press, Cambridge, 1989.
- Reiff, P. H., and J. G. Luhmann, Solar wind control of the polar-cap potential, in *Solar Wind-Magnetosphere Coupling*, edited by Y. Kamide and J. A. Slavin, p. 453, Terra Sci., Tokyo, 1986.
- Reiff, P. H., R. W. Spiro, and T. W. Hill, Dependence of polar cap potential drop on interplanetary parameters, *J. Geophys. Res.*, *86*, 7639, 1981.

- Rich, F. J., and M. Hairston, Large-scale convection patterns observed by DMSP, *J. Geophys. Res.*, *99*, 3827–3844, 1994.
- Richmond, A. D., and Y. Kamide, Mapping electrodynamic features of the high-latitude ionosphere from localized observations: Technique, *J. Geophys. Res.*, *93*, 5741, 1988.
- Robinson, R. M., R. R. Vondrak, K. Miller, T. Babbs, and D. A. Hardy, On calculating ionospheric conductivities from the flux and energy of precipitating electrons, *J. Geophys. Res.*, *92*, 2565, 1987.
- Ruohoniemi, J. M., and K. B. Baker, Large-scale imaging of high-latitude convection with Super Dual Auroral Radar Network HF radar observations, *J. Geophys. Res.*, *103*, 20,797, 1998.
- Ruohoniemi, J. M., and R. A. Greenwald, Statistical patterns of high-latitude convection obtained from Goose Bay HF radar observations, *J. Geophys. Res.*, *101*, 21,743, 1996.
- Russell, C. T., G. Lu, and L. G. Luhmann, Lessons from the ring current injection during the September 24, 25, 1998 storm, *Geophys. Res. Lett.*, *27*, 1371–1374, 2000.
- Russell, C. T., J. G. Luhmann, and G. Lu, Nonlinear response of the polar ionosphere to large values of the interplanetary electric field, *J. Geophys. Res.*, *106*, 18,495–18,504, 2001.

- Schlegel, K., and J. P. St.-Maurice, Anomalous heating of the polar E region by unstable plasma waves: 1. observations, *J. Geophys. Res.*, *86*, 1447–1452, 1981.
- Schunk, R. W., and A. F. Nagy, *Ionospheres Physics, plasma physics, and chemistry*, Cambridge University Press, Cambridge, 2000.
- Shepherd, S. G., R. A. Greenwald, and J. M. Ruohoniemi, Cross polar cap potentials with Super Dual Auroral Radar Network during quasi-steady solar wind and interplanetary magnetic field conditions, *J. Geophys. Res.*, *107*, doi:10.1029/2001JA000152, 2002.
- Shepherd, S. G., J. M. Ruohoniemi, and R. A. Greenwald, Testing the Hill model of transpolar potential with Super Dual Auroral Radar Network observations, *Geophys. Res. Lett.*, *30*, 1002, doi:10.1029/2001JA000152, 2003.
- Sibeck, D. G., R. E. Lopez, and E. C. Roelof, Solar wind control of the magnetopause shape, location, and motion, *J. Geophys. Res.*, *96*, 5489–5495, 1991.
- Siscoe, G. L., N. U. Crooker, and K. D. Siebert, Transpolar potential saturation: Roles of region 1 current system and solar wind ram pressure, *J. Geophys. Res.*, *107*, 1321, 2002a.
- Siscoe, G. L., G. M. Erickson, B. U. Ö. Sonnerup, N. C. Maynard, J. A. Schoendorf, K. D. Siebert, D. R. Weimer, W. W. White, and G. R. Wilson,

- Hill model of transpolar potential saturation: Comparisons with MHD simulations, *J. Geophys. Res.*, *107*, doi:10.1029/2001JA000109, 2002b.
- Slinker, S. P., J. A. Fedder, and J. G. Lyon, Plasmoid formation and evolution in a numerical simulation of a substorm, *Geophys. Res. Lett.*, *22*, 859–862, 1995.
- Spreiter, J. R., A. L. Summers, and A. Y. Alksne, Hydrodynamic flow around the magnetosphere, *Planet. Space Sci.*, *14*, 223–253, 1966.
- St.-Maurice, J. P., A unified theory of anomalous resistivity and Joule heating effects in the presense of ionospheric E region irregularities, *J. Geophys. Res.*, *92*, 4533–4542, 1987.
- St.-Maurice, J. P., and R. Laher, Are observed broadband plasma wave amplitudes large enough to explain the enhanced temperatures in the high-latitude E region?, *J. Geophys. Res.*, *90*, 2843–2850, 1985.
- Stauning, P., and J. K. Olesen, Observations of the unstable plasma in the disturbed E region, *Phys. Scripta*, *40*, 325–332, 1989.
- Stone, J. M., and M. L. Norman, ZEUS-2D: A radiation magnetohydrodynamics code for astrophysical flows in two space dimensions. II. the magnetohydrodynamic algorithms and tests, *Astrophys. J. Supp.*, *80*, 791–818, 1992.
- Vasyliunas, V. M., Theoretical models of magnetic field line merging, 1, *Rev. Geophys. Space Phys*, *13*, 303, 1975.

- Vasyliunas, V. M., J. R. Kan, G. L. Siscoe, and S. I. Akasofu, Scaling relations governing magnetospheric energy transfer, *Planet. Space Sci.*, *30*, 359–365, 1982.
- Weimer, D. R., Models of high-latitude electric potentials derived with a least error fit of spherical harmonic functions, *J. Geophys. Res.*, *100*, 19,595, 1995.
- Weimer, D. R., A flexible, IMF dependent model of high-latitude electric potentials having "space weather" applications, *Geophys. Res. Lett.*, *23*, 2549, 1996.
- Weimer, D. R., An improved model of ionospheric electric potentials including perturbations and application to the Geospace Environment Modeling November 24, 1996, event, *J. Geophys. Res.*, *106*, 407, 2001.
- Yee, K. W., Numerical solution of initial boundary value problems involving Maxwell's equations in isotropic media, *IEEE Trans. Antenn. Propag.*, *14*, 302–307, 1966.
- Zalesak, S. T., Fully multidimensional flux-corrected transport algorithms for fluids, *J. Comput. Phys.*, *31*, 335, 1979.

